Doctorate Dissertation

博士論文

Soft-x-ray Magnetic Dichroism Studies of Magnetic and Orbital Anisotropies in $La_{1-x}Sr_xMnO_3$ Thin Films

（軟Ｘ線磁気二色性による $La_{1-x}Sr_xMnO_3$ 薄膜の磁気異方性および軌道異方性に関する研究）

Goro Shibata

芝田　悟朗

Abstract

Magnetic thin films and multilayers exhibit various intriguing physical properties which are different from those of the bulk due to the effects of epitaxial strain, surface and interfacial effects, lowered dimensionality, and inter-layer coupling. They often exhibit magnetic anisotropy due to the combined effects of anisotropic electronic structure and spin-orbit interaction (SOI). Understanding the microscopic origin of the magnetic anisotropy in ferromagnetic thin films and controlling it have been one of the major research topics both from scientific and technological points of view. Since their magnetic properties are governed by mutual coupling of spin, charge, orbital, and lattice degrees of freedoms, it is highly desired to clarify the detailed electronic structures in order to elucidate the microscopic origin of their magnetic properties, especially the magnetic anisotropy. Soft x-ray spectroscopy, including x-ray absorption spectroscopy (XAS), x-ray magnetic circular dichroism (XMCD), and x-ray magnetic linear dichroism (XMLD), has been a powerful probe for the electronic states and magnetism of $3d$ transition-metal compounds. Since electronic structures and magnetism can be highly anisotropic in thin films and multilayers, soft x-ray spectroscopy with varying incident angles and magnetic-field angles will give new insights into the physical properties of thin films.

In the present thesis, using the 'vector-magnet' apparatus for soft x-ray spectroscopy which has been newly developed by our group, I have worked on the angle-dependent XAS, XMCD, and XMLD measurements and the development of the analysis methods for them, and have studied the electronic structures and their anisotropies of $La_{1-x}Sr_xMnO_3$ (LSMO) thin films. LSMO is a material which shows ferromagnetic metallicity in the widest ranges of hole concentration x and has highest Curie temperature above the room temperature among colossal-magnetoresistive perovskite manganites. From the angle-dependent XMCD experiments, it has been demonstrated that the anisotropy of the spin-density distribution of Mn $3d$ electrons changes depending on the epitaxial strain and that it is correlated with the change of strain-induced magnetic anisotropy. From the XMLD experiments, changes in the charge-density anisotropy of Mn $3d$ electrons induced by the spin polarization has been observed, which can be understood as the inverse process of the strain-induced magnetic anisotropy.

The present studies will not only deepen our understanding of the relationship between the electronic structure and the magnetic properties of manganite thin films, but also pave the way for elucidating the origin of magnetic anisotropy in transition-metal thin films in terms of microscopic electronic structure.

Contents

Chapter 1

Introduction

With the progress in sample growth technique in recent years, it has become possible to fabricate magnetic thin films and multilayers of metals and transition-metal oxides, with controlling their structures in the atomic scale. They generally exhibit a wide variety of intriguing magnetic and electric properties which are different from those of the bulk, due to the effects of epitaxial strain, surface and interfacial effects, lowered dimensionality, and inter-layer coupling [1]. Some of these thin films and multilayers exhibit perpendicular magnetic anisotropy (PMA), namely, the easy magnetization axis is along the perpendicular direction to the sample despite the demagnetizing field within the film. Magnetic thin films with PMA have potential application for, e.g., high-density magnetic recording media and spintronics devices [1]. Clarifying the physical origin of magnetic anisotropy in ferromagnetic thin films and controlling it have been major research topics not only from technological points of view but also from scientific point of view.

In general, magnetism and magnetic anisotropy of ferromagnetic thin films are governed by their electronic states of transition-metal d electrons through spin-orbit interaction (SOI). X-ray magnetic circular dichroism (XMCD) using synchrotron x rays has been a useful spectroscopic method for revealing the electronic state of these systems. It has advantages that one can obtain information about spin and orbital magnetic moments and microscopic electronic structure such as chemical valence and strength of crystal fields in an element-selective way, and that high signal intensities can be obtained even if the volume fraction of the ferromagetic sample is low as in thin films and multilayers. Moreover, it has been theoretically proposed that, from the angular dependence of XMCD spectra, one can also extract a physical quantity called "magnetic dipole" $\boldsymbol{M}_{\mathrm{T}}$, which represents the anisotropic distribution of the spin-density, i.e., the preferential orbital occupation of spin-polarized electrons [2,3]. It has also been pointed out that, by

using linearly polarized x rays instead of circularly polarized ones, one can obtain information about the electronic and magnetic state of d electrons complementary to those from XMCD. This technique is called x-ray magnetic linear dichroism (XMLD), and gives information about the anisotropic charge distribution, i.e., the deformation of electron orbitals induced by spin polarization. The angle-dependent XMCD and XMLD spectroscopy can be utilized to reveal the anisotropic electronic state of ferromagnetic materials and, therefore, can provide great clues on the microscopic mechanism of the magnetic anisotropy of magnetic thin films and multilayers. However, there have been few experimental studies so far which utilize the angle-dependent XMCD and XMLD methods, due to the experimental limitation that the magnetic-field direction is fixed parallel to the incident x rays in conventional XMCD apparatus.

The purpose of the present studies in this thesis is to clarify the relationship between the macroscopic magnetic properties and the electronic structure of magnetic thin films, especially the orbital occupation and the spin states, by XMCD and XMLD spectroscopies. Using a newly-developed XMCD apparatus with a vector-type magnet [4], it has become possible to measure the field-angle dependence of the XMCD spectra, which can be utilized for studying the magnetic anisotropy of ferromagnetic thin films. The main focus in the present studies is put on thin films of the ferromagnetic transition-metal oxide $La_{1-x}Sr_xMnO_3$ (LSMO), which is well known for its novel magnetic properties such as colossal magnetoresistance (CMR) and half metallicity. The present studies show that the magnetic anisotropy of the LSMO thin films induced by epitaxial strain from the substrate is associated with the anisotropy of the spin-density distribution, i.e., the magnetic dipole $\boldsymbol{M}_{\mathrm{T}}$. By comparison with previous x-ray linear dichroism studies, it has also been found that the preferential orbital occupation of spin-polarized and spin-unpolarized electrons are different. This may be one of the possible origins of magnetic dead layers formed at the surface and interfaces of LSMO thin films, which have been reported in previous studies [5–8].

The present thesis is organized as follows. The physical properties of LSMO and its thin films are introduced in Chap. 2. The basic principles of XMCD and XMLD are summarized in Chap. 3. The experimental details of are described in Chap. 4. In Chap. 5, study of the thickness-dependent magnetic transition in LSMO thin films by conventional XMCD is presented. A phase-mixed nature of the thickness-dependent phase transition has been revealed from the magnetic-field dependence of the XMCD intensities. Chap. 6 is devoted for the angle-dependent XMCD study on the LSMO thin films using the vector-XMCD apparatus. In this study, the magnetic dipole $\boldsymbol{M}_{\mathrm{T}}$ has been detected and its substrate dependence is discussed in conjunction

with the magnetic anisotropy of the films. Chap. 7 describes the XMLD study on the LSMO thin films using the same vector-XMCD apparatus. The results show that the charge distribution of the Mn 3d electrons are changed by spin polarization through SOI. Finally, summaries and future prospects are presented in Chap. 8.

Chapter 2

Physical properties of $La_{1-x}Sr_xMnO_3$ thin films

2.1 Perovskite-type transition-metal oxides

Perovskite-type $3d$ transition metal oxides (TMOs) ABO_3 have been extensively studied for decades due to their wide variety of novel physical phenomena such as metal-insulator transition (MIT), complex magnetic transitions, and charge/orbital ordering (CO/OO) [9]. The strong Coulomb correlation between the transition-metal (TM) $3d$ electrons and the complex mutual coupling of the charge, spin, orbital, and lattice degrees of freedom lead to these novel phenomena. Figure 2.1(a) describes the crystal structure of the perovskite-type oxides ABO_3. The TM atom (B) is surrounded by six oxygen atoms octahedrally and these BO_6 octahedra form a network by sharing their corners as shown in Fig. 2.1(b). The rare-earth atoms (A) are located at the interstitial sites of the octahedra and serve as electron donors into the TM $3d$-O $2p$ bands.

The physical properties of the perovskite-type TMOs can be controlled by changing either of the bandwidth (bandwidth control) or the electron concentration (filling control) of the TM $3d$-O $2p$ bands [9]. As shown in Fig. 2.2(a), TMOs tend to become Mott insulators when the ratio of the Coulomb interaction U to the bandwidth W (U/W) is large and the electron filling is close to an integer. The bandwidth can be controlled by doping atoms with different ionic radius into either of the A or B site to induce the distortion and/or rotation of the BO_6 octahedra [Fig. 2.1(b)]. The bonding length or the angle of the B-O-B chain changes due to this distortion or rotation of the octahedra, resulting in the changes in the bandwidth. The degree of the crystal distortion can be quantified using the tolerance factor f defined by

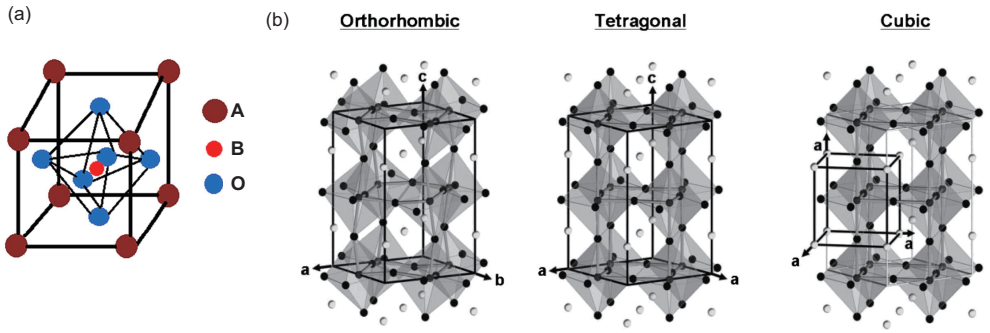

Figure 2.1: Crystal structures of perovskite-type transition-metal oxides (TMOs) ABO_3. (a) Unit cell of the cubic perovskite structure. (b) Orthorhombic (left) and tetragonal (middle) crystal structures with distortion and/or rotation of the BO_6 octahedra, and cubic (right) crystal structure without distortion or rotation of the octahedra. Panel (a) is adapted from Ref. [10] and (b) is adapted from Ref. [11].

the following equation:

$$f = (r_A + r_O)/\sqrt{2}(r_B + r_O), \tag{2.1}$$

where r_A, r_B, and r_O are the ionic radii of A, B, and O, respectively [9]. The crystal structure becomes cubic in the case of $f \sim 1$. When f deviates significantly from 1, rotation and/or distortion of the octahedra are induced and the crystal symmetry is lowered down to rhombohedral or orthorhombic. The electron concentration can be controlled by doping atoms with different valence, e.g., substituting Sr^{2+} for La^{3+} or Ca^{2+} for Y^{3+} in the A site. Figure 2.2(b) schematically describes MITs for various TMOs. Substituting different atoms into the A or B site leads to the changes in the bandwidth and/or the electron filling, resulting in MITs.

2.2 Perovskite-type manganites

2.2.1 Transport and magnetic properties

Among the perovskite-type TMOs, the manganese oxides (manganites) $AMnO_3$ have been of great interest due to their intriguing magnetic properties. Figure 2.3 shows the phase diagrams for various perovskite-type manganites $R^{3+}_{1-x}A^{2+}_xMnO_3$ (R = rare-earth atom, A = alkaline-earth atom). The parent compounds $RMnO_3$ are antiferromagnetic Mott insulators (AFM-I) with canted magnetic moment in the ground state. Upon substitution of the alkaline-earth atom A for the rare-earth atom R, holes are

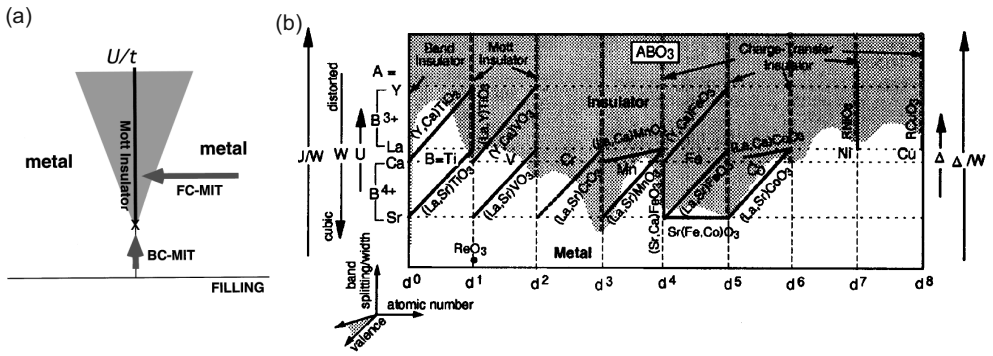

Figure 2.2: Metal-insulator transitions (MITs) in perovskite-type TMOs. (a) Schematic illustration of the bandwidth-controlled and filling-controlled MITs. (b) Metal-insulator phase diagram for various TMOs. Reproduced from Refs. [9] and [12].

doped and the systems tend to turn into ferromagnetic and metallic phases. The ferromagnetic phases are most stabilized around $x \sim 0.2$-0.4 and the systems again turn into antiferromagnetic insulating phases with further hole doping. Among the compounds in Fig. 2.3, $La_{1-x}Sr_xMnO_3$ (LSMO, tolerance factor $f = 0.930$ at $x = 0.3$ [13]) has the widest bandwidth W due to its small crystal distortion, $Pr_{1-x}Ca_xMnO_3$ (PCMO, $f = 0.906$ at $x = 0.3$ [13]) has the narrowest W due to large distortion, and $Nd_{1-x}Sr_xMnO_3$ (NSMO, $f = 0.917$ at $x = 0.3$ [13]) and $La_{1-x}Ca_xMnO_3$ (LCMO, $f = 0.916$ at $x = 0.3$ [13]) have intermediate values. In accordance with this, LSMO exhibits a ferromagnetic metallic (FM-M) phase in the widest range of x and has the Curie temperature (T_C) higher than room temperature, whereas the ranges of the FM-M phase is narrower in NSMO and LCMO, and the metallic phase is completely suppressed in PCMO. In the systems where the crystal distortion is large like PCMO, electron correlation plays important roles and charge-ordered (CO) states are often observed around certain doping levels, as shown in Fig. 2.3.

One of the most notable phenomena in perovskite-type manganites is colossal magnetoresistance (CMR) [14–16]. CMR is a extraordinarily large reduction of electric resistivity under external magnetic field. Figure 2.4 shows the examples of the CMR effect observed in LSMO ($x = 0.175$) [17] and LCMO ($x = 0.3$) [16]. CMR is often observed near the boundary between the FM-M and AFM-I phases in the phase diagram of Fig. 2.3. As shown later, the CMR effect originates from the phase transition in a microscopic scale from the AFM-I to the FM-M phases induced by magnetic field.

Among all the manganites, LSMO in the optimal doping range of the

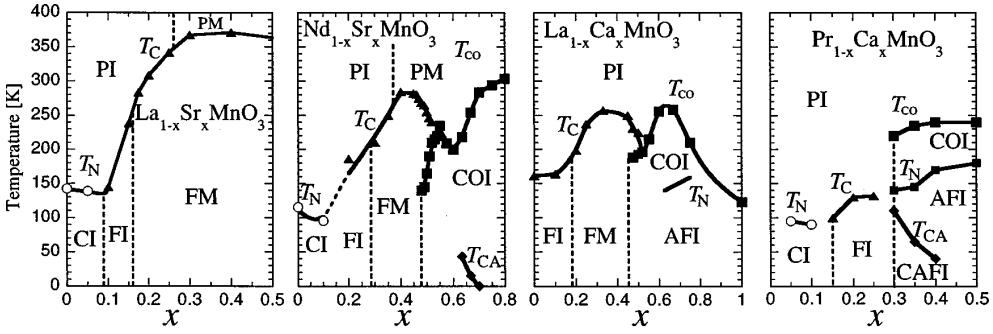

Figure 2.3: Phase diagrams for various manganese oxides $R_{1-x}A_x\mathrm{MnO}_3$. Each symbol in the figure denotes: P: paramagnetic, F: ferromagnetic, C: canted antiferromagnetic, AF: antiferromagnetic, CO: charge-ordered, I: insulator, and M: metal. 'CAFI' denotes the canted antiferromagnetic insulator *with* charge ordering. Reproduced from Ref. [9].

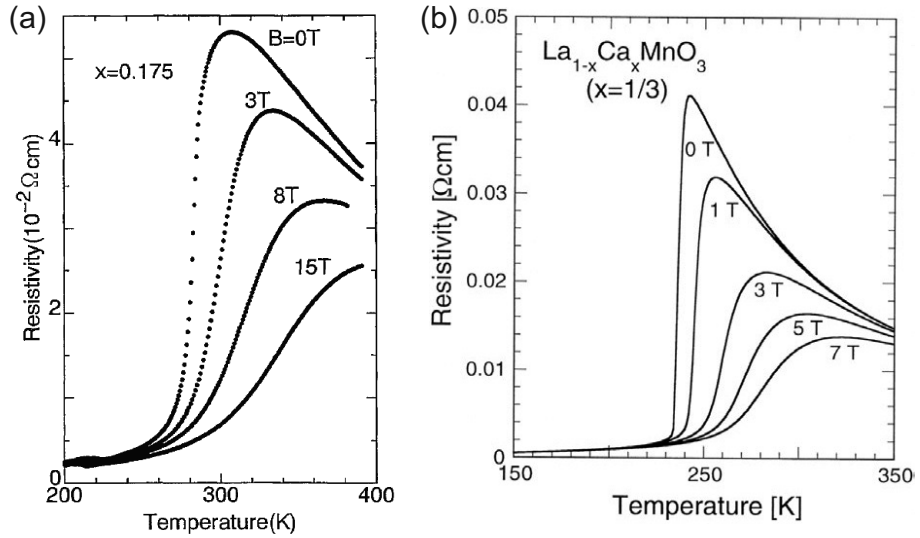

Figure 2.4: Colossal magnetoresistance (CMR) in (a) LSMO ($x = 0.175$) and (b) LCMO ($x = 1/3$). Panel (a) adapted from Ref. [17] and (b) from Ref. [16].

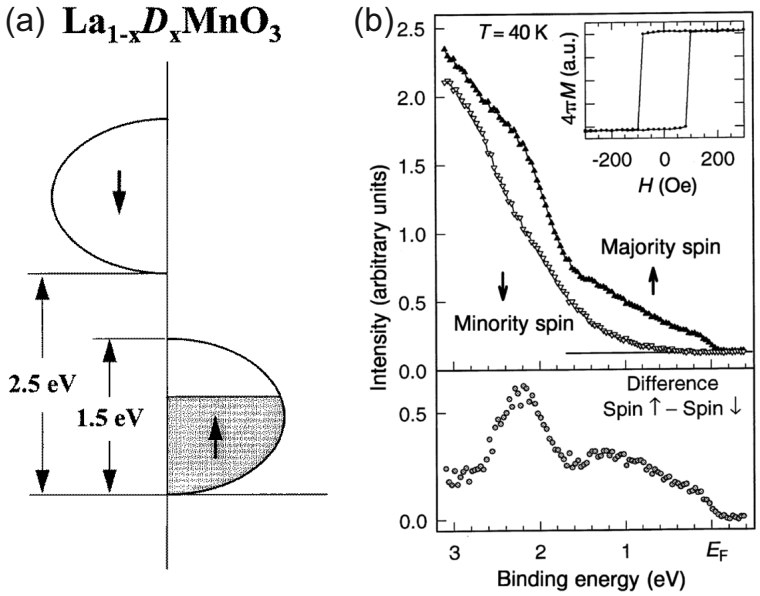

Figure 2.5: Half metallicity of LSMO. (a) Schematic band diagram for a half-metallic material. (b) Spin-resolved photoemission spectroscopy for half-metallic LSMO ($x = 0.3$). Panel (a) adapted from Ref. [14] and (b) from Ref. [18].

FM-M phase is known to show half metallicity. A half-metallic material is a ferromagnetic material which is conductive for electrons with one spin direction but is insulating for electrons with the other spin direction, as schematically shown in Fig. 2.5(a). The half-metallic nature of LSMO has been confirmed by spin-resolved photoemission spectroscopy (PES), as shown in Fig. 2.5(b) [18]. Since this half-metallic property can be utilized for spin-filters or magnetically-driven switching devices such as magnetic tunneling junctions (MTJs), LSMO has been regarded as a candidate material in the field of spin-electronics (spintronics).

2.2.2 Electronic structure and spin interactions

In order to explain the electric and magnetic properties of the perovskite-type manganites including the CMR effect, one has to consider their microscopic electronic structure. Figure 2.6(a) and 2.6(b) schematically illustrate the energy levels of Mn $3d$ electrons in perovskite-type manganites $R_{1-x}A_x\mathrm{MnO_3}$ with cubic and tetragonal crystal structures, respectively. In the case of the cubic structure [Fig. 2.6(a)], the five d orbitals are split into two sublevels, the e_g ($x^2 - y^2/3z^2 - r^2$) and the t_{2g} ($xy/yz/zx$) levels, due to the crystal field ($10Dq$) produced by the surrounding oxygen atoms. The

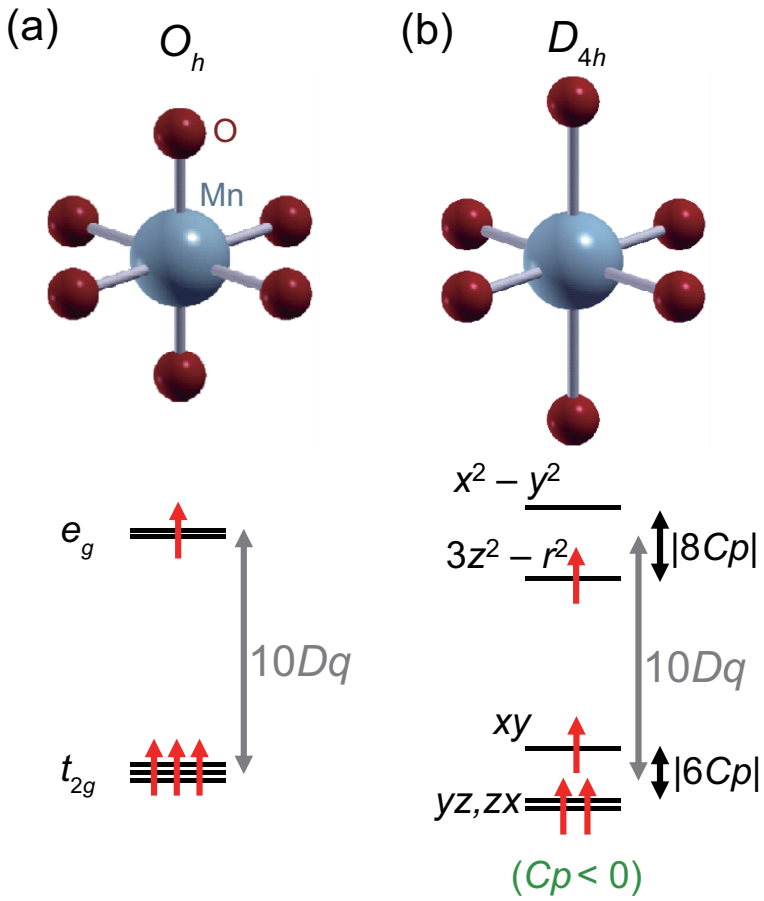

Figure 2.6: Energy levels of the Mn $3d$ electrons under the (a) octahedral (O_h) and (b) tetrahedral (D_{4h}) symmetry. Panel (b) adapted from Ref. [21]. The images of the clusters has been drawn by using XCrySDen [22].

Mn ions are in a mixed valence state of Mn^{3+} ($3d^4$) and Mn^{4+} ($3d^3$) (the average valence of Mn being $3 + x$), and thus the t_{2g} majority-spin band is fully occupied while the e_g majority-spin band is partially occupied. Therefore, the electronic states in the e_g band play an important role in order to understand the physical properties of manganites. In the case of the tetragonal structure, the e_g and t_{2g} sublevels are further split as shown in Fig. 2.6(b), since the x- or y-axis and the z-axis become inequivalent. Thus, in the case of Mn^{3+}, either of the $x^2 - y^2$ or $3z^2 - r^2$ orbital is preferentially occupied depending on the sign of the distortion (elongation or shrinkage of the MnO_6 octahedra), and a charge- and orbital-ordered insulating phase is often stabilized [19]. In some manganite systems with Mn^{3+} valence, such a crystal distortion *spontaneously* occurs in order to lower the total electron energy [20], which is known as Jahn-Teller effect.

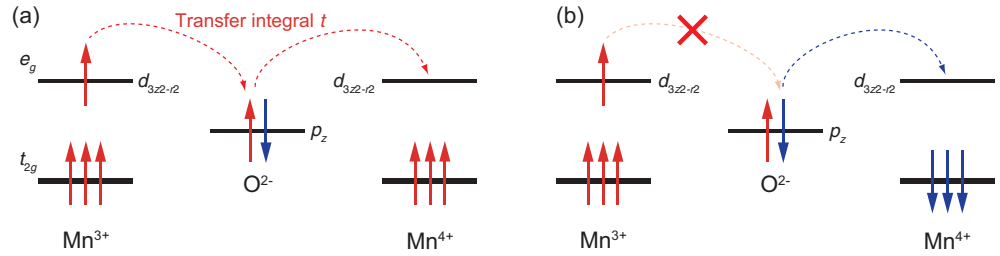

Figure 2.7: Description of the double-exchange (DE) interaction. (a) Electronic states of a Mn^{3+}-O-Mn^{4+} chain in a spin-parallel configuration. (b) Same as (a) but in a spin-antiparallel configuration. The DE interaction favors the spin-parallel configuration (a).

The ferromagnetism of hole-doped perovskite-type manganites can be explained in terms of double-exchange (DE) interaction, which is schematically shown in Fig. 2.7. DE interaction acts between Mn^{3+} and Mn^{4+} ions, and stabilizes ferromagnetic spin configuration. It originates from the fact that the probability of electron hopping depends on the relative directions of the spins of the two ions: The spin directions of the t_{2g} and e_g electrons in a Mn ion have to be the same due to strong Hund coupling J_{H} between them. When the neighboring Mn ions have the same spin directions [Fig. 2.7(a)], the $d_{3z^2-r^2}$ electrons of the Mn^{3+} ion can hop into the $d_{3z^2-r^2}$ orbital of the Mn^{4+} ions via the O $2p_z$ orbital, and thus there is an energy gain due to the transfer integral t between Mn and O. When the spins of the neighboring Mn atoms are antiparallel [Fig. 2.7(b)], however, hopping of the $d_{3z^2-r^2}$ electron from Mn^{3+} to Mn^{4+} is prohibited due to J_{H}, resulting in no energy gain by t. This is the reason for the ferromagnetic spin interaction between Mn^{3+} and Mn^{4+} ions.

In addition to the DE interaction, superexchange (SE) interaction also plays a role (Fig. 2.8). SE interaction acts between two neighboring Mn^{3+} ions and stabilizes antiferromagnetic spin coupling. It can be derived from the perturbation theory: When the neighboring Mn spins are antiparallel [Fig. 2.8(a)], there are more virtual excitation paths due to the electron transfer (t) than the case where the Mn spins are parallel [Fig. 2.8(b)], and thus the ground-state energy becomes lower in the former case, as can be understood from the formula of the perturbation theory. Therefore, it follows that the antiferromagnetic spin coupling is preferred between the two Mn^{3+} ions.

The competition between the DE and SE spin interactions, together with the preferential orbital occupation induced by the crystal distortion, governs the electric and magnetic properties of manganites.

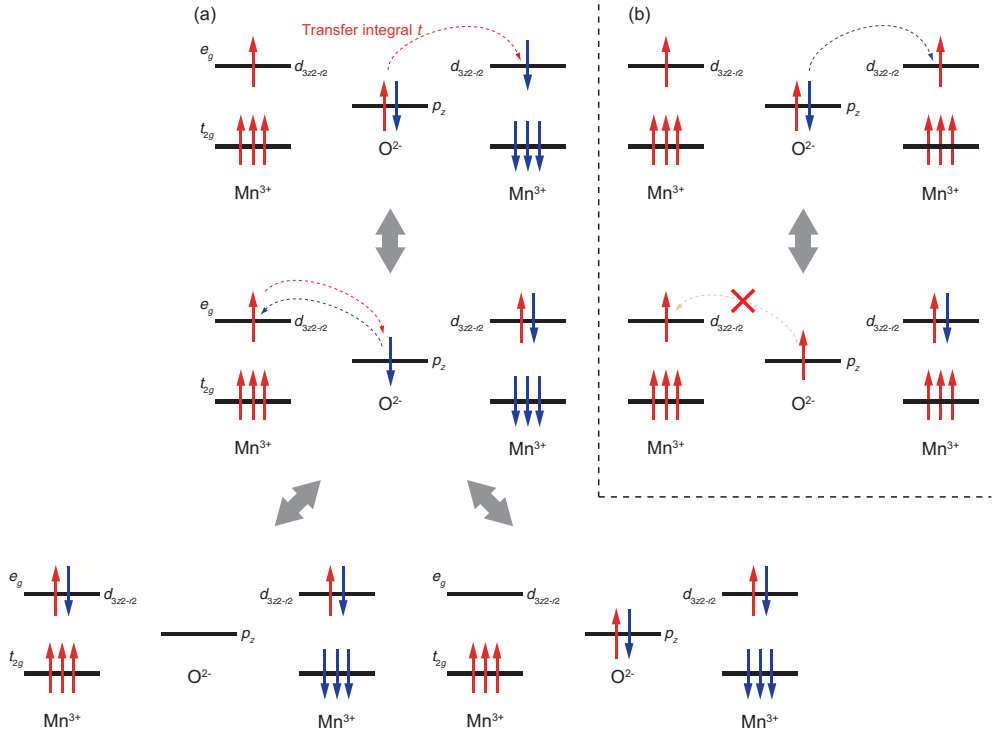

Figure 2.8: Description of the superexchange (SE) interaction. (a) Electronic states of a Mn^{3+}-O-Mn^{3+} chain in a spin-antiparallel configuration. (b) Same as (a) but in a spin-parallel configuration. The gray arrows represent the virtual excitations in the perturbation theory. The SE interaction favors the spin-antiparallel configuration (a).

2.2.3 Phase-separation model

The ferromagnetic insulating (FM-I) phase in the phase diagram of manganites (Fig. 2.3) cannot be explained by the simple DE model because both the metallicity and the ferromagnetism are associated with the electron hopping and they should appear at the same time within the model. In order to resolve this problem, a phase-separation model has been proposed [23, 24]. In this model, one assumes that the AFM-I and the FM-M phases are separated but are mixed together in a microscopic scale. If the volume fraction of the FM-M phase is finite but small, there is no electric conduction path which goes through the entire system and hence it becomes insulating in a macroscopic scale, although finite ferromagnetic moment remains. In this way, the FM-I phase near the boundary of the AFM-I and FM-M phases can be explained. This model also explains the CMR effect, because small increase in the volume fraction of the FM-M phase due to magnetic field can build the electric conduction path and thus can lead to a quick decrease in

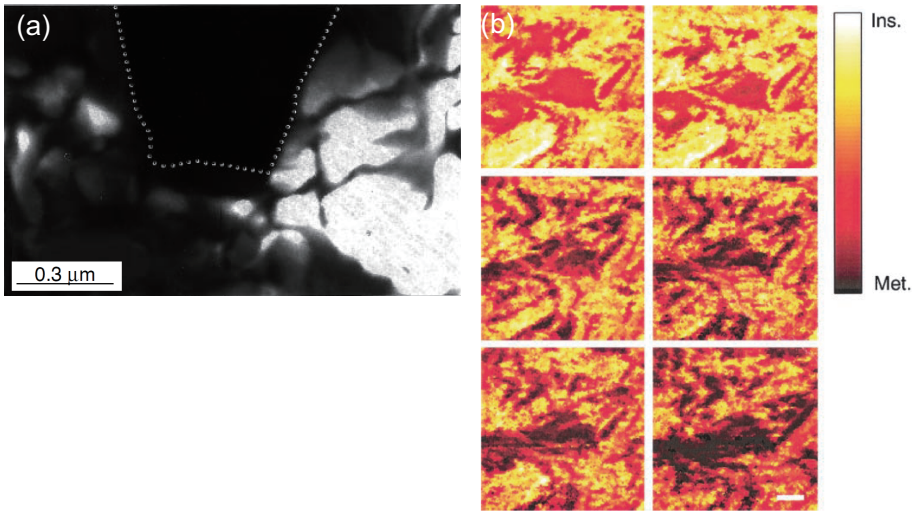

Figure 2.9: Electronic phase separation in manganites. (a) Dark-field transmission electron microscope (TEM) image of $La_{2/8}Pr_{3/8}Ca_{3/8}MnO_3$ (LPCMO) taken at $T = 20$ K The dashed line is guides for the eye. (b) Scanning tunneling spectroscopic (STS) images (610 nm $\times$ 610 nm) of LCMO ($x \sim 0.3$) taken at slightly below T_C (~ 220 K). $\mathrm{d}I/\mathrm{d}V$ at a bias voltage of 3 V are plotted. Each panel, from left to right and top to bottom, shows the images taken under the magnetic fields of 0, 0.3, 1, 3, 5, and 9 T. Panel (a) adapted from Ref. [23] and (b) from [24].

resistivity.

The phase separation between the AFM-I and FM-M phases are experimentally confirmed in several studies [23, 24]. Figure 2.9(a) shows the dark-field transmission electron microscope (TEM) image of $La_{2/8}Pr_{3/8}Ca_{3/8}MnO_3$ (LPCMO, $T_C \sim 55$ K) at $T = 20$ K obtained from the superlattice peak of charge order [23]. The dark and bright areas indicate the charge-ordered and metallic regions, respectively. This image clearly indicates that charge-ordered insulating domain still exists even below T_C in a sub-micrometer scale, supporting the phase-separation model. Figure 2.9(b) shows the scanning tunneling spectroscopic (STS) images of LCMO ($x \sim 0.3$) taken at slightly below T_C (~ 220 K) [24]. Each panel, from left to right and top to bottom, shows the images taken under the magnetic fields of 0, 0.3, 1, 3, 5, and 9 T. The spatial variations in the electronic phases in a sub-micrometer scale and the transition from insulating (light color) to metallic (dark color) domains by applying magnetic field are clearly observed. Note that this inhomogeneity in electronic phases is generally irrelevant of that of the surface topology, namely, it is an intrinsic property of CMR manganites [24].

2.3 Physical properties of TMO thin films

When TMOs are grown in the form of thin films, their physical properties are governed not only by the factors mentioned above, but also by additional factors characteristic of thin films, such as their thickness, substrate, and surface and interfaces with neighboring layers. In this section, physical properties of TMO thin films, especially of manganites, are discussed.

Effect of epitaxial strain

When a TMO film is grown on the substrate, its in-plane lattice constants tend to be the same as those of the substrate. Thus, the film undergoes a compressive or tensile strain depending on the difference of the lattice constants between the film and substrate. This is called epitaxial strain and can largely affect the electronic phases of thin films. In general, the epitaxial strain is gradually relaxed as the thickness of the film increases. In addition, the strength of the epitaxial strain depends on the growth conditions of the films.

For example, Konishi *et al.* [19] have investigated the electric and magnetic properties of LSMO thin films grown on various substrates: $SrTiO_3$ (001) (STO), $LaAlO_3$ (001) (LAO), and $La_{0.3}Sr_{0.7}Al_{0.35}Ta_{0.35}O_9$ (001) (LSAT). which apply a tensile, compressive, and almost no strain, respectively, along the in-plane directions of the film. The results are summarized in Fig. 2.10 [19]. The LSMO ($x = 0.3, 0.5$) films, which are in the FM-M phase in the bulk, tend to turn into the AFM-I phases under the epitaxial strain (STO/LAO substrate), while the physical properties are almost the same as those of the bulk in the case of the LSAT substrate. The experimental phase diagram is summarized in Fig. 2.10(b). From the comparison with the first-principles calculations [Fig. 2.10(c)], it has been shown that the ground-state spin configuration is 'A-type' antiferromagnetism [top-right picture of Fig. 2.10(a)] in the case of the large tensile strain (STO) and 'C-type' antiferromagnetism (top-left picture) in the case of the large compressive strain (LAO). They also show from the first-principles calculations that the Mn $d_{x^2-y^2}$ ($d_{3z^2-r^2}$) orbital is preferentially occupied in the case of tensile (compressive) strain [19]. This can be understood as a consequence of lowering of the symmetry from the cubic to the tetragonal crystal structure (Fig. 2.6).

Surface and interfacial effect

The electronic structure at the surface or the interfaces of the film is in general different from that in the bulk, and thus novel physical properties

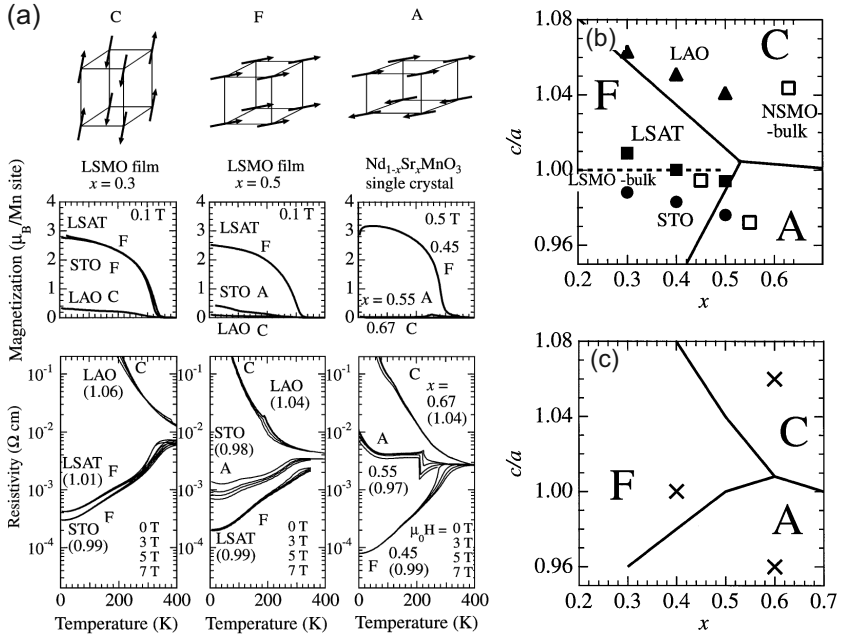

Figure 2.10: Physical properties of LSMO thin films grown on different substrates. (a) Expected magnetic phases (top), temperature- (T-)dependence of the magnetization (middle), and T-dependence of the resistivity and magnetoresistance (bottom), for the LSMO thin films with $x = 0.3$ (left), $x = 0.5$ (center) and the NSMO single crystals (right). C, F, and A denote the C-type antiferromagnetic, ferromagnetic, and A-type antiferromagnetic phases, respectively. The LSMO thin films have been grown on the $SrTiO_3$ (001) (STO), $LaAlO_3$ (001) (LAO), and the $La_{0.3}Sr_{0.7}Al_{0.35}Ta_{0.35}O_9$ (001) (LSAT) substrates. (b)(c) Experimental (b) and calculated (c) phase diagrams as functions of the Sr concentration x and the degree of the strain c/a (the ratio of the out-of-plane lattice constant c to the in-plane lattice constant a). Adapted from Ref. [19].

are often observed there. One of the most outstanding examples in TMO heterostructures is the emergence of electric conductivity at the LAO/STO interface [25]. Despite that both LAO and STO are band insulators, the interface of them exhibits electric conduction, as shown in Fig. 2.11(a) [25]. Other studies on the LAO/STO heterostructures have shown that superconductivity [26] and possible ferromagnetism [27] appear at ultralow temperature ($T \lesssim 0.3$ K). This LAO/STO heterostructure system has been studied extensively in order to clarify the origin of the metallicity at the interface. In the early study by Ohtomo et al. [25], the metallicity has been ascribed to the electron transfer from LAO to STO induced by the polar nature of LAO: As shown in Figs. 2.11(b) [28], LAO consists of the alternate stack-

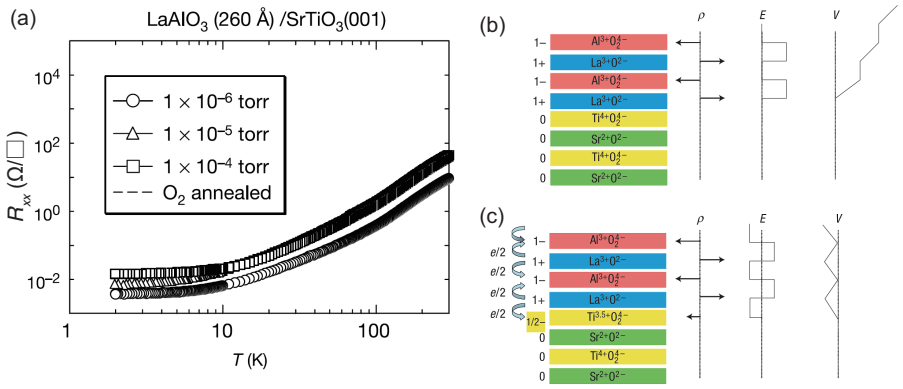

Figure 2.11: Interfacial metallicity between LAO and STO. (a) Sheet resistivity (R_{xx}) of the LAO (26 nm) thin film grown on the STO (001) substrate. (b)(c) Polar catastrophe model. (c) and (b) respectively represent the cases where interfacial electron transfer occurs and does not occur. Panel (a) adapted from Ref. [25] and (b)(c) from Ref. [28].

ing of the LaO^+ and AlO_2^- layers. Such a stacking structure is, however, energetically unfavorable because the Coulomb potential diverges as shown in the right picture of Figs. 2.11(b) [28]. In order to avoid this energy divergence, electrons are doped into the interfacial TiO_2 layer, as shown in Fig. 2.11(c), and the valence of Ti are shifted from 4+ to 3.5+. Hence, the metallic conduction appears at the interface. This hypothesis, known as the 'polar catastrophe' model, has been tested both experimentally and theoretically for a long time. Although some studies support the model, consensus has not been reached because other studies have shown that different mechanism such as oxygen vacancy [29] or chemical interdiffusion [30] play more important roles.

The physical properties of manganite thin films are also different from those of the bulk due to the surface and interfacial effects. It has been reported that the magnetic moment and Curie temperature of ferromagnetic manganite thin films can be much suppressed near the surface and interfaces [5–8]. For example, magnetic tunneling junctions (MTJs) composed of half-metallic LCMO or LSMO exhibit lower performances than expected (e.g., lower Curie temperature or smaller magnetoresistance), due to the suppression of the half metallicity near the interfaces with the barrier layer [5–7]. Another study has shown by magnetization-induced secondharmonic generation (MSHG), which is a probe to study the magnetizatic properties at the interfaces, that ferromagnetic LSMO forms a magnetically 'dead layer' at the interface with STO, as shown in Fig. 2.12 [8]. It has also shown that this dead layer can be suppressed by inserting two unit cells (UCs) of $LaMnO_3$,

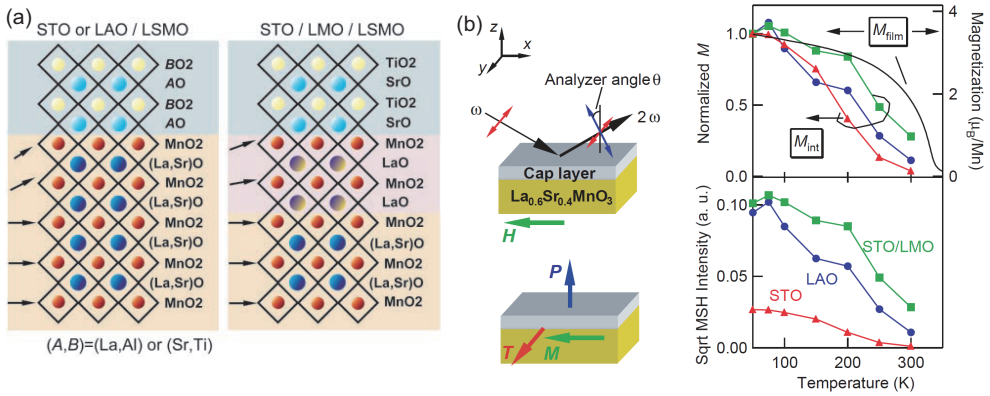

Figure 2.12: Magnetic properties of LSMO ($x = 0.4$) thin films at the interfaces studied by magnetization-induced secondharmonic generation (MSHG). (a) Structure of the samples studied. In the left panel, two unit cells (UCs) of STO or LAO are deposited on the LSMO thin films. In the right panel, two UCs of $LaMnO_3$ are inserted at the interface. (b) Experimental geometry of MSHG (left) and the intensities of MSHG for the three films mentioned above. Adapted from Ref. [8].

suggesting that hole doping at the interface may play an important role in the formation of the dead layer [8]. Thus, clarifying the electric and magnetic properties at the interfaces and understanding the origin of them has been of great interest, both from scientific and application point of view.

Dimensional effect

Dimensionality is another factor which governs the physical properties of thin films. When the thickness of the film is reduced down to a few unit cells (UCs), the system behaves like two-dimensionally rather than three-dimensionally. This leads to the decrease of the bandwidth due to the reduced number of bonds along the out-of-plane direction [31–38], or the modulation of the band structure by the formation of the quantum-well states [39]. Indeed, thickness-dependent metal-to-insulator transitions and magnetic transitions are observed in many TMOs, such as paramagnetic metals $SrVO_3$ [31] and $LaNiO_3$ [32, 33], and ferromagnetic metals LSMO [34–36] and $SrRuO_3$ [37, 38]. Figure 2.13 shows the thickness-dependent metal-to-insulator transition observed in ferromagnetic LSMO thin films [35] as an example. As shown by the transport and magnetization data in Figs. 2.13(a) and 2.13(b), respectively, the LSMO ($x = 0.3$) films exhibit a metal-to-insulator transition and concomitant weakening of ferromagnetism with decreasing thickness. The photoemission spectra of the LSMO ($x = 0.4$) thin

films [Fig. 2.13(c)] show the opening of an energy gap at the Fermi energy (E_F) below the critical thickness of $\sim$ 6-8 UCs, indicating that the films turn into an insulating phase. This large energy gap ($\gtrsim$ 0.5 eV) suggests that this MIT is different from that observed in conventional metal thin films induced by weak localization or Anderson localization [40–44], and that electron correlation has to be taken into account in order to explain the mechanism of the MIT.

It should be noted, however, the decrease of the film thickness also results in the enhancement of the epitaxial strain and relative enhancement of the surface and interfacial effects compared to the bulk. It is therefore needed to separate these effects in order to correctly understand the physical origin of the thickness-dependent phenomena.

Chemical effect

In addition to the abovementioned effects specific to thin films, chemical effect cannot be ignored. Since the chemical states of thin films are sensitive compared to bulk materials, significant modification of physical properties can occur in thin films. Formation of oxygen vacancies, off-stoichiometry, and intermixing of cations at the interface can be possible origins for this. Figure 2.14 shows a study on the valence state of Mn at the surface of LSMO ($x = 0.3$) thin films by x-ray absorption spectroscopy (XAS) as an example [45]. Figure 2.14(A) shows that the spectral difference (spectrum c) between two different LSMO thin films (spectra a and b) is nearly identical to the calculated (spectrum d) and experimental (spectrum e) XAS spectra of Mn^{2+} ions. This suggests that there are some Mn^{2+} ions in the grown LSMO thin films, despite that the valence of Mn should be in between Mn^{3+} and Mn^{4+} in bulk manganites. By comparison between spectra b and c, it is suggested that the peak or shoulder structure at the photon energy of 640 eV in spectra a and b is the signal from the Mn^{2+} ions. The amount of Mn^{2+} can be controlled by changing the annealing conditions after the film growth, as shown in Fig. 2.14(B). In order to suppress the effect of these extrinsic Mn^{2+}, the films have been annealed in an oxygen atmosphere prior to the measurements in Chapter 5, 6, and 7.

2.4 Magnetic anisotropy of LSMO thin films and orbital occupation

It has been reported that, in ferromagnetic manganite thin films, the magnetic anisotropy changes depending on the substrates of the films [46, 47].

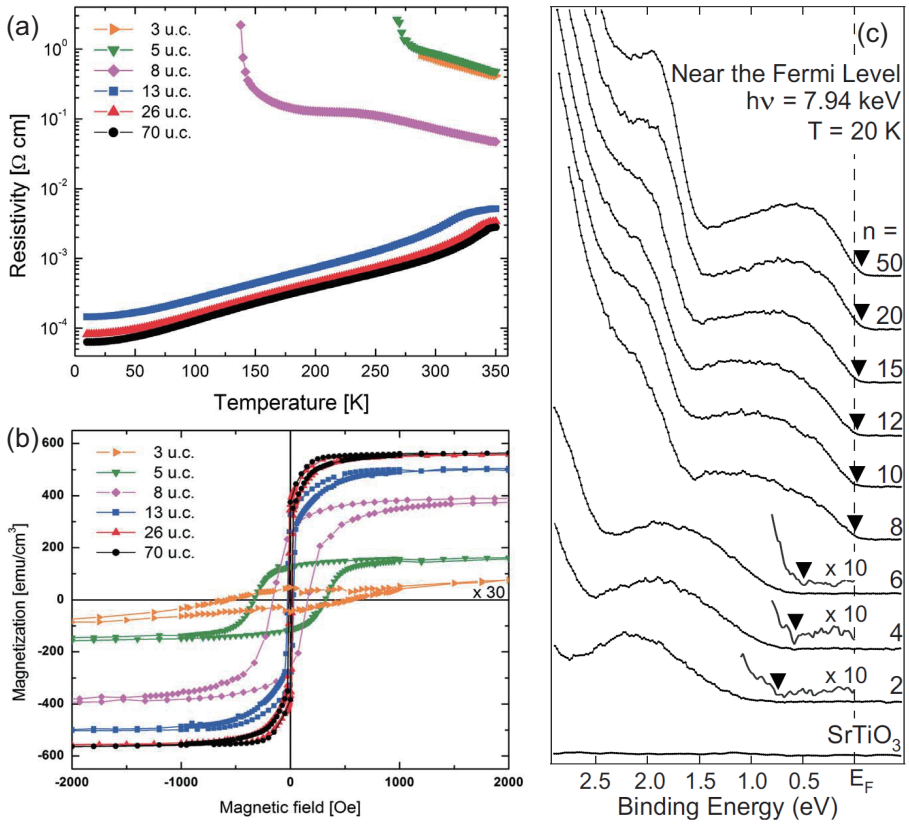

Figure 2.13: Thickness-dependent phase transition in LSMO thin films grown on STO (001) substrates. (a) Transport properties of LSMO ($x = 0.3$) thin films. (b) Magnetization curves for various thicknesses of LSMO ($x = 0.3$) measured at $T = 10$ K. (c) Hard x-ray photoemission spectra for various thicknesses of LSMO ($x = 0.4$) thin films. n denotes the thickness of LSMO in unit cells. Panels (a)(b) adapted from Ref. [35] and (c) from Ref. [28].

Figures 2.15(a)-(c) show the magnetic hysteresis curves of LSMO ($x = 0.33$) thin films grown on three different substrates, $LaAlO_3$ (001) (LAO), $SrTiO_3$ (001) (STO), and $La_{0.3}Sr_{0.7}Al_{0.35}Ta_{0.35}O_9$ (001) (LSAT). Due to the differences in the lattice constants between LSMO and the substrates, the film undergoes a compressive strain from the LAO substrate, a tensile strain from the STO substrate along the in-plane direction, and is almost unstrained for the LSAT substrate [19]. The magnetization curves in Fig. 2.15(a)-(c) clearly shows that the magnetic easy axis is along the out-plane direction for the LAO substrate and is in-plane direction for the STO and LSAT substrates [46]. (Note that, although LSMO on LSAT has a nearly cubic crystal structure, it exhibits in-plane easy axis because of the energy increase by the

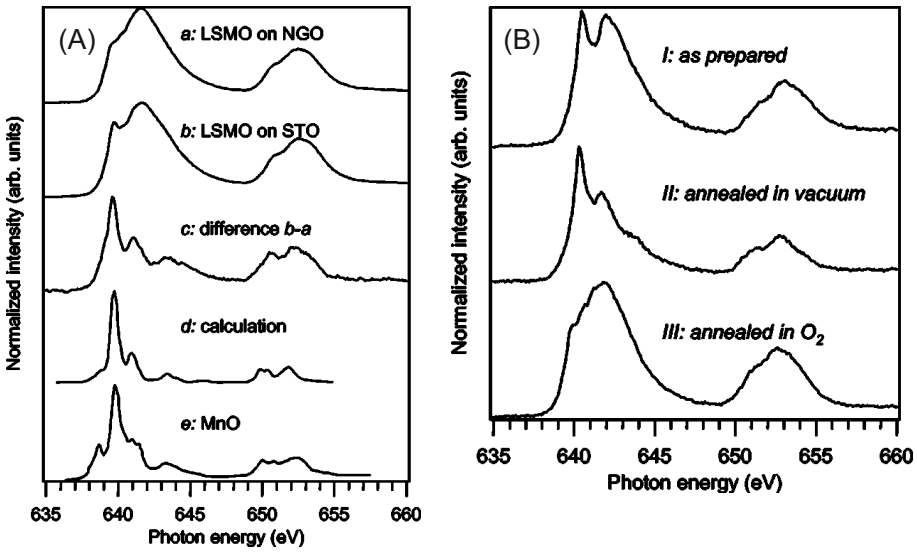

Figure 2.14: Valence state of Mn at the surface of LSMO ($x = 0.3$) thin films studied by x-ray absorption spectroscopy (XAS). (A) XAS spectra for two different LSMO films grown on (a) $NdGaO_3$ (NGO) and (b) STO substrates. c is the difference spectra obtained by $\mathrm{a} - \mathrm{b} \times C$, where C is an appropriate weight constant. d and e are the calculated and experimental XAS spectra of Mn^{2+} ions, respectively. (B) XAS spectra of an epitaxial LSMO film grown on STO with various annealing conditions. (I), (II), and (III) are the XAS spectra for the as prepared film, the film annealed in vacuum, and the film annealed in oxygen atmosphere, respectively. Adapted from Ref. [45].

demagnetizing field in the case of out-of-plane magnetization). It can also be seen that the magnetic anisotropy is stronger for the STO substrate than the LSAT substrate. Similar behavior is also observed by magnetic force microscopy (MFM), as shown in Figs. 2.15(d) and (e) [47]. The maze pattern observed at zero field for the LSMO/LAO film [right panel in (d)] indicates that the magnetization is along the out-of-plane direction.

It is expected that the magnetic anisotropy of ferromagnetic materials are deeply related to their electron orbitals. In order to clarify the preferential orbital occupation in LSMO thin films, x-ray linear dichroism (XLD) spectroscopy has been performed [48–51]. In XLD spectroscopy, the difference in the x-ray absorption spectra are measured for two different linear polarizations (in-plane or out-of-plane polarizations), and information about the preferential orbital occupation is deduced from the difference spectra (see Sec. 3.3 for the principles of XLD). In the case of perovskite-type manganites, it is expected that the $x^2 - y^2$ ($3z^2 - r^2$) orbital has a lower energy than the $3z^2 - r^2$ ($x^2 - y^2$) orbital in the case of tensile (compressive) substrate

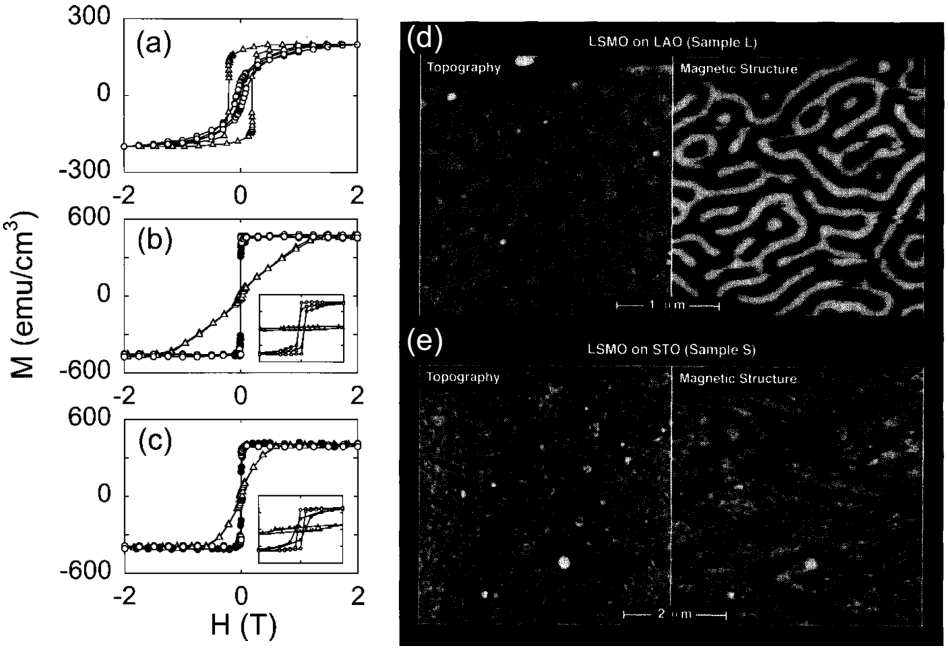

Figure 2.15: Substrate dependence of the magnetic anisotropy in ferromagnetic LSMO thin films. (a)-(c) Magnetic hysteresis curves at $T = 5$ K of LSMO ($x = 0.33$) thin films grown on $LaAlO_3$ (001) (LAO) (a), $SrTiO_3$ (001) (STO) (b), and $La_{0.3}Sr_{0.7}Al_{0.35}Ta_{0.35}O_9$ (001) (LSAT) (c) substrates. In (a) and (b), the magnetic field is applied along the in-plane [110] (open circles), in-plane [100] (closed circles), and the out-of-plane [001] (triangles) directions. In (c), the field is applied along the in-plane [100] (open circles), in-plane [010] (closed circles) and the out-of-plane [001] (triangles) directions. Insets show the expanded data in the range of $|H| \leq 400$ Oe. (d),(e) Topographic (left) and magnetic (right) images of LSMO ($x = 0.3$) thin films at zero field and room temperature, measured using atomic force microscopy (AFM) and magnetic force microscopy (MFM), respectively. (d) and (e) show the images for the LSMO thin films grown on LAO and STO substrate, respectively. Panels (a)-(c) reproduced from Ref. [46] and panels (d) and (e) adapted from Ref. [47].

due to the tetragonal crystal field created by the substrate. This means that the $x^2 - y^2$ ($3z^2 - r^2$) orbital should be more preferentially occupied in the LSMO/STO (LSMO/LAO) substrate. Against this expectation, however, the XLD results show that the $3z^2 - r^2$ orbital is always more preferentially occupied irrespective of the substrate [48–51]. Figs. 2.16(a) and 2.16(b) shows the XLD spectra for the LSMO ($x = 0.3$) thin films grown on the STO (tensile) and LAO (compressive) substrates, respectively [50]. The difference spectra between the in-plane and out-of-plane polarizations (green

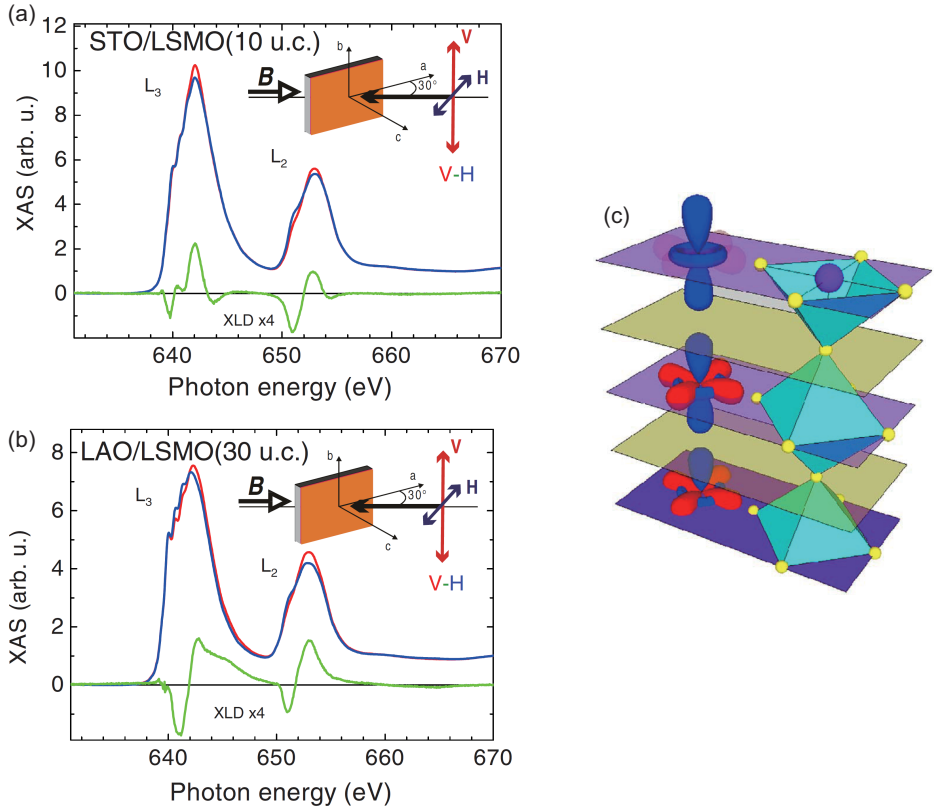

Figure 2.16: (a),(b) X-ray linear dichroism (XLD) spectra at $T = 10$ K of LSMO ($x = 0.3$) thin films grown on the (a) STO (001) (tensile) and (b) LAO (compressive) substrates. The red and blue spectra are the absorption spectra for in-plane and out-of-plane linear polarizations, respectively, and the green one is the difference spectra. (c) Panels (a) and (b) adapted from Ref. [50] and (c) from Ref. [51].

curve) have the same sign for both the substrates, indicating that the orbital occupation is unchanged by the substrates. This has been so far attributed to the broken inversion symmetry at the surface of the film [49–51]: As shown in Fig. 2.16(c), the Mn atoms at the surface lack one apical oxygen. This may change the energy level of the $3z^2 - r^2$ orbital and thus lead to the preferential occupation of the $3z^2 - r^2$ orbital. Since XLD is a relatively surface-sensitive experiment (with a probing depth of a few nm), such a surface effect may complicate the interpretation of the experimental results. It is therefore desired to directly probe the orbital occupation of Mn in the bulk, especially that which is related to the ferromagnetism of the film, in order to discuss the relationship between the orbital occupation and the magnetic anisotropy.

Chapter 3

Soft x-ray magnetic dichroism

In this chapter, the basic principles of x-ray magnetic circular dichroism (XMCD) and x-ray magnetic linear dichroism (XMLD) are summarized.

3.1 X-ray absorption spectroscopy

X-ray absorption spectroscopy (XAS) is a spectroscopic technique in which the absorption coefficient of a material for x rays is measured as a function of photon energy. Figure 3.1 schematically illustrates the principles of XAS. When x rays are incident to a material, the electron transitions from core levels to valence bands occur by photoabsorption. Within the dipole approximation, the absorption intensity can be calculated as below using Fermi's golden rule:

$$I(h\nu) \propto \sum_{i,f} |\langle f|e\boldsymbol{E}\cdot\boldsymbol{r}|i\rangle|^2 \delta(E_i - E_f - h\nu), \tag{3.1}$$

where $|i\rangle$ is the initial core-level state, $|f\rangle$ is the final state in the valence band, E_i and E_f, respectively, are the energies of the initial and final states, $h\nu$ is the photon energy of the x ray, $\boldsymbol{E}$ is the electric field of the x ray, and $\boldsymbol{r} = (x, y.z)$ is the position operator of the electron. Since the initial core-level states are well localized and have constant energies, the absorption intensity $I(h\nu)$ reflects the density of states (DOS) of the final (valence-band) states. From the spectral line shapes of XAS, one can obtain information about the electronic states of the valence bands, such as the chemical valence, hybridization strength, symmetry of crystal field, and so on. One of the strengths of XAS that it is an element-selective technique because the binding energies of the core-level electrons are specific to each element. For $3d$ transition-metal oxides, the $2p$-$3d$ absorption edges of transition metals or the $1s$-$2p$ absorption edge of oxygen are often utilized in order to investigate

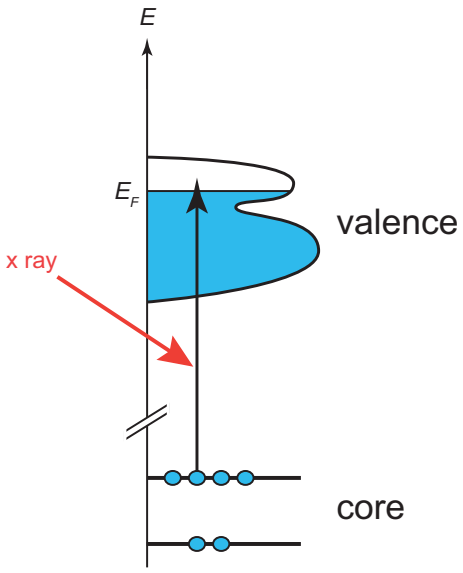

Figure 3.1: Principles of x-ray absorption spectroscopy (XAS) based on the one-electron model.

the electronic structure of the valence bands. These transition correspond to the photon-energy regime of soft x rays ($h\nu \sim$ 100-2000 eV). Synchrotron radiation is generally utilized for XAS experiments because high-flux photons are required and the photon energy of x rays has to be variable.

In contrast to optical or infrared spectroscopy, it is difficult to directly obtain the absorption coefficient by measuring the intensity of the transmitted light in the case of soft x rays unless the sample is thin enough, because of the rather short penetration depth of x rays (typically a few hundred nm). There are some alternative detection methods to deduce the absorption intensity in XAS. The widely used methods are the total-electron-yield (TEY) mode and the total-fluorescence-yield (TFY) mode (Fig. 3.2). The TEY mode is the method to measure the total amount of electrons emitted from the sample through photoelectric or Auger effects. In the TEY mode, the sample is electrically in contact with the ground via a picoammeter. When x rays are absorbed by the sample, electrons flow into the samples from the ground in order to compensate the emitted electrons, producing the electric current. One can deduce the amount of the emitted electrons and thus the absorption coefficient by measuring this compensation current using the picoammeter. In the TFY mode, the intensity of the fluorescence associated with the x-ray absorption is measured using a photodiode or a multi channel plate.

The probing depths of the TEY and TFY modes are typically about 5 nm and 100 nm, respectively, which means that the TFY mode is more bulk

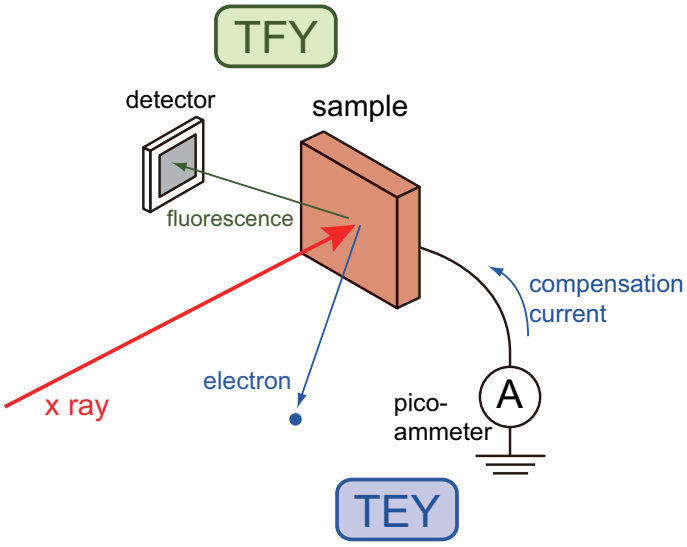

Figure 3.2: Total-electron-yield (TEY) and total-fluorescence-yield (TFY) modes as the detection methods of XAS.

sensitive than the TEY mode. The TEY mode cannot be applied to samples which have too high resistivities, whereas the TFY mode is applicable to both conducting and insulating samples. However, the TFY mode has disadvantages that the quantum efficiency of fluorescence is low and, therefore, that the signal-to-noise ratio is low. In addition, the spectral line shape can be distorted due to 'self-absorption effect' [52, 53]. In this thesis, the TEY mode has been adopted in all the experiments because the self-absorption effect can significantly affect the spectral line shapes of XAS.

3.2 X-ray magnetic circular dichroism (XMCD)

3.2.1 Principles of XMCD

X-ray magnetic circular dichroism (XMCD) is defined as the difference in the XAS spectra between the right- and left-handed circularly-polarized x rays due to the presence of magnetization. XMCD appears when the net magnetic moment of a certain element in a sample is finite, as in ferromagnets, ferrimagnets, or canted antiferromagnets (weak ferromagnets). Figure 3.3(a)(b) schematically illustrates the measurement setup of XMCD and the spectra which can be obtained. The sample is placed in a magnetic field, and circularly-polarized x rays produced by the synchrotron light source are irradiated onto the sample [Fig. 3.3(a)]. If the sample is magnetized parallel or antiparallel to the incident x rays, differences in the XAS spectra

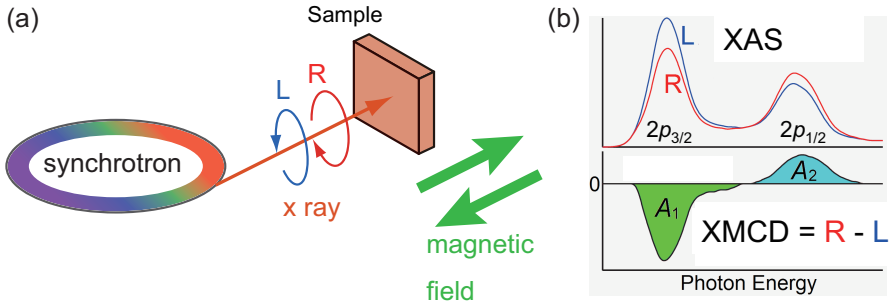

Figure 3.3: Schematic diagram of x-ray magnetic circular dichroism (XMCD). (a) Experimental setup. (b) XAS spectra for the right- and left-handed circular polarization and the difference spectra, i.e., XMCD spectra.

appear between the right- and left-handed polarization, namely, the XMCD spectrum is obtained [Fig. 3.3(b)]. XMCD spectra can be measured either by reversing the light polarization or the direction of the magnetic field. As explained in the following sections, one can obtain information about the microscopic magnetic properties of the sample from XMCD.

One of the most important advantages of XMCD is that one can estimate the spin and orbital magnetic moments separately and quantitatively from the integrated intensities of the XMCD spectra, as described in Sec. 3.2.2. In addition, one can estimate the magnetic moment of a specific magnetic element of interest because XAS is an element-specific probe, as mentioned above. XMCD also has the advantage that it is applicable to systems which contain only small amount of magnetic atoms such as ultra-thin films or dulute magnetic semiconductors, thanks to its high sensitivity. In such systems, one can deduce the *intrinsic* magnetization (M-H) curves of the systems using XMCD, which is difficult by conventional magnetization measurements such as superconducting quantum interference device (SQUID) magnetometry due to the large diamagnetism or paramagnetism of the substrates or host materials. This properties shall be utilized in Chaps. 5 and 6.

The physical origin of XMCD can be explained as follows: The absorption intensity for the right- and left-handed circularly-polarized x rays (hereafter denoted as the σ^+ and σ^- light, respectively) can be calculated using Eq. (3.1). The $\boldsymbol{E}\cdot\boldsymbol{r}$ term in Eq. (3.1) for the $\sigma^\pm$ light is proportional to $x \pm iy$, leading to the selection rules $\Delta l_z = \pm 1$ and $\Delta s_z = 0$, where Δl_z and Δs_z are the changes of the orbital and spin angular momenta along the z axis after the x-ray absorption, respectively. Due to these selection rules and spin-orbit splitting of the core-hole energy levels, the transition probabilities from the $2p$-core to $3d$-valence levels (i.e., the absorption inten-

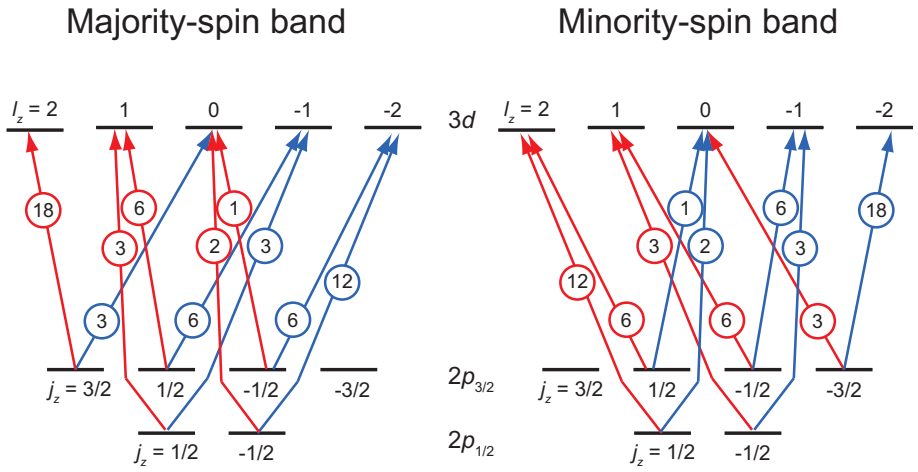

Figure 3.4: Relative transition probabilities from the $2p$-core to $3d$-valence levels for the right- (red) and left-handed (blue) circularly-polarized x rays, calculated using Eq. (3.1).

sities) are asymmetric between the σ^+ and σ^- x rays, as shown in Fig. 3.4. Although this asymmetry is cancelled out as a whole if the majority- and minority-spin bands are equally occupied, it remains if the system is spin-polarized and the transition probability into the minority-spin band is larger than that of the majority-spin band. For example, if the majority-spin band is fully occupied, only the transitions into the minority-spin (right-hand side of Fig. 3.4) has to be considered and the relative transition probabilities $I^{\pm}$ for the $\sigma^{\pm}$ x rays can be calculated as follows:

$$\begin{aligned} I^+ \ (2p_{3/2} \rightarrow 3d) &= 6+6+3=15, \\ I^- \ (2p_{3/2} \rightarrow 3d) &= 1+6+18=25, \\ I^+ \ (2p_{1/2} \rightarrow 3d) &= 12+3=15, \\ I^- \ (2p_{1/2} \rightarrow 3d) &= 2+3=5. \end{aligned}$$

Thus, it follows that the $2p_{3/2} \rightarrow 3d$ absorption edge exhibits negative XMCD signals ($I^+ - I^- < 0$) and the $2p_{3/2} \rightarrow 3d$ edge positive XMCD signals ($I^+ - I^- > 0$). If there is a finite orbital moment and the band filling for each l_z are different, this can further result in the asymmetry of the transition probabilities into each l_z levels and hence can be an origin of XMCD. In this way, XMCD is observed by the presence of either spin or orbital magnetic moment.

3.2.2 XMCD sum rules

Thole *et al.* [54] and Carra *et al.* [55] have theoretically shown that one can separately calculate the orbital ($\boldsymbol{M}_{\rm orb}$) and spin magnetic moments ($\boldsymbol{M}_{\rm spin}$) projected along the incident x rays from the integrated intensities of the XMCD spectra. Their results for the $2p \rightarrow 3d$ transition are as follows (in unit of μ_B/atom):

$$\hat{\boldsymbol{P}} \cdot \boldsymbol{M}_{\rm orb} = -\frac{4\int_{L_3+L_2}(\mu^+ - \mu^-)\mathrm{d}\nu}{3\int_{L_3+L_2}(\mu^+ + \mu^-)\mathrm{d}\nu}(10 - N_d), \tag{3.2}$$

$$\begin{aligned} \hat{\boldsymbol{P}} \cdot \boldsymbol{M}_{\rm spin}^{\rm eff} &\equiv \hat{\boldsymbol{P}} \cdot \left(\boldsymbol{M}_{\rm spin} + \frac{7}{2}\boldsymbol{M}_{\rm T} \right) \\ &= -\frac{2\int_{L_3}(\mu^+ - \mu^-)\mathrm{d}\nu - 4\int_{L_2}(\mu^+ - \mu^-)\mathrm{d}\nu}{\int_{L_3+L_2}(\mu^+ + \mu^-)\mathrm{d}\nu}(10 - N_d). \end{aligned} \tag{3.3}$$

where $\hat{\boldsymbol{P}}$ is the unit vector along the x rays (taken to be antiparallel to the wavevector $\boldsymbol{k}$), μ^+ (μ^-) is the XAS intensity for the positive (negative) polarizations, L_3 (L_2) is the $2p_{3/2} \rightarrow 3d$ ($2p_{1/2} \rightarrow 3d$) absorption edge, and N_d is the number of electrons in the $3d$ band. The spin magnetic moment deduced from Eq. (3.3) is called 'effective' spin magnetic moment $\boldsymbol{M}_{\rm spin}^{\rm eff}$ which contains an additional term $(7/2)\boldsymbol{M}_{\rm T}$. This additional term is called 'magnetic dipole' [55], which shall be described in detail in the next subsection. The magnetic dipole $(7/2)M_{\rm T}$ is generally small compared to the spin magnetic moment $M_{\rm spin}$ when the system has a high crystal symmetry, and is often neglected to a first approximation (i.e., $\boldsymbol{M}_{\rm spin}^{\rm eff} \simeq \boldsymbol{M}_{\rm spin}$). As can be seen from these equations, XMCD is sensitive to the magnetic moment component parallel the incident x rays. Using the spectral intensities schematically drawn in Fig. 3.3(b), the projection of the orbtial ($\hat{\boldsymbol{P}} \cdot \boldsymbol{M}_{\rm orb}$) and effective spin magnetic moments ($\hat{\boldsymbol{P}} \cdot \boldsymbol{M}_{\rm spin}^{\rm eff}$) are proportional to $A_1 - A_2$ and $A_1 + 2A_2$, respectively. This means that $\hat{\boldsymbol{P}} \cdot \boldsymbol{M}_{\rm orb}$ is proportional to the asymmetry of the XMCD spectra and $\hat{\boldsymbol{P}} \cdot \boldsymbol{M}_{\rm spin}^{\rm eff}$ is approximately proportional to the peak height (or the dip depth) of the spectra. Equations (3.2) and (3.3) are called XMCD sum rules and have been widely used to estimate the spin and orbital magnetic moments of the element quantitatively.

The validity of the XMCD sum rules was tested experimentally by Chen et al. [56] They grew Fe and Co thin films on thin (~ 1 μm-thick) parylene substrates and measured the XMCD spectra with high accuracy by directly measuring the intensities of transmitted x rays. Figure 3.5 shows the obtained XAS and XMCD spectra of the Fe thin film, and the analysis method to apply the XMCD sum rules. The absorption coefficients for the positive

and negative magnetic fields, i.e., the XAS spectra [Fig. 3.5(b)], have been obtained from the transmission intensities [Fig. 3.5(a)]. From Fig. 3.5(b), the XMCD spectra [Fig. 3.5(c)], the XAS spectra summed over both the magnetic-field directions [Fig. 3.5(d)], and their integrals with respect to $h\nu$ have been calculated. Using the integrated values p, q, and r shown in Figs. 3.5(c) and 3.5(d), the XMCD sum rules [Eqs. (3.2) and (3.3)] can be rewritten as follows:

$$\hat{\boldsymbol{P}} \cdot \boldsymbol{M}_{\rm orb} = -\frac{4q}{3r}(10 - N_d), \tag{3.2'}$$

$$\hat{\boldsymbol{P}} \cdot \boldsymbol{M}_{\rm spin}^{\rm eff} = -\frac{6p - 4q}{r}(10 - N_d). \tag{3.3'}$$

Thus $M_{\rm orb}$ and $M_{\rm spin}^{\rm eff}$ along the x-ray incident direction can be obtained. They showed that the magnetic moments deduced from the XMCD sum rules agree with the ones deduced in previous gyromagnetic ratio measurements and first-principles calculations within an accuracy of several percent, demonstrating the validity of the XMCD sum rules [56].

3.2.3 Interpretation of the magnetic dipole $M_{\rm T}$

The magnetic dipole $\boldsymbol{M}_{\rm T}$ in Eq. (3.3) is defined by the following equations using the magnetic dipole *operator* $\boldsymbol{T}$ [55]:

$$\boldsymbol{T} \equiv \boldsymbol{S} - 3(\boldsymbol{S} \cdot \hat{\boldsymbol{r}})\hat{\boldsymbol{r}}, \tag{3.4}$$

$$\boldsymbol{M}_{\rm T} \equiv -g\mu_B \langle \boldsymbol{T} \rangle, \tag{3.5}$$

where g ($\simeq 2$) is the g-factor of the electron, $\hbar\boldsymbol{S}$ is the spin angular momentum operator ($\boldsymbol{M}_{\rm spin} = -g\mu_B\langle \boldsymbol{S} \rangle$), and $\hat{\boldsymbol{r}}$ is a unit-vector operator parallel to the electron position operator $\boldsymbol{r}$ ($\hat{\boldsymbol{r}} \equiv \boldsymbol{r}/|\boldsymbol{r}|$). Here, we define the following second-order tensor operator $\boldsymbol{Q}$ [2, 3],

$$\boldsymbol{Q} = \boldsymbol{1} - 3\hat{\boldsymbol{r}} \otimes \hat{\boldsymbol{r}}, \tag{3.6}$$

or using its elements Q_{ij}'s,

$$Q_{ij} \equiv \delta_{ij} - 3\hat{r}_i\hat{r}_j \qquad (i, j = x, y, z). \tag{3.6'}$$

Then, the operator $\boldsymbol{T}$ can be rewritten as follows:

$$\boldsymbol{T} = \boldsymbol{Q} \cdot \boldsymbol{S}, \tag{3.7}$$

$$T_i = \sum_j Q_{ij} S_j. \tag{3.7'}$$

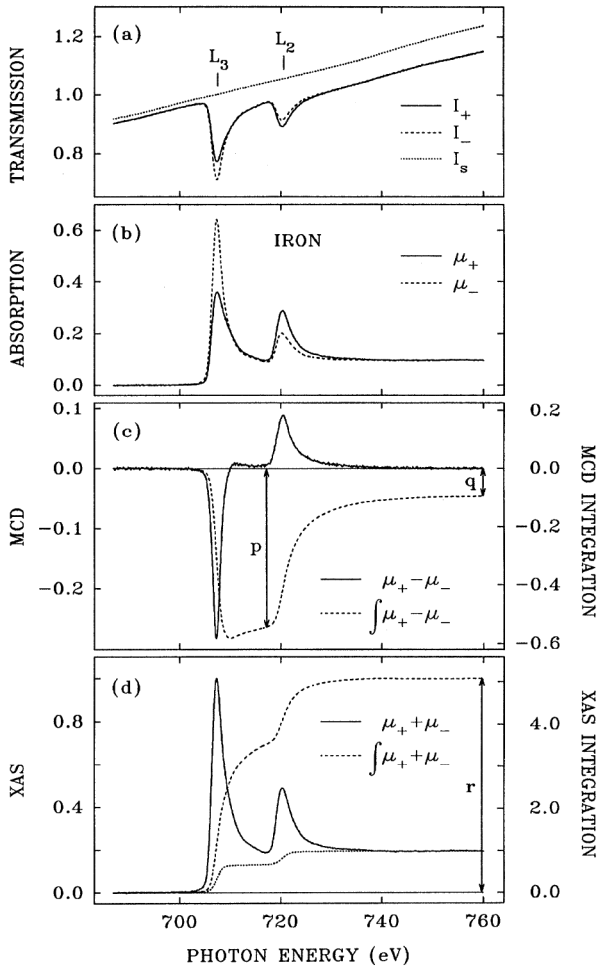

Figure 3.5: XAS and XMCD spectra of an Fe thin film measured by the transmission method and explanation of the sum-rule analysis. XMCD is measured by reversing the direction of the magnetic field. (a) Transmission intensities for both the positive (solid) and negative (dashed) magnetic-field directions. Dotted curve shows the background from the substrate. (b) XAS spectra for both the field directions obtained from the data in (a). (c) XMCD spectrum calculated from (b) (solid) and its integral with respect to photon energy (dashed). (d) XAS spectrum summed over both the field directions (solid) and its integral with respect to photon energy (dashed). Dotted curve represents a two-step-like background originating from the transition from Fe $2p$ to energy levels higher than Fe $3d$, which is to be subtracted when applying the XMCD sum rules. The values p, q, and r, indicated in (c) and (d), are the integrals which appear in the XMCD sum rules. Reproduced from Ref. [56].

$\boldsymbol{Q}$ is an operator called electric quadrupole-moment tensor, and the expectation values of Q_{ij}'s represent the anisotropy of the charge density, namely, the anisotropy of the electron distribution. For example, the expectation value $\langle Q_{zz} \rangle = \langle 1 - 3\hat{z}^2 \rangle$ is positive if the charge density is higher in the xy-plane than along the z-axis (i.e., $\langle \hat{z}^2 \rangle$ is small) and is negative in the opposite case (i.e., $\langle \hat{z}^2 \rangle$ is large). Therefore, $\langle Q_{zz} \rangle$ becomes positive for the $d_{x^2-y^2}$ orbital and negative for the $d_{3z^2-r^2}$ orbital [2,3]. Detailed calculations show that $\langle Q_{zz} \rangle = +4/7$ for the $d_{x^2-y^2}$ orbital and $\langle Q_{zz} \rangle = -4/7$ for the $d_{3z^2-r^2}$ orbital [2, 3]. In this way, information about the orbital occupation can be deduced from the expectation values of Q_{ij}'s. Since the magnetic dipole operator $\boldsymbol{T}$ can be written as a product of $\boldsymbol{Q}$ and $\boldsymbol{S}$ as shown in Eq. (3.7), $\boldsymbol{T}$ and $\boldsymbol{M}_{\mathrm{T}}$ reflect both the spin direction and the anisotropy of the electron distribution (i.e., the orbital occupation). If spin-orbit interaction (SOI) is weak as in $3d$ transition metals, Eq. (3.7) or (3.7') can be separated into spatial and spin parts and hence $\langle Q_{ij} S_j \rangle$ can be replaced by $\langle Q_{ij} \rangle \langle S_j \rangle$. Thus one obtains from Eqs. (3.5) and (3.7),

$$M_{\mathrm{T}}^i = \sum_j \langle Q_{ij} \rangle M_{\mathrm{spin}}^j. \tag{3.8}$$

If the crystal symmetry is high enough (higher than D_{2h}), $\langle Q_{ij} \rangle$ can be diagonalized by choosing the x, y, and z-axes parallel to the crystal axes [2], and thus we obtain

$$M_{\mathrm{T}}^i = \langle Q_{ii} \rangle M_{\mathrm{spin}}^i. \tag{3.9}$$

Equation (3.9) means that $\boldsymbol{M}_{\mathrm{T}}$ represents the anisotropic distribution of *spin-polarized* electrons; in other words, the *anisotropy of the spin-density distribution*. Figure 3.6 [21] schematically describes the relationship between $\boldsymbol{M}_{\mathrm{T}}$, $\boldsymbol{M}_{\mathrm{spin}}$ and the anisotropy of the electron distribution in the case where $\boldsymbol{M}_{\mathrm{spin}}$ is parallel to the z-axis. The magnetic dipole $\boldsymbol{M}_{\mathrm{T}}$ becomes parallel (antiparallel) to $\boldsymbol{M}_{\mathrm{spin}}$ for the $d_{x^2-y^2}$ ($d_{3z^2-r^2}$) orbitals and vanishes when the electron distribution is isotropic (e.g., the $d_{x^2-y^2}$ and $d_{3z^2-r^2}$ levels are equally occupied). Thus information about the orbital occupation of the spin-polarized electrons can be deduced by measuring $\boldsymbol{M}_{\mathrm{T}}$.

3.2.4 Relationship between M_{orb}, M_{T} and magnetic anisotropy

It has been theoretically predicted that the orbital magnetic moment M_{orb} and the magnetic dipole M_{T}, which can be deduced by XMCD, are closely related to magnetic anisotropy of ferromagnetic materials.

Bruno [57] has shown by using the second-order perturbation theory of spin-orbit interaction (SOI) and the tight-binding model that, for a ferro-

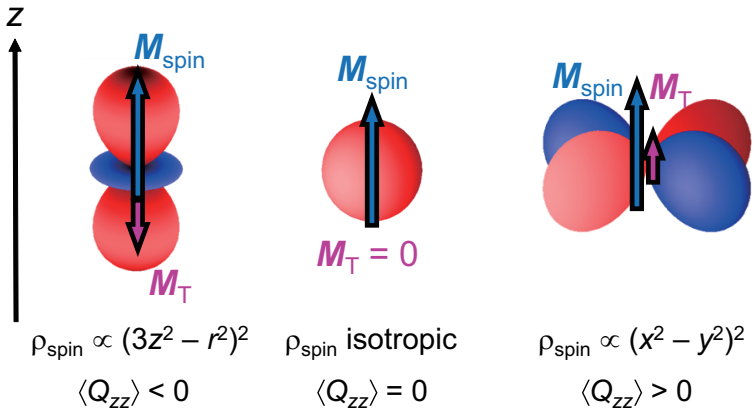

Figure 3.6: Relationship between the magnetic dipole ($\boldsymbol{M}_{\mathrm{T}}$), the spin magnetic moment ($\boldsymbol{M}_{\mathrm{spin}}$), and the anisotropy of the spin density distribution (ρ_{spin}). Figure adapted from the Supplementary Material of Ref. [21].

magnetic metal with uniaxial magnetic anisotropy, the magnetic anisotropy energy (MAE) is proportional to the difference in the orbital magnetic moments (M_{orb}'s) between when the magnetization ($\boldsymbol{M}$) is parallel to the axis (taken to be z-axis hereafter) or perpendicular to it. In the case of less-than-half systems such as manganites, the Bruno's result is expressed as follows:

$$\begin{aligned}\Delta E &= E^x - E^z \\ &= \frac{\zeta}{4\mu_B}\left(|M^z_{\mathrm{orb}}| - |M^x_{\mathrm{orb}}|\right), \end{aligned} \tag{3.10}$$

where ΔE is the MAE, ζ is the strength of SOI of the d electrons, μ_B is the Bohr magneton, and M^z_{orb} (M^x_{orb}) is the orbital magnetic moment along the spin direction when the system is magnetized parallel (perpendicular) to the uniaxial direction (Note that $M_{\mathrm{orb}} < 0$ in the case of less-than-half systems). Owing to its simplicity and intuitiveness, the Bruno equation [Eq. (3.10)] has been widely used to discuss the magnetic anisotropy of many ferromagnetic metallic materials. It should be noted, however, that in Bruno's perturbative calculation, only the 'spin-conserved' terms are taken into account. That is, in the formula of the second-order perturbation theory,

$$E_i^{(2)} = \sum_{|m\rangle \neq |i\rangle} \frac{|\langle m|\hat{H}_{\mathrm{so}}|i\rangle|^2}{E_i - E_m}, \tag{3.11}$$

it is assumed that the spin directions of the initial state $|i\rangle$ and the virtual excited state $|m\rangle$ are the same. Wang *et al.* [58] has later extended the Bruno

equation Eq. (3.10) by considering the 'spin-flip' terms, i.e., the terms where the spin direction in $|m\rangle$ is opposite to that in $|i\rangle$. Their result is summarized by van der Laan in a more concise form [59]. In the case of less-than-half systems, the result can be expressed as follows:

$$\begin{aligned}\Delta E &= E^x - E^z \\ &= \frac{\zeta}{4\mu_B}\left(|M^z_{\mathrm{orb}}| - |M^x_{\mathrm{orb}}|\right) + \frac{21}{4\mu_B}\frac{\zeta^2}{\Delta E_{\mathrm{ex}}}\left(M^z_{\mathrm{T}} - M^x_{\mathrm{T}}\right), \end{aligned} \tag{3.12}$$

where ΔE_{ex} is the exchange splitting between the majority- and minority-spin bands. As explained above, the magnetic dipole M_{T} represents the anisotropy of the spin-density distribution, namely, the shape of the orbitals of the spin-polarized electrons. Equation (3.12) shows that MAE is determined by not only the anisotropy of the orbital magnetic moment but also the magnetic dipole term, namely, the anisotropy of the spin-density distribution.

The theories by Bruno [Eq. (3.10)] and by Wang *et al.* and van der Laan [Eq. (3.12)] have been tested theoretically by using first-principles calculation and experimentally by XMCD. Some studies have shown that Bruno's equation (3.10) at least qualitatively describes the magnetic anisotropy of ferromagnetic thin films, i.e., the orbital magnetic moment M_{orb} has more contribution to magnetic anisotropy than the magnetic dipole M_{T} [60–63], while other studies have shown that Bruno's equation totally collapses in the presence of heavy elements with large spin-orbit interaction, i.e., M_{T} plays more important role than M_{orb}, as proposed by Wang *et al.* [Eq. (3.12)] [64–67]. It is therefore important to separate the contribution from M_{orb} and M_{T} to MAE in order to correctly elucidate the origin of the magnetic anisotropy.

3.3 X-ray magnetic linear dichroism (XMLD)

X-ray linear dichroism (XLD) is an experimental technique analogous to XMCD, in which the x-ray absorption spectra for two different linear polarizations are measured. Since the absorption intensities are determined by the symmetries of the light polarization and the electron orbitals in the initial and final states [Eq. (3.1)], one can deduce information about the orbital character of the valence electrons from the XLD spectra. For example, one can infer whether the in-plane (e.g., d_{xy} or $d_{x^2-y^2}$) or the out-of-plane (e.g., d_{yz}, d_{zx}, or $d_{3z^2-r^2}$) orbitals are more preferentially occupied in thin films by measuring the difference in the XAS spectra between the in-plane and out-of-plane light polarizations [49–51].

It has also been pointed out that, even in the absence of the preferential orbital occupation, XLD arises depending on whether the light polarization is parallel or perpendicular to the local magnetic moment $\boldsymbol{M}$ [68, 69]. This is called x-ray *magnetic* linear dichroism (XMLD), which originates from spin-orbit interaction of core-level electrons. In contrast to XMCD, XMLD can be applicable not only to ferromagnetic but also to antiferromagnetic materials because the spectral intensity of XMLD is proportional to the square of the local moment M^2 [68].

Similarly to XMCD [Eqs. (3.2), (3.3)], sum rules have been derived for X(M)LD [69]. The X(M)LD sum rules can be written as follows:

$$\langle Q_{zz} \rangle = \frac{2\int_{L_3+L_2}(\mu^{\parallel} - \mu^{\perp})\mathrm{d}\nu}{\int_{L_3+L_2}(\mu^{\parallel} + \mu^{\perp})\mathrm{d}\nu}(10 - N_d), \tag{3.13}$$

$$\langle P_{zz} \rangle + \langle R_{zz} \rangle = \frac{5\int_{L_3}(\mu^{\parallel} - \mu^{\perp})\mathrm{d}\nu - 10\int_{L_2}(\mu^{\parallel} - \mu^{\perp})\mathrm{d}\nu}{3\int_{L_3+L_2}(\mu^{\parallel} + \mu^{\perp})\mathrm{d}\nu}(10 - N_d). \tag{3.14}$$

Here, $\mu^{\parallel}$ ($\mu^{\perp}$) is the absorption coefficient when the light polarization is parallel (perpendicular) to the z direction, and P_{zz}, Q_{zz}, and R_{zz} are the operators defined by the following equations:

$$P_{zz} = \frac{1}{2}\sum_n \left(3l_z s_z - \boldsymbol{l}\cdot\boldsymbol{s}\right)_n, \tag{3.15}$$

$$Q_{zz} = \frac{1}{2}\sum_n \left(3l_z^2 - \boldsymbol{l}^2\right)_n, \tag{3.16}$$

$$R_{zz} = \frac{1}{4}\sum_n \left[5l_z(\boldsymbol{l}\cdot\boldsymbol{s})l_z - (\boldsymbol{l}^2 - 2)\boldsymbol{l}\cdot\boldsymbol{s} - (2\boldsymbol{l}^2 + 1)l_z s_z\right]_n, \tag{3.17}$$

with n being the label for each electron [69]. The z-axis is taken parallel to the spin direction in the case of XMLD. Note that Q_{zz} is proportional to the electric quadrupole operator defined by Eq. (3.6') (which can be shown using Wigner-Eckart theorem [70]). Equations (3.13) and (3.14) are the counterparts of the orbital [Eq. (3.2)] and spin sum rules for XMCD [Eq. (3.3)], respectively. These equations show that one can deduce the anisotropic charge distribution (e.g., preferential orbital occupation) induced by the spin $\langle Q_{zz} \rangle$ using Eq. (3.13), and the anisotropy of spin-orbit interaction $\langle P_{zz} \rangle$ using Eq. (3.14), under the assumption that $\langle R_{zz} \rangle$ is small enough compared to $\langle P_{zz} \rangle$.

Figure 3.7 [71] shows an example of studies which utilizes the XLD sum rule. In this study, the interfacial orbital polarization induced in a superlattice composed of $LaNiO_3$ (LNO) and $LaAlO_3$ (LAO) was investigated via XLD and soft x-ray reflectometry. Figure 3.7(a) shows the experimental and calculated XAS spectra at the Ni $L_{2,3}$ ($2p \rightarrow 3d$) absorption edges for the

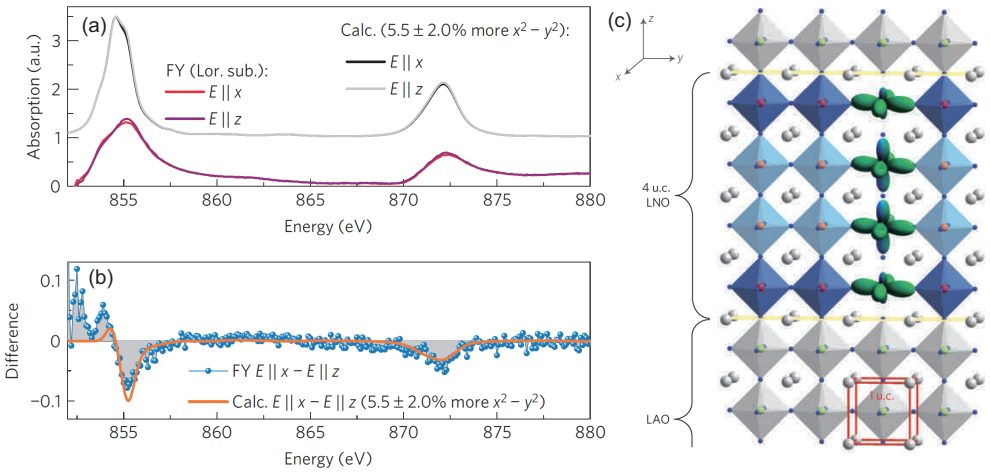

Figure 3.7: X-ray linear dichroism (XLD) on a $[(LaNiO_3)_4/(LaAlO_3)_4]_8$ (LNO/LAO) superlattice. (a) Experimental (colored) and calculated (black/gray) XAS spectra at the Ni $L_{2,3}$ ($2p \rightarrow 3d$) absorption edges for the linear polarizations parallel to the x (in-plane) and z (out-of-plane) directions. Note that the background signals due to the La M_4 ($3d_{3/2} \rightarrow 4f$) absorption edge have been subtracted from the raw spectra (see Ref. [71] for details). (b) Experimental (blue) and calculated (orange) XLD spectra [defined as XAS ($\boldsymbol{E} \parallel x$) − XAS ($\boldsymbol{E} \parallel z$)] corresponding to (a). XLD sum rule shows that the Ni $3d_{x^2-y^2}$ orbital is more preferentially occupied than the Ni $3d_{3z^2-r^2}$ orbital by $\sim 5.5\%$. (c) Schematic illustration of the deduced orbital polarization at the LNO/LAO interfaces. Adapted from Ref. [71].

linear polarizations parallel to the x (in-plane) and z (out-of-plane) directions. The corresponding XLD spectra [=XAS ($\boldsymbol{E} \parallel x$) − XAS ($\boldsymbol{E} \parallel z$), defined opposite to Eq. (3.13)] is shown in Fig. 3.7. The experimental XLD spectrum reasonably agrees with the calculated one. By using the XLD sum rule Eq. (3.13), they have estimated $\langle Q_{zz} \rangle$ and have concluded that the Ni $3d_{x^2-y^2}$ orbital is more preferentially occupied than the Ni $3d_{3z^2-r^2}$ orbital by $\sim 5.5\%$, demonstrating the interfacial orbital reconstruction at the LNO/LAO interfaces [Fig. 3.7(c)].

3.4 Cluster-model calculation

The spectral line shapes of XAS, XMCD, and XMLD for transition-metal oxides can be analyzed using the configuration-interaction (CI) cluster model [72]. In the CI cluster model, one considers a molecule which consists of a transition-metal atom and surrounding anions (see Fig. 2.6), and calculates

the electronic structures of the molecule. For example, an MnO_6 cluster is considered in the case of perovskite-type manganese oxides. Taking the Mn $3d$ and O $2p$ valence orbitals and the Mn $2p$ core orbitals into account, the Hamiltonian of the cluster is expressed as follows [72]:

$$\hat{H} = \hat{H}_1 + \hat{H}_2, \tag{3.18}$$

$$\begin{aligned}\hat{H}_1 = \sum_i \epsilon_d(\Gamma_i) \sum_{\gamma_i} d^\dagger_{\gamma_i} d_{\gamma_i} + \sum_i \epsilon_p(\Gamma_i) \sum_{\gamma_i} p^\dagger_{\gamma_i} p_{\gamma_i} + \epsilon_c \sum_\xi c^\dagger_\xi c_\xi \\ + U_{dd} \sum_{i,j} \sum_{\gamma_i \neq \gamma_j} n_{d\gamma_i} n_{d\gamma_j} - U_{dc} \sum_{i,\gamma_i} n_{d\gamma_i} \sum_\xi (1 - n_{c\xi}) \\ + \sum_i V(\Gamma_i) \sum_{\gamma_i} (d^\dagger_{\gamma_i} p_{\gamma_i} + h.c.),\end{aligned} \tag{3.19}$$

$$\hat{H}_2 = H_{dd} + H_{dc} + H_d(\zeta_d) + H_c(\zeta_c). \tag{3.20}$$

$\hat{H}_1$ and $\hat{H}_2$ are, respectively, the non-multiplet and multiplet terms describing the valence and core states and electron-electron interaction between these states. In Eq. (3.19), Γ_i is a representation of the symmetry group (such as e_g and t_{2g} representations in the O_h symmetry), γ_i is the basis of each representation including spin states (such as $d_{xy\uparrow}$ or $d_{3z^2-r^2\downarrow}$ etc.), ϵ_d, ϵ_p, and ϵ_c are, respectively, the energies of the one-electron orbitals of the Mn $3d$, O $2p$ (valence) and the Mn $2p$ (core) levels, $d^\dagger_{\gamma_i}$, $p^\dagger_{\gamma_i}$, and $c^\dagger_\xi$ (d_{γ_i}, p_{γ_i}, and c_ξ) are the creation (annihilation) operators for these levels, $n_{d\gamma_i}$ and $n_{c\xi}$ are the number operators, U_{dd} (U_{dc}) is the Coulomb energy between the Mn $3d$ and Mn $3d$ (Mn $3d$ and Mn $2p$) electrons, and V is the hybridization between the Mn $3d$ and O $2p$ orbitals. In Eq. (3.20), H_{dd} and H_{dc} are the full-multiplet interaction between the Mn $3d$ and Mn $3d$ (Mn $3d$ and Mn $2p$) levels, respectively, and $H_d(\zeta_d)$ and $H_c(\zeta_c)$ are spin-orbit interaction (SOI). H_{dd} and H_{dc} can be expressed using the Slater integrals F^i's and G^i's [73], which represent the anisotropy of Coulomb interaction. Note that, in the case of O_h symmetry, the hybridization strength V can be expressed using Slater-Koster parameters $(pd\sigma)$ and $(pd\sigma)$ as follows [74]:

$$V(t_{2g}) = 2(pd\pi) \tag{3.21}$$

$$V(e_g) = -\sqrt{3}(pd\sigma) \tag{3.22}$$

In the CI cluster model, one assumes that the initial and final electronic states can be expressed as superpositions of several different electron configurations in order to take into account the effect of electron transfer from

the O $2p$ to Mn $3d$ orbitals. That is, one assumes that the wavefunctions of the initial ($|i\rangle$) and final states ($|f\rangle$) can be written as follows [72]:

$$|i\rangle = \alpha_0|3d^n 2p^6\rangle + \alpha_1|3d^{n+1}2p^6\underline{L}\rangle + \alpha_2|3d^{n+2}2p^6\underline{L}^2\rangle + \cdots , \tag{3.23}$$

$$|f\rangle = \beta_0|3d^{n+1}2p^5\rangle + \beta_1|3d^{n+2}2p^5\underline{L}\rangle + \beta_2|3d^{n+3}2p^5\underline{L}^2\rangle + \cdots . \tag{3.24}$$

Here, $3d$ (valence) and $2p$ (core) denote the corresponding orbitals of Mn, $\underline{L}$ denotes the hole in the ligand O $2p$ orbitals, and n is the nominal number of electrons in the Mn $3d$ orbitals. In addition, the charge-transfer energy Δ is defined by

$$\Delta = E(|3d^{n+1}2p^6\underline{L}\rangle) - E(|3d^n 2p^6\rangle), \tag{3.25}$$

where $E(|3d^{n+1}2p^6\underline{L}\rangle)$ and $E(|3d^n 2p^6\rangle)$ are the average energies of these configurations. By diagonalizing the Hamiltonian in Eq. (3.18) using the wavefunctions in Eqs. (3.23) and (3.24), the energy levels and transition probabilities between these levels can be calculated and thus the x-ray absorption intensities are obtained. The Coulomb energies U_{dd} and U_{dc}, the hybridization energy V, the charge-transfer energy Δ, and the crystal-field splitting $10Dq$ and $8Cp$ [see Fig. 2.6 for definition], are usually taken as adjustable parameters to fit the simulated spectra to the experimental ones.

Chapter 4

Experimental methods and analyses

In the present chapter, technical details and analysis methods of angle-dependent XMCD is explained.

4.1 Vector-magnet apparatus for XMCD and XMLD

The present section describes the details of the vector-magnet apparatus, which is used for the angle-dependent x-ray magnetic circular dichroism (XMCD) and x-ray magnetic linear dichroism (XMLD) experiments in the following chapters.

The conceptual design of the vector magnet is schematically described in Fig. 4.1. The vector magnet is composed of two pairs of superconducting coils which are orthogonally arranged along the horizontal and vertical directions. One can apply magnetic field along an arbitrary direction within the plane formed by the axes of the two coil pairs by adjusting the magnitudes of the electric currents which flow through the two pairs of superconducting coils independently using two bipolar current sources (Fig. 4.2). The horizontal coils are aligned parallel to the incident x rays, namely, the magnetic field is applied parallel to the x rays when the vertical coils are turned off. One can also change the incident angle of the x rays by rotating the sample holder using the manipulator. This means that the directions of the applied magnetic field and the incident x rays can be controlled independently.

Each superconducting coil is stored in a cone-shaped copper casing unit, in which seven pancake-like coils with different outer diameters ranging from 60-104 mm are stacked, as shown in Fig. 4.3 [4, 75]. Such a design of coils

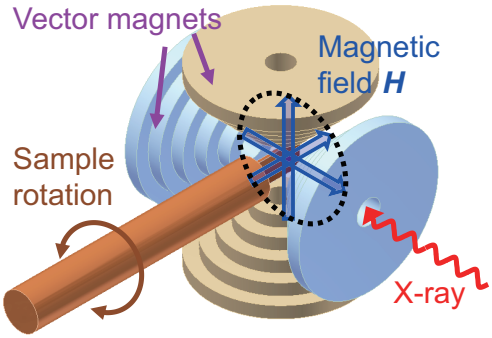

Figure 4.1: Conceptual description of the vector-magnet apparatus. Adapted from Ref. [21].

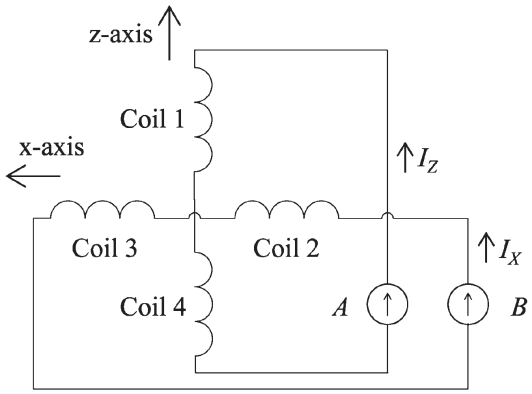

Figure 4.2: Schematic description of the electric circuit of the superconducting coils. Here, A and B represents bipolar current sources which supply the two pairs of superconducting coils with electric currents. Reproduced from Ref. [4].

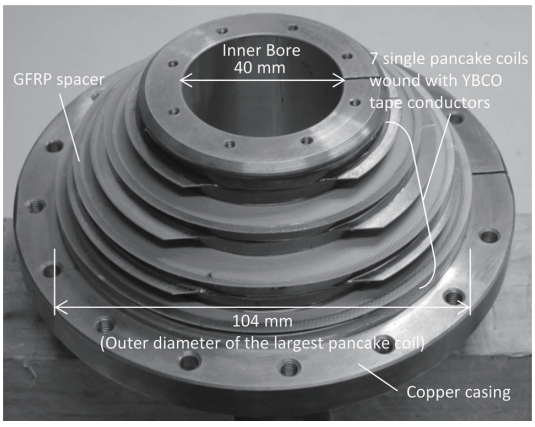

Figure 4.3: Picture of the a cone-shaped copper casing unit for the superconducting coils. Reproduced from Ref. [4].

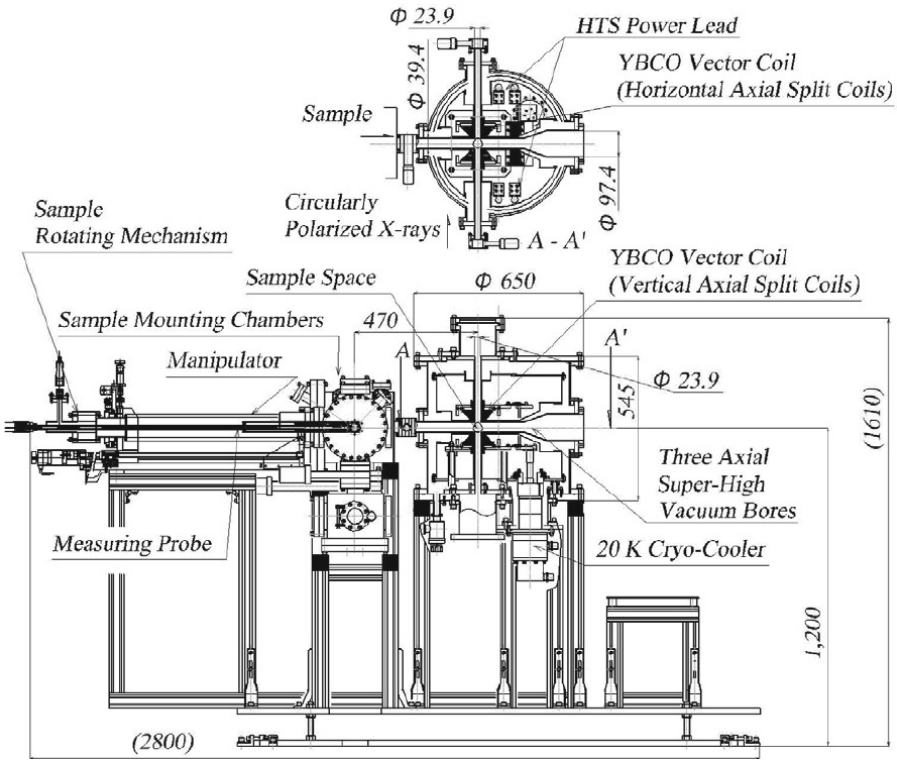

Figure 4.4: Schematic drawing of the entire system of the vector-magnet XMCD apparatus. The top and bottom panels represents the vertical and horizontal cross-sectional views, respectively. Reproduced from Ref. [75].

has been adopted so that the coils come close to each other and thus the strength of the magnetic field at the center is maximized. The superconducting coils are made of the $YBa_2Cu_3O_{7-\delta}$ (YBCO) sheet wire with width of 4 mm and thickness of 0.1 mm (manufactured by SuperPower Inc.) [4,75]. The use of the YBCO wire allows us to operate the magnets at high temperatures up to 30 K [4,75]. These superconducting coils are cooled using a vapor-compression refrigerator down to < 20 K. The inner diameter of the pancake coils is 45 mm and the total turn number is 1004 [4]. The designed operation current is 140 A for each pair of the superconducting coils [75], which corresponds to 1 T at the center of the vector magnet.

Figure 4.4 schematically describes the general view of the vector-magnet XMCD apparatus. The sample is transferred from the left-hand side of the figure into the measurement chamber drawn at the center of the figure. During the measurements, the sample is located at the center of the three axial vacuum bores, which is pumped by turbo molecular pumps and ion pumps down to $< 1\times10^{-9}$ Torr. The superconducting coil units are installed so that they surrounds the three axial vacuum bores, as shown in Fig. 4.4. Note that

Table 4.1: Specification of the vector-magnet XMCD apparatus in the present study compared with those constructed in Advanced Light Source (ALS) [76] and National Synchrotron Radiation Research Center (NSRRC) [77].

	Present work [4, 75]	ALS [76]	NSRRC [77]
Number of pole pieces	4	8	8
Field direction	2D	3D	3D
Maximum magnetic field (T)	1.0	0.9	3.65
Magnet	YBCO magnet	Electromagnet	$Bi_2Sr_2Ca_2Cu_3O_{10}$ magnet
Magnet cooling method	Cryocooler	Water flow	Cryocooler and liquid N_2
Sample Space (mm)	23.9× 24.8 × 39.4	20.3 diameter	25.4 diameter
Sample temperature (K)	20-300	15-450	N/A
Available measurements	XAS/XMCD /XMLD	XAS/XMCD /XMLD	Resonant x-ray scattering

the spaces where the sample and the superconducting coils are located are separated. The space for the superconducting coils (inside the large cylindrical chamber in Fig. 4.4) is pumped by a turbo molecular pump down to $\sim 10^{-5}$ Torr for the heat-insulation purpose. The front- and back-side ports of the three axial vacuum bores are connected to the beamline. The top and bottom ports are used for installing sample-supporting rods, which is necessary in order to reduce mechanical vibration of the sample holder. The port at the right-hand side is used for monitoring the manipulator position during the sample transfer. In the present system, the sample can be cooled using a liquid-helium gas-flow cryostat down to the lowest temperature of ~ 20 K.

Table 4.1 summarizes the specification of the vector-magnet XMCD apparatus in the present study compared with those constructed in other synchrotron facilities (Advanced Light Source (ALS) [76] in the U.S.A. and National Synchrotron Radiation Research Center (NSRRC) in Taiwan [77]).

In these facilities, octapole vector-magnet systems, in which the eight pole pieces are placed along the diagonal directions around the sample, have been adopted [76, 77]. Although the direction of the magnetic field is limited to two dimensions in our apparatus, larger sample space and magnetic field strength comparable to ALS are achieved at the same time by the use of the high-temperature superconducting magnet (made of YBCO) and the simpler mechanical structure. In addition, no cryogen such as liquid nitrogen or liquid helium is required for the operation of the YBCO superconducting magnet.

4.2 Beamlines

The XMCD and XMLD experiments in this thesis have been performed at beamlines BL-16A2 of Photon Factory (PF) in High Energy Accelerator Research Organization (KEK) and BL23SU of SPring-8. In addition to the vector-XMCD apparatus installed at KEK-PF, several XMCD apparatuses have been used. In this section, details about these synchrotron beamlines and apparatuses are described.

4.2.1 Photon Factory BL-16A

The beamline BL-16A at KEK-PF [78, 79] is designed for soft x-ray spectroscopy including XAS, XMCD, photoemission spectroscopy (PES), and resonant x-ray scattering. It is equipped with a twin APPLE-II type undulator, which covers the photon energy range of 180-1500 eV and provides soft x rays with linear, circular, and eliptical polarizations. Table 4.2 summarizes the available photon energy for each polarization mode. The photon flux is $\sim 1 \times 10^{11}$ photons/sec at the energy resolution of $E/\Delta E = 8000$. A fast polarization-switching mode is available by using the two undulators installed in a tandem configuration [80, 81]. The principle of the fast polarization switching is shown in Fig. 4.5 [80]. For dichroism measurements, the two undulators are set to different polarization modes (e.g., the ID1 undulator to the right-handed circular polarization and the ID2 undulator to the left-handed circular polarization). By manipulating the trajectory of electrons using 'kicker magnets', one can extract the light from only one of the undulators, as shown in Fig. 4.5.

A schematic layout of the beamline optics is shown in Fig. 4.6 [78, 82]. Synchrotron light generated from the undulators is vertically converged onto the entrance slit S1 by the pre-focusing toroidal mirror M0. Since S1 can be regarded as a virtual point light source, these pre-focusing optics enable one to suppress the variation of the light-emitting point due to the instability

Table 4.2: Photon energies ($h\nu$'s) available at KEK-PF beamline BL-16A for each polarization mode [79].

Polarization	$h\nu$ (eV)
Circular	297-1000
Linear (horizontal)	180-1500
Linear (vertical)	380-1500
Eliptical	218-1500

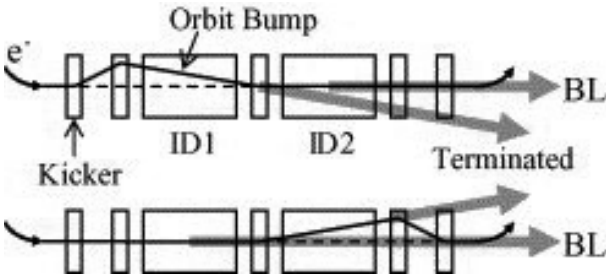

Figure 4.5: Principle of fast polarization switching using the twin undulators. Reproduced from [80].

of the synchrotron light source. The light which has gone through S1 is vertically converged by the cylindrical mirror M1 and then is irradiated on the monochrometer which consists of a plane mirror M2 and a planar varied-line-spacing grating (VLSG). The VLSG is a diffraction grating which has different line spacings depending on the position in order to achieve high resolution in a wide photon-energy range [82–84]. The monochromated light passes through the exit slit S2. The plane mirror Mp is used to direct the beam into one of the two beamline branches (BL-16A1 and BL-16A2). Finally, the monochromated light is converged using the toroidal mirrors M3 or M3' onto the focal points F1, F2, or F3, where the endstation instruments are installed.

In addition to the vector-XMCD apparatus described in Sec. 4.1, an XMCD apparatus equipped with a superconducting magnet [85] installed at KEK-PF BL-16A has been used in the present studies. Figure 4.7 [85] is the schematic description of the apparatus. The apparatus consists of an measurement chamber where the sample and the x rays are introduced, a liquid-helium bath in which the superconducting magnet coil is installed, and a liquid-nitrogen bath as a thermal shield. The superconducting magnet coil is made of a NbTi wire and can produce magnetic fields parallel to the incident x rays up to $|H| = 5$ T. Samples are cooled by a He-gas-flow cryostat. The attainable lowest sample temperature is $\sim$ 10 K. Angle θ

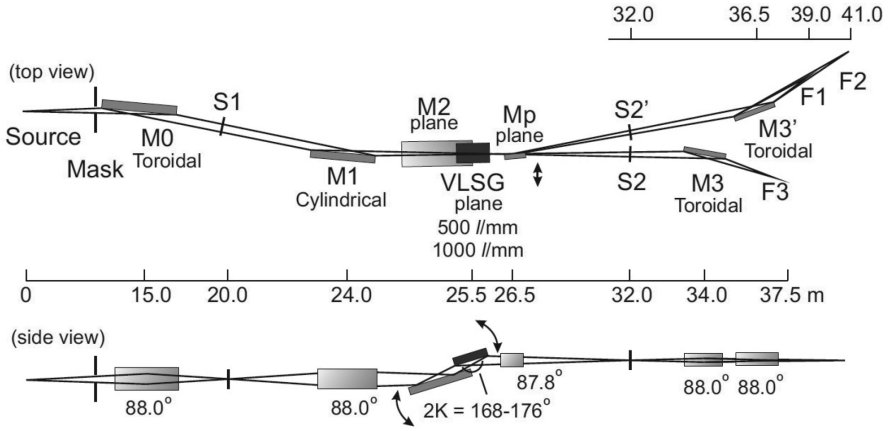

Figure 4.6: Beamline optics of KEK-PF BL-16A. Reproduced from [78].

between the sample normal and the incident x rays can be varied in the range of $0^\circ \leq |\theta| \lesssim 70^\circ$. Both the TEY and TFY measurement modes are available.

The vector-magnet XMCD apparatus and the superconducting-magnet XMCD apparatus are installed at the focal points F1 and F2 in Fig. 4.6, respectively.

4.2.2 SPring-8 BL23SU

BL23SU at SPring-8 [84, 86] is a beamline designed for soft-x-ray spectroscopies on various materials, including surface chemistry, actinide compounds, biological materials, and magnetic materials. It is equipped with a twin-helical undulator and covers the photon energies ranging from 370 eV to several keV in the circular polarization mode [86]. The energy resolution $E/\Delta E$ is better than 10000. The photon flux at the sample position is $\sim 1 \times 10^{12}$ photons $\cdot \sec^{-1} \cdot (0.01\%$ bandwidth$)^{-1}$ for $h\nu = 700$ eV [86]. The polarization of x rays can be switched at 1 Hz using the two helical undulators (Fig. 4.5), which enables us high-precision measurements [80, 87].

The beamline optics of BL23SU is schematically shown in Fig. 4.8 [86]. Synchrotron light generated from the twin-helical undulator (THU) passes through the pre-focusing optics, which consist of a vertical condensing mirror M_v, a horizontal collimating mirror M_h, and the entrance slit. Light is then focused onto the planar VLSG (VLSPG) using a spherical mirror (either M_1 or M_2).The monochromated light is then vertically collimated by the cylindrical mirror M_3 and converged by the toroidal mirror M_4 onto one of the focal positions where the endstation instruments are installed.

Figure 4.9 is a schematic description of the experimental geometry of

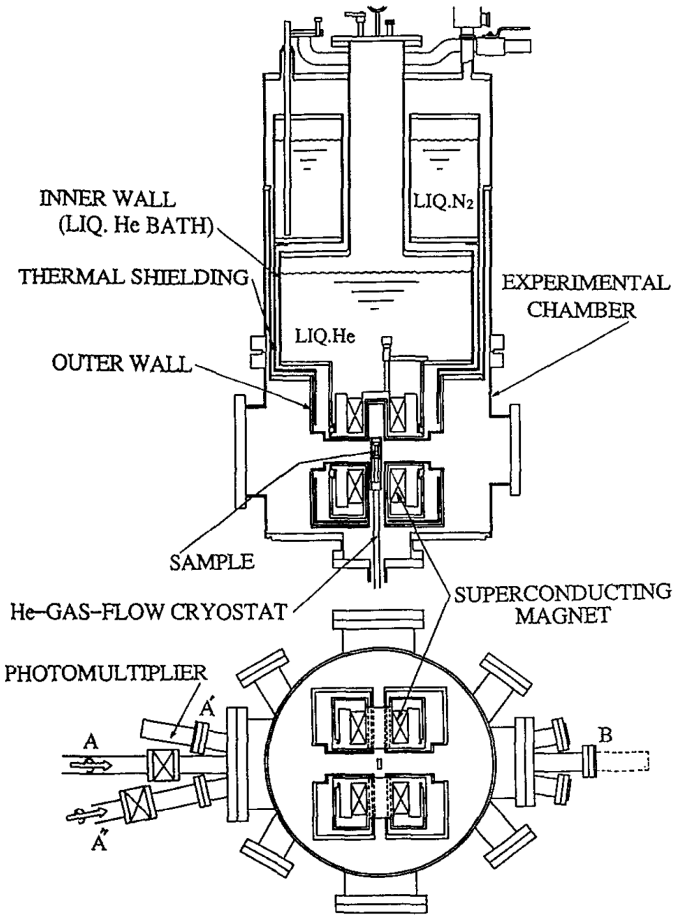

Figure 4.7: Superconducting-magnet XMCD apparatus at beamline BL-16A of Photon Factory. Reproduced from [85].

XMCD at BL23SU. The chamber is equipped with a superconducting magnet which can generate a magnetic field up to 10 T parallel to the x rays. The sample can be cooled down to $\sim$ 10 K using a He-gas-flow cryostat. Since the sample manipulator is attached to the downstream side of the beamline, the incident angle of the x rays is fixed at 0° (normal incidence). The absorption signal is measured in the TEY mode.

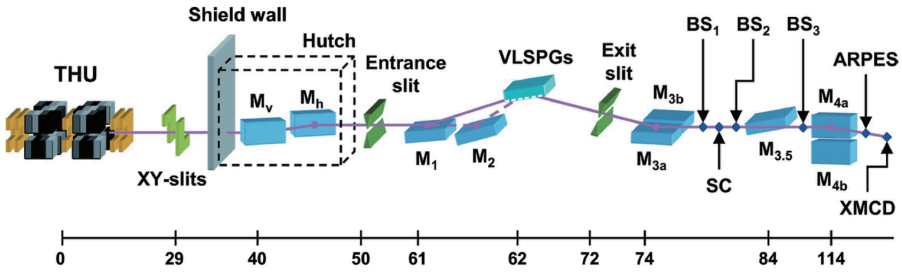

Figure 4.8: Beamline optics of SPring-8 beamline BL23SU. Reproduced from [86].

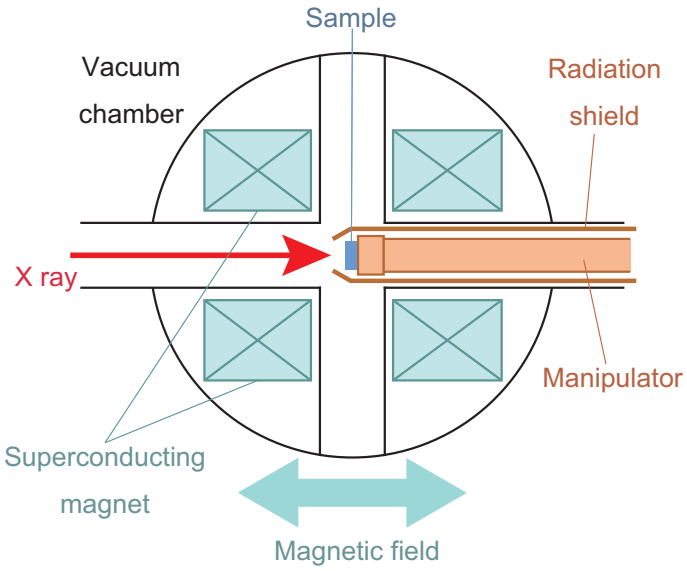

Figure 4.9: Schematic drawing of the XMCD measurement chamber at SPring-8 beamline BL23SU.

4.3 Experimental and Analysis methods of angle-dependent XMCD

4.3.1 Angle-dependent XMCD and transverse XMCD

As explained in Sec. 3.2.3, the magnetic dipole term $\hat{\boldsymbol{P}} \cdot \boldsymbol{M}_{\mathrm{T}}$ in Eq. (3.3) represents the orbital occupation of the spin-polarized electrons, which may be a key to elucidate the magnetic anisotropy of ferromagnetic materials from microscopic point of view. It has been theoretically proposed that this term can be extracted from the angle-dependent XMCD experiments because the $\hat{\boldsymbol{P}} \cdot \boldsymbol{M}_{\mathrm{T}}$ and $\hat{\boldsymbol{P}} \cdot \boldsymbol{M}_{\mathrm{spin}}$ terms in Eq. (3.3) show different angular dependencies with respect to the directions of the magnetization ($\theta_{\boldsymbol{M}}$) or the incident x rays (θ_{inc}) [3]. Such an experiment can be performed by using the vector-type magnet apparatus described in Sec. 4.1. The experimental geometry for the angle-dependent XMCD is described in Fig. 4.10(a). All the angles ($\theta_{\boldsymbol{M}}$, θ_{inc}, and the magnetic-field direction $\theta_{\boldsymbol{H}}$) are defined with respect to the sample normal. The left-hand side of the spin sum rule [Eq. (3.3)] can then be rewritten using Eq. (3.9) as follows:

$$
\begin{aligned}
& \hat{\boldsymbol{P}} \cdot \boldsymbol{M}_{\mathrm{spin}} + (7/2)\hat{\boldsymbol{P}} \cdot \boldsymbol{M}_{\mathrm{T}} \\
\simeq\ & \sum_i \hat{P}_i M^i_{\mathrm{spin}} + (7/2) \sum_i \hat{P}_i \langle Q_{ii} \rangle M^i_{\mathrm{spin}} \\
=\ & M_{\mathrm{spin}} \cos(\theta_{\boldsymbol{M}} - \theta_{\mathrm{inc}}) \\
& + (7/4)\langle Q_{zz} \rangle M_{\mathrm{spin}} (2 \cos\theta_{\boldsymbol{M}} \cos\theta_{\mathrm{inc}} - \sin\theta_{\boldsymbol{M}} \sin\theta_{\mathrm{inc}}). \qquad (4.1)
\end{aligned}
$$

Here the four-fold in-plane rotational symmetry $\langle Q_{xx} \rangle = \langle Q_{yy} \rangle$ has been assumed (as in thin films) and the traceless property of $\boldsymbol{Q}$ (i.e., $2\langle Q_{xx} \rangle + \langle Q_{zz} \rangle = 0$) has been used. From this equation, the $\theta_{\boldsymbol{M}}$-dependencies of the spin magnetic moment $\hat{\boldsymbol{P}} \cdot \boldsymbol{M}_{\mathrm{spin}}$, the magnetic dipole term $(7/2)\hat{\boldsymbol{P}} \cdot \boldsymbol{M}_{\mathrm{T}}$, and the sum of them ($\hat{\boldsymbol{P}} \cdot \boldsymbol{M}^{\mathrm{eff}}_{\mathrm{spin}}$) can be calculated as shown in Fig. 4.10(b) (here, the x-ray incident angle θ_{inc} is fixed to 45°). Since the angular dependence of $\hat{\boldsymbol{P}} \cdot \boldsymbol{M}_{\mathrm{spin}}$ and $(7/2)\hat{\boldsymbol{P}} \cdot \boldsymbol{M}_{\mathrm{T}}$ are different, one can deduce the sign and the magnitude of $\langle Q_{zz} \rangle > 0$ of the spin-polarized electrons from the angular dependence of $\hat{\boldsymbol{P}} \cdot \boldsymbol{M}^{\mathrm{eff}}_{\mathrm{spin}}$ which can be measured by XMCD.

Especially, if the spin magnetic moment $\boldsymbol{M}_{\mathrm{spin}}$ is aligned perpendicular to the incident x rays ($\theta_{\mathrm{inc}} = 45°$), the $\hat{\boldsymbol{P}} \cdot \boldsymbol{M}_{\mathrm{spin}}$ term vanishes and thus only the magnetic dipole term $\hat{\boldsymbol{P}} \cdot \boldsymbol{M}_{\mathrm{T}}$ remains (Fig. 4.11). This geometry is called transverse XMCD (TXMCD), which has been theoretically proposed to directly detect the XMCD signals originating from $\boldsymbol{M}_{\mathrm{T}}$ [3]. Since the magnetization angle $\theta_{\boldsymbol{M}}$ and the magnetic-field angle $\theta_{\boldsymbol{H}}$ are in general different in actual experiments, one has to search for the angle where the TXMCD geometry is realized by gradually changing $\theta_{\boldsymbol{H}}$.

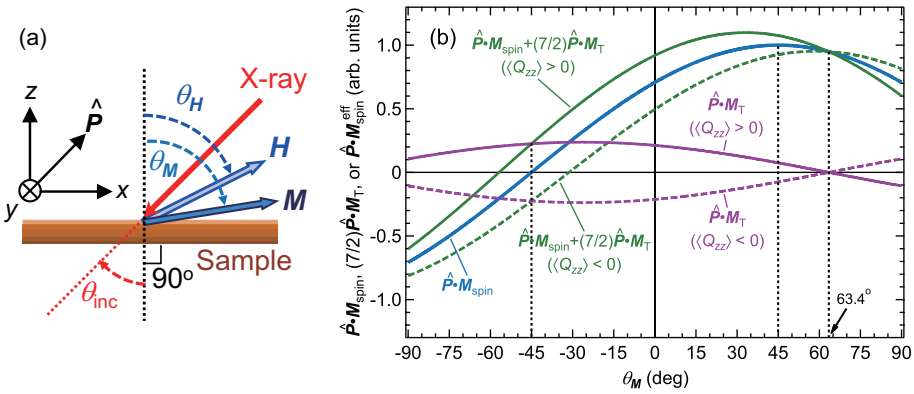

Figure 4.10: Angle-dependent XMCD. (a) Experimental geometry of angle-dependent XMCD and the definition of the directions of incident x rays ($\theta_{\rm inc}$), magnetic field ($\theta_{\boldsymbol{H}}$), and magnetization ($\theta_{\boldsymbol{M}}$). $\hat{\boldsymbol{P}}$ is a unit vector along the x-ray incident direction, which is defined to be antiparallel to the wavevector $\boldsymbol{k}$ of x rays. (b) Theoretical angular dependences of $\hat{\boldsymbol{P}}\cdot\boldsymbol{M}_{\rm spin}$, $(7/2)\hat{\boldsymbol{P}}\cdot\boldsymbol{M}_{\rm T}$, and $\hat{\boldsymbol{P}}\cdot\boldsymbol{M}_{\rm spin}^{\rm eff}$ in Eq. (3.3), for the x-ray incident angle ($\theta_{\rm inc}$) of 45°. The solid and dashed curves, respectively, describe the cases where the zz-component of the electric quadrupole moment tensor ($\langle Q_{zz}\rangle$) is positive and negative, i.e. the electron orbital is $d_{x^2-y^2}$-like and $d_{3z^2-r^2}$-like. The magnitudes of $\boldsymbol{M}_{\rm spin}$ and $\langle Q_{zz}\rangle$ are assumed to be $M_{\rm spin}=1$ and $(7/2)\langle Q_{zz}\rangle = 0.3$. Panel (a) adapted from Ref. [21] and Panel (b) from the Supplementary Material of it.

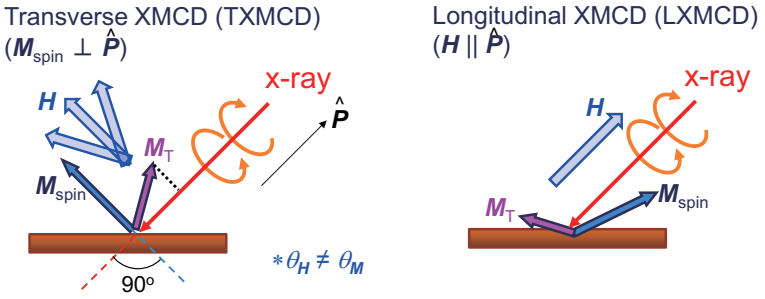

Figure 4.11: Geometries for transverse XMCD (TXMCD, left) and the conventional (longitudinal) XMCD (right).

4.3.2 Estimation of the magnetic anisotropy energy from angle-dependent XMCD

Angle-dependent XMCD can also be used to deduce the magnetic anisotropy energy (MAE) of the sample, as described below. In the presence of magnetic anisotropy, the spin magnetization $\boldsymbol{M}$ are in general not entirely aligned parallel to the external magnetic field $\boldsymbol{H}$. In order to deduce the magnetization direction $\theta_{\boldsymbol{M}}$ from the field direction $\theta_{\boldsymbol{H}}$, Stoner-Wohlfarth model [88] has been used as a simple model which incorporates the effect of magnetic anisotropy in ferromagnetic materials. In this model, one assumes that the sample has only a single magnetic domain and that the magnetic anisotropy is uniaxial (i.e., it has only a single magnetic easy/hard axis). The MAE per volume E to the lowest order is then written as follows:

$$\begin{aligned} E = & - \mu_0 M_{\mathrm{sat}} H \cos(\theta_{\boldsymbol{M}} - \theta_{\boldsymbol{H}}) \\ & + \frac{\mu_0}{2} M_{\mathrm{sat}}^2 \cos^2\theta_{\boldsymbol{M}} - K_{\mathrm{u}} \cos^2\theta_{\boldsymbol{M}}, \end{aligned} \tag{4.2}$$

where M_{sat} is the saturation magnetization and K_{u} is the uniaxial MAE ($K_u > 0$ for out-of-plane easy axis). The three terms in Eq. (4.2) represent the Zeeman energy due to the external magnetic field $\boldsymbol{H}$, the shape magnetic anisotropy due to the demagnetization field in the film, and the magnetocrystalline anisotropy (MCA) which originates from spin-orbit interaction. The magnetization direction $\theta_{\boldsymbol{M}}$ for certain $\theta_{\boldsymbol{H}}$, H, K_{u}, and M_{sat} is determinded so that E is minimized with respect to $\theta_{\boldsymbol{M}}$. The $\theta_{\boldsymbol{H}}$-dependence of $\hat{\boldsymbol{P}} \cdot \boldsymbol{M}_{\mathrm{spin}}^{\mathrm{eff}} \equiv \hat{\boldsymbol{P}} \cdot [\boldsymbol{M}_{\mathrm{spin}} + (7/2)\boldsymbol{M}_{\mathrm{T}}]$ can then be calculated from Eq. (4.1) using this $\theta_{\boldsymbol{M}}$. By fitting the obtained angular dependence of $\hat{\boldsymbol{P}} \cdot \boldsymbol{M}_{\mathrm{spin}}^{\mathrm{eff}}$ to the experimental one, one can deduce the parameters K_u, M_{sat}, and $\langle Q_{zz} \rangle$ using the least-square method.

Chapter 5

Thickness-dependent magnetic properties of $La_{0.6}Sr_{0.4}MnO_3$ thin films studied by x-ray magnetic circular dichroism

Part of this chapter has been published in "Thickness-dependent ferromagnetic metal to paramagnetic insulator transition in $La_{0.6}Sr_{0.4}MnO_3$ thin films studied by x-ray magnetic circular dichroism", G. Shibata, K. Yoshimatsu, E. Sakai, V. R. Singh, V. K. Verma, K. Ishigami, T. Harano, T. Kadono, Y. Takeda, T. Okane, Y. Saitoh, H. Yamagami, A. Sawa, H. Kumigashira, M. Oshima, T. Koide, and A. Fujimori, Phys. Rev. B **89**, 235123 (2014).

5.1 Introduction

Perovskite-type $3d$ transition-metal oxides (TMOs) have been extensively studied because of their wide variety of intriguing physical properties, which can be controlled by changing the bandwidth or the filling of the hybridized transition-metal $3d$ and O $2p$ bands [9]. Especially, it has recently become possible to epitaxially grow single-crystalline thin films of $3d$ TMOs, controlling their stacking on the atomic scale. The physical properties of those TMO thin films are not only governed by their bandwidth and electron filling, but also by their thickness, i.e., dimensionality. Metallic oxide thin films, such as $La_{1-x}Sr_xMnO_3$ (LSMO) [34–36, 89], $SrRuO_3$ (SRO) [37, 38], $SrVO_3$ (SVO) [31, 39], and $LaNiO_3$ [32], ubiquitously undergo metal-to-insulator transitions (MITs) when the film thickness is reduced down to a critical thickness of several unit cells (UC). In ferromagnetic metals such as LSMO [35, 36] and SRO [37], a concomitant suppression of the fer-

romagnetism has been also observed. Such MITs are observed by both transport [32, 34, 35, 37] and photoemission spectroscopy (PES) measurements [31, 36, 38, 39]. The PES studies show that an energy gap of order $\sim$ 1 eV opens at the Fermi energy (E_F) below the critical thicknesses of 4 UC (SRO [38], SVO [31]) to 8 UC (LSMO [36]). Although conventional metallic thin films also undergo thickness-dependent MITs driven by surface roughness and disorders [40–44, 90], the existence of such a large energy gap in TMO thin films implies that one also has to take into account the strong electron correlation. However, the detailed mechanism for these thickness-dependent MIT in TMOs have not been understood yet. One possible mechanism, which has been proposed to explain the MIT of SVO thin films [31], is the dimensionality-induced reduction of the bandwidth due to the decreased number of nearest neighbors. For LSMO thin films, however, this simple picture is insufficient to explain the MIT, because the electron filling of the Mn 3d band is not an integer. Other possible mechanisms include localization of charge carriers due to disorder or lattice distortion, and the relative increase of interfacial effects such as charge transfer and electronic reconstruction. Because all these mechanisms accompany the changes in the electronic structure and spin states of transition-metal ions, microscopic probe for them are strongly desired in order to elucidate the origin of the thickness-dependent MIT and magnetic phase transition in TMO thin films.

In this chapter, x-ray absorption spectroscopy (XAS) and x-ray magnetic circular dichroism (XMCD) studies on the electronic structure and magnetic properties of LSMO ($x = 0.4$) thin films with varying film thickness shall be presented. The element selectivity of XMCD allows us to probe the intrinsic magnetism of the LSMO thin films quantitatively, without extrinsic contribution such as diamagnetism from the substrates. The valence state of the Mn atoms can also be inferred from the spectral line shapes of the XAS spectra. The results show that the suppression of the ferromagnetism with decreasing thickness occurs more gradually than the MIT, suggesting a percolative nature of the phase transition. It has been also shown that the valence of Mn approaches 3+ below the critical thickness of the MIT, possibly due to interfacial charge transfer and/or off-stoichiometry in thinner films.

5.2 Experimetal

Figure 5.1 schematically describes the stacking structure of the studied LSMO ($x = 0.4$) thin films. The films were grown on the TiO_2-terminated $SrTiO_3$ (001) (STO) substrates by laser molecular beam epitaxy [91], with

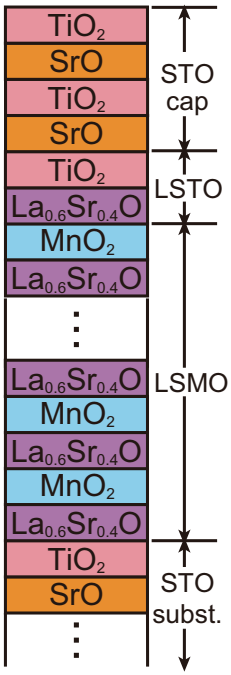

Figure 5.1: Schematic drawing of the stacking structure of the studied $La_{0.6}Sr_{0.4}MnO_3$ (LSMO) thin films.

thicknesses ranging from 2 to 15 UC. The deposited LSMO films were capped by $La_{0.6}Sr_{0.4}TiO_3$ (LSTO) and subsequently-deposited STO with thicknesses of 2 UC and 1 UC, respectively. The role of the LSTO layer is to keep the local environment of the top MnO_2 layer similar to that in the bulk, i.e., every MnO_2 layer is sandwiched by $La_{0.6}Sr_{0.4}O$ (LSO) layers, as shown in Fig. 5.1 [36]. The intensity oscillation of the specular spot in reflection high-energy electron diffraction (RHEED) was used as an indicator for the film thickness during the growth. The surface morphology of the deposited films was examined by atomic force microscopy, and all the films exhibited step-and-terrace structures, confirming that atomically flat surfaces were obtained. It was also confirmed that the films were coherently grown by four-circle x-ray diffraction measurements. In order to reduce oxygen vacancies, the films were annealed in an oxidizing atmosphere for 45 minutes at a temperature of 400 °C and at an oxygen pressure of 1 bar before the XMCD measurements. The XMCD measurements were performed at BL-16A of KEK-PF and at BL23SU of SPring-8 [86]. The spectra were measured in the normal incident geometry, namely, both the incident x rays and the applied magnetic field were perpendicular to the sample surface. The measurement temperature T was equal to 20 K. All the data were collected in the total electron yield mode.

The spin magnetic moment $M_{\rm spin}$ was deduced by applying the XMCD spin sum rule [55] to the obtained XMCD spectra. The orbital magnetic moment $M_{\rm orb}$ and the magnetic dipole $M_{\rm T}$ were neglected in the present study because both quantities are more than one order of magnitude smaller than $M_{\rm spin}$. This can produce systematic errors of $\lesssim 10\%$ in $M_{\rm spin}$. The procedure for applying the spin sum rule to the experimental spectra was essentially the same as that described in Ref. [92]: The hole number of the Mn $3d$ band (n_d) was assumed to be 5.78 by considering the charge transfer between the Mn $3d$ and the ligand O $2p$ bands [92]. In addition, the deduced $M_{\rm spin}$ has been devided by the 'correction factor' (= 0.587) given in Ref. [93], since $M_{\rm spin}$ deduced from the spin sum rule tends to be smaller than the actual value for less-than-half-filled systems due to the small spin-orbit splitting between the $2p_{3/2}$ and $2p_{1/2}$ core levels [93, 94].

5.3 Results and discussion

Figures 5.2(a) and 5.2(b) show the Mn $L_{2,3}$-edge XAS and XMCD spectra of the LSMO samples with various thicknesses, respectively. The spectra have been normalized so that the peak height of XAS at the Mn L_3 edge is equal to unity. The spectral line shapes of XAS and XMCD are similar to those observed in the previous study of bulk LSMO (x = 0-0.5) [92], reflecting the mixed valence state between Mn^{3+} and Mn^{4+}. The XMCD intensity gradually decreases with the reduction of the thickness, consistent with the thickness-dependent MIT and magnetic phase transition reported in previous studies [34–36].

Thickness dependence of the magnetic properties of LSMO thin films has been investigated by analyzing the magnetization curves obtained by the XMCD measurements. Figures 5.3(a) shows the magnetization curves of Mn for various thicknesses deduced using the XMCD spin sum rule [55], plotted as functions of the external magnetic field $H_{\rm ext}$ (see Sec. 5.2 for the details of the sum-rule analysis). Since the direction of $H_{\rm ext}$ is perpendicular to the thin film, demagnetizing field has to be taken into account; That is, the effective magnetic field applied on the sample is given by $H = H_{\rm ext} + H_{\rm demag} = H_{\rm ext} - M$, where M is the magnetization (in units of A/m) of the sample. The magnetization curves after this correction for demagnetizing field are shown in Fig. 5.3(b). One can see that the saturation magnetic field decreases down to $\mu_0 H \sim 0.3$ - 0.8 T compared to the raw data plotted in Fig. 5.3(a), but is still an order of magnitude larger than those in the case of in-plane magnetic field ($\sim 10^{-2}$ T) [35,46,47,97]. This clearly shows that the LSMO thin films grown on the STO substrates favor in-plane magnetization

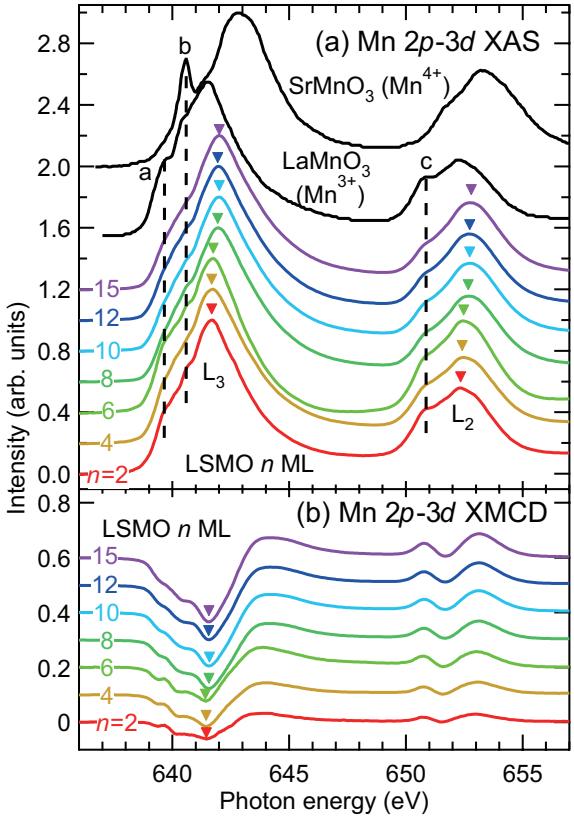

Figure 5.2: Mn $L_{2,3}$-edge XAS (a) and XMCD spectra (b) for $La_{0.6}Sr_{0.4}MnO_3$ (LSMO) thin films with varying thickness, measured at a temperature (T) of 20 K and under an external magnetic field ($\mu_0 H_{\rm ext}$) of 3 T. In panel (a), the XAS spectra for $LaMnO_3$ [95] and $SrMnO_3$ [96] are also shown as reference spectra for Mn^{3+} and Mn^{4+}, respectively.

due to magnetocrystalline anisotropy induced by the tensile epitaxial strain.

These magnetization curves have been decomposed into ferromagnetic and paramagnetic components, following the method of Ref. [98]. Namely, the magnetization component which saturates below $\mu_0 H \sim 1$ T has been regarded as the ferromagnetic component and the one which increases linearly with H up to the highest magnetic fields has been regarded as the paramagnetic component, as shown in the inset of Fig. 5.3(b). Thus, the intercept and the slope of the magnetization curve in the high-H region gives the ferromagnetic moment $M_{\rm ferro}$ and the paramagnetic susceptibility $\chi_{\rm para}$ of the Mn ions, respectively. The linear increase of M as a function of H up to 8 T has been confirmed for some samples, as shown in Fig. 5.3(c), which justifies the present method to separate the magnetization curves into the ferromagnetic and paramagnetic components. The deduced $M_{\rm ferro}$ and $\chi_{\rm para}$

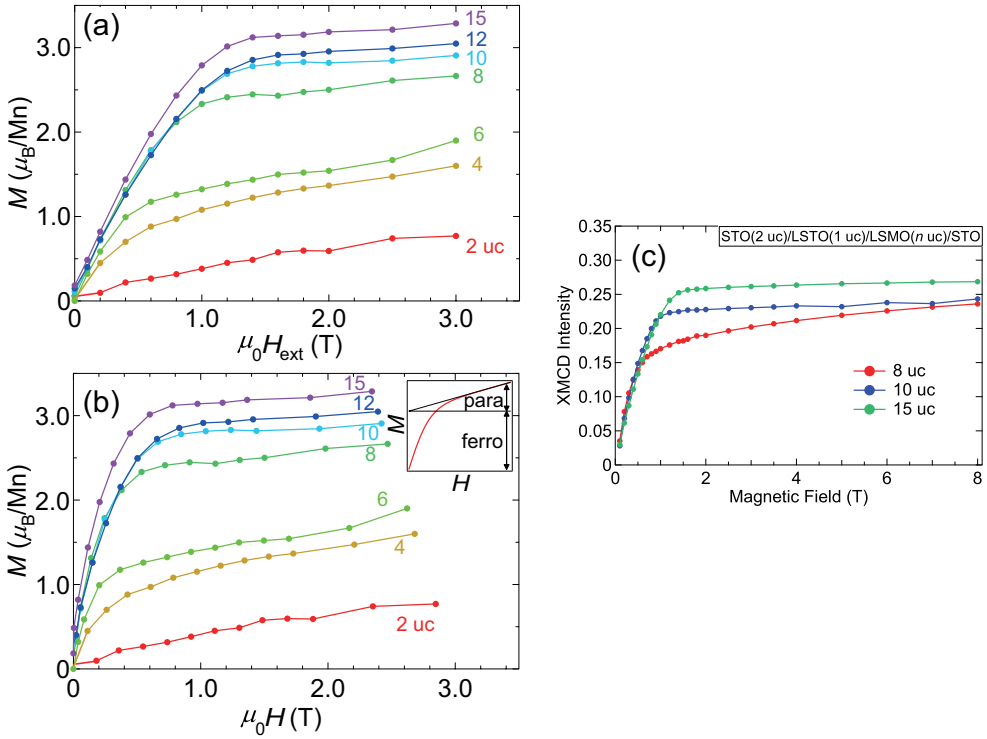

Figure 5.3: Magnetization curves of the studied LSMO/STO thin films deduced by XMCD. (a) Magnetization curves plotted as functions of the external magnetic field $H_{\rm ext}$. (b) Same data plotted as a function of the magneic field H after the correction for the demagnetizing field (see text for details). Inset in (b) schematically illustrates the method of the decomposition of the magnetization curves into ferromagnetic ($M_{\rm ferro}$) and paramagnetic ($M_{\rm para}$) components. (c) XMCD intensities up to high $H_{\rm ext}$ (≤ 8 T).

values are shown in Fig. 5.4(a) as functions of film thickness. A gradual decrease of $M_{\rm ferro}$ and a gradual increase of $\chi_{\rm para}$ are seen with decreasing thickness, reflecting the ferromagnetic-to-paramagnetic transition. In Fig. 5.4(a), the measured paramagnetic susceptibility $\chi_{\rm para}$ is compared to the one calculated from the Curie law ($\chi_{\rm para}^{\rm Curie}$) by the following equations:

$$\chi_{\rm para}^{\rm Curie} = \left[0.6\chi^{S=2} + 0.4\chi^{S=3/2}\right]\left(1 - \frac{M_{\rm ferro}}{M_0}\right), \tag{5.1}$$

$$\chi^S = \frac{S(S+1)g^2\mu_B}{3k_BT}, \tag{5.2}$$

where $g \simeq 2.0$ is the g-factor, $M_0 = 3.6\mu_B$/Mn is the full moment of Mn, and $1 - M_{\rm ferro}/M_0$ is the number ratio of the paramagnetic Mn atoms. The first and second terms of Eq. (5.1) represent the paramagnetic contribution

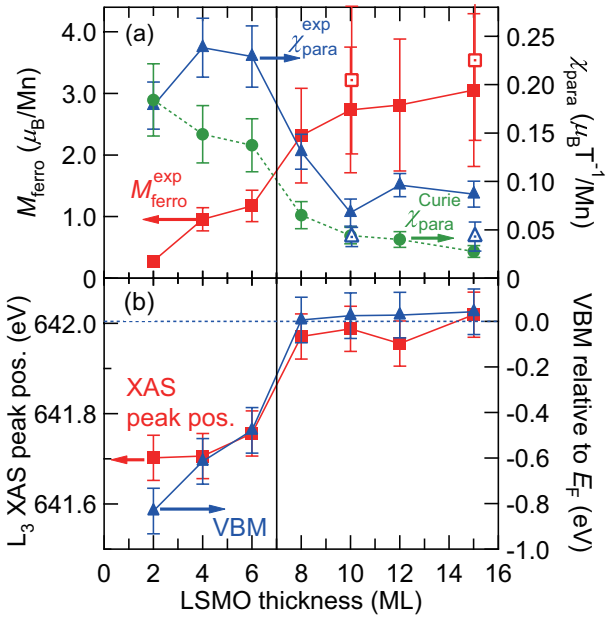

Figure 5.4: Magnetic and electronic properties of the LSMO thin films as a function of thickness. (a) Ferromagnetic moment per Mn (M_{ferro}, squares) and the paramagnetic susceptibility per Mn (χ_{para}, triangles) deduced from the magnetization curves in Fig. 5.3 (see text for the method). The paramagnetic susceptibility calculated from the Curie law ($\chi_{\mathrm{para}}^{\mathrm{Curie}}$) is also shown by circles for comparison. Open symbols represents M_{ferro} and χ_{para} deduced from the magnetization curves up to $\mu_0 H_{\mathrm{ext}} = 8$ T. (b) XAS peak position at the Mn L_3 edge (squares) and the valence band maximum (VBM) with respect to the Fermi level (E_F) estimated from photoemission spectroscopy [36] (triangles).

from the Mn^{3+} and Mn^{4+} ions, respectively. As can be seen from Fig. 5.4(a), the measured χ_{para} is slightly larger than $\chi_{\mathrm{para}}^{\mathrm{Curie}}$ in the entire thickness range, indicating that the Weiss temperature is positive. This means that ferromagnetic correlations between local magnetic moments of Mn still exist even in the paramagnetic phase.

It should be noted that the ferromagnetic-to-paramagnetic transition with decreasing thickness occurs rather *gradually* compared to the MIT. While the decrease of M_{ferro} and the increase of χ_{para} gradually occurs as shown in Fig. 5.4(a), the valence-band maximum (VBM) deduced from the PES measurement [36] rather abruptly changes at the critical thickness of MIT, as shown in Fig. 5.4(b). This suggests that there are some paramagnetic components even in the metallic phase above the critical thickness of the MIT and that part of the ferromagnetic component survives even in

the insulating phase. This result can be understood in terms of the phase-separation model (Sec. 2.2.3), i.e., both the ferromagnetic metallic (FM-M) phase and the paramagnetic insulating (PM-I) phase coexist around the critical thickness of the MIT, as ubiquitously observed around metal-insulator phase boundaries of manganites [23, 24]. Based on this model, the MIT can be described as the changes in the volume ratio between the two phases. The disappearance of the DOS at E_F can be explained by the reduction of the metallic domain sizes. In metal nanoparticles, loss of the DOS at E_F are commonly observed with the reduction of particle sizes due to surface effects, decrease of the bandwidth caused by the reduced coordination number, and quantum confinement effects [99, 100]. Similar effects are expected in the present case of randomly-distributed metallic domains.

In order to clarify how the electronic state evolves as a function of thickness, the line shapes of the XAS and XMCD spectra have been analyzed. The XAS spectra of $LaMnO_3$ (Mn^{3+}) [95] and $SrMnO_3$ (Mn^{4+}) [96] are shown in Fig. 5.2(a) as references, together with those of the LSMO thin films in the present study. By comparison between these XAS spectra, it can be seen that the shoulder structures a and c (originating from Mn^{3+}) are enhanced with decreasing thickness and that the maximum positions of the spectra at both the Mn L_3 and L_2 edges are abruptly shifted towards the lower photon energies ($h\nu$) by ~ 0.2 eV, below the critical thickness of the MIT. One can also see such peak shifts in the XMCD spectra across the critical thickness [Fig. 5.2(b)]. These peak shifts are considered to be originate from changes in the hole concentration of the Mn 3d bands: As shown in Fig. 5.2(b), both the L_3 and L_2 peak maxima are located at lower $h\nu$ for Mn^{3+} than for Mn^{4+}. It is also known that the peak position of the Mn XAS spectra are gradually shifted towards higher $h\nu$ with increasing Mn valence in mixed-valence manganese oxides [101]. The present result shows that the hole concentration of Mn abruptly drops across the critical thickness (6-8 UC), suggesting a close correlation between the Mn valence and the thickness-dependent MIT and ferromagnetic-to-paramagnetic transition. Note that the valence shift towards the Mn^{3+} side in thinner films are also reported in some previous studies [102, 103].

One possibility for the observed changes in the Mn valence towards 3+ with decreasing film thickness is electron doping at the interface from the LSTO layer in the cap. As shown in Fig. 5.1, the studied thin films have one UC of LSTO layer between the LSMO and STO layers, and the $(LSO)^{0.6+}$ monolayer in this LSTO layer serves as an electron donor. Since the work function of LSMO is larger than that of STO [104], it is expected that the electrons from the LSO donors are doped into the LSMO side rather than the STO side. In thinner films, this interfacial doping effect becomes more

significant because the volume ratio of the interface to the bulk increases, and thus the shift of the average Mn valence from 3.4+ to 3+ can be explained. It should be noted, however, this doping effect alone is not sufficient to explain the magnitude of the valence shift for the 4- and 6-UC-thick films, in which the Mn valence is comparable to that of the 2-UC film. It is also possible that there are some oxygen vacancies in the LSMO films and/or the STO substrates, which also serves as electron donors in addition to the mechanism mentioned above. Note that the valence of Mn in perovskite-type manganite thin films tends to be lower than the nominal value in general [45].

The abrupt valence change at the critical thickness of the MIT (6-8 UC) implies a close correlation between the MIT and the valence of Mn. One possiblility is that the MIT leads to a re-distribution of the charged carriers within the LSMO film. In thicker films, the system is metallic and the carriers (holes) tend to be distributed at the top and bottom interfaces of the LSMO layer, in order to cancel out the potential gradient inside the film [25, 28]. When the film thickness is reduced, the system turns into the insulating phase and holes are distributed uniformly over the entire film. Since XAS and XMCD in the TEY mode are a relatively surface-sensitive detection technique (with probing depths of $\sim$ 3-5 nm [105]), the observed Mn valence can abruptly change if the charged carriers near the bottom interface are distributed in a more extended region below the critical thickness of the MIT. In order to test these hypotheses, further studies would be necessary on the depth profiles of the charged carriers and magnetism for LSMO thin films with various stacking structures.

5.4 Conclusion

In this chapter, the thickness dependencies of the magnetism and the electronic structure of LSMO ($x = 0.4$) thin films have been investigated via XAS and XMCD in order to clarify the mechanism of the thickness-dependent MIT and concomitant magnetic transition. From the analyses of the magnetization curves measured by XMCD, it has been shown that the ferromagnetic component *gradually* decreases while the paramagnetic one *gradually* increases with decreasing film thickness. The paramagnetic susceptibility is shown to be larger than that deduced from the Curie law, indicating the ferromagnetic spin correlations between the local Mn moments. The gradual magnetic transition is in contrast to the abrupt MIT and the concomitant valence shift towards Mn^{3+} below the critical thickness. This difference between the electronic and magnetic transition can be understood within the phase-separation model between the FM-M and the PM-I phases.

Chapter 6

Anisotropic spin density in $La_{0.7}Sr_{0.3}MnO_3$ thin films probed by angle-dependent x-ray magnetic circular dichroism

Part of this chapter has been published in "Anisotropic spin-density distribution and magnetic anisotropy of strained $La_{1-x}Sr_xMnO_3$ thin films: Angle-dependent x-ray magnetic circular dichroism", G. Shibata, M. Kitamura, M. Minohara, K. Yoshimatsu, T. Kadono, K. Ishigami, T. Harano, Y. Takahashi, S. Sakamoto, Y. Nonaka, K. Ikeda, Z. Chi, M. Furuse, S. Fuchino, M. Okano, J.-i. Fujihira, A. Uchida, K. Watanabe, H. Fujihira, S. Fujihira, A. Tanaka, H. Kumigashira, T. Koide, and A. Fujimori, npj Quantum Mater. **3**, 3 (2018).

6.1 Introduction

Understanding the origin of magnetic anisotropy in ferromagnetic materials and controlling it has been a major issue in both the fundamental and applied science [1]. In the field of applied science, many attempts have been made to enhance the magnetic anisotropy of ferromagnets, aiming at the realization of high-density information-storage devices and high-power motors. In the field of fundamental science, the microscopic origin of magnetic anisotropy has been discussed extensively. Magnetic anisotropy generally emerges as a consequence of the complex interplay between spin-orbit interaction (SOI), band structures, spin and orbital magnetic moments, and

orbital occupation. The magnetic anisotropy of ferromagnetic thin films is of particular interest, because it is controlled by various external factors, such as film thickness, carrier doping at the interfaces, and epitaxial strain due to the lattice mismatch between the film and the substrate.

Perovskite-type manganese oxide $La_{1-x}Sr_xMnO_3$ (LSMO), which is well-known for its intriguing transport and magnetic properties such as colossal magnetoresistance (CMR) and half-metallicity, is one of the candidate materials for spintronics and its physical properties have been extensively studied for decades [9]. It is in the ferromagnetic metallic (FM-M) phase at the doping levels of $0.175 \lesssim x \lesssim 0.5$, with Curie temperatures above the room temperature ($T_C \sim 370$ K at $x \sim 0.3$) [106]. When LSMO is grown in a form of thin films, their physical properties are also affected by various external factors. It has been shown, for example, that the FM-M nature of LSMO at the doping levels of $0.3 \leq x \leq 0.5$ is lost under strong epitaxial strain, and the film turns into the A-type antiferromagnetic (AFM) metallic phase in the case of tensile strain [e.g., on the $SrTiO_3$ (STO) (001) substrate], or the C-type AFM insulating phase in the case of compressive strain [e.g., on the $LaAlO_3$ (LAO) (001) substrate] [19]. The magnetic anisotropy of the LSMO thin films is also affected by the strain, namely, they have out-of-plane magnetic easy axis in the case of the LAO substrate (compressive strain) and have in-plnae magnetic easy axes in the case of the STO substrate (tensile strain) [46, 47]. According to the first-principles calculations [19], it has been pointed out that the $d_{x^2-y^2}$ orbital is more preferentially occupied if tensile strain is applied on the film, and that the $d_{3z^2-r^2}$ orbital is more preferentially occupied if compressive strain is applied on the film. This result implies a close correlation between the magnetic anisotropy and the preferential orbital occupation of the Mn $3d$ electrons. However, previous studies by x-ray linear dichroism (XLD) spectroscopy have shown that the $d_{3z^2-r^2}$ orbital is always more preferentially occupied than the $d_{x^2-y^2}$ orbital, irrespective of the sign of the epitaxial strain [49–51]. So far, this apparent discrepancy has been considered to originate from the different orbital occupation between the surface and the bulk: They assume that the $d_{3z^2-r^2}$ orbital is more preferentially occupied due to the spatial symmetry breaking at the surface and the interface, [49–51]. Although this model reasonably explains the results of XRD, no direct information about the orbital occupation in the bulk of the LSMO thin films and its relationship between the magnetism has been obtained so far.

In this study, preferential orbital occupation and magnetic anisotropy in LSMO thin films grown on STO (tensile) and LAO (compressive) substrates have been investigated by angle-dependent x-ray magnetic circular dichroism (XMCD). As shown below, this method can directly probe the prefer-

ential orbital occupation of *spin-polarized* electrons, i.e., the anisotropy of spin-density distribution. This can be realized by extracting the 'magnetic dipole' $\boldsymbol{M}_{\mathrm{T}}$ which appears in the XMCD spin sum rule [55] in addition to the spin magnetic moment $\boldsymbol{M}_{\mathrm{spin}}$. $\boldsymbol{M}_{\mathrm{T}}$ represents the anisotropy of the spatial distribution of spin density, i.e., the shape of the orbitals of spin-polarized electrons. In contrast to XLD, which probes the orbital polarization of *all* the valence electrons, angle-dependent XMCD probes the orbital polarization of only *spin-polarized* electrons, which enables one to directly deduce the preferential orbital occupation of electrons participating in ferromagnetism. Although it is in general hard to separate the XMCD signals into the components originating from $\boldsymbol{M}_{\mathrm{spin}}$ and $\boldsymbol{M}_{\mathrm{T}}$ by a single XMCD measurement, it can be done, as described below, by measuring the angular dependence of the XMCD spectra as a function of magnetic-field direction ($\theta_{\boldsymbol{H}}$) because the two components have different angular dependencies, [2, 3, 59, 107]. Especially, the XMCD signal from the magnetic dipole $\boldsymbol{M}_{\mathrm{T}}$ can be directly extracted in such a geometry that $\boldsymbol{M}_{\mathrm{spin}}$ is aligned perpendicular to the incident x rays, which allows one to determine the anisotropy of the spin-density distribution [3]. Although this kind of XMCD measurement, transverse XMCD (TXMCD), was theoretically proposed long time ago [2,3,59,107,108], there have been very limited number of TXMCD experiments [109–112] due to the restriction that the direction of the magnetic field produced by the electromagnet is fixed parallel to the incident light in conventional measurement systems. This restriction has been recently resolved by the development of an XMCD measurement system with a vector-type magnet, in which one can apply the magnetic field along various directions using two pairs of superconducting magnets [4]. This chapter describes the angle-dependent XMCD and TXMCD studies on ferromagnetic LSMO ($x = 0.3$) thin films grown on STO and LAO substrates, and discusses the relationship between the epitaxial strain and the anisotropy of the spin-density distribution. It has been found that the preferential orbital occupation of spin-polarized electrons in the studied LSMO films is $d_{x^2-y^2}$-like in the case of tensile epitaxial strain (STO substrate) and is $d_{3z^2-r^2}$-like in the case of compressive epitaxial strain (LAO substrate), which are different from the orbital occupation deduced from XLD. This is ascribed to the difference between the spin- and charge-density distributions, i.e. the preferential occupation of both the spin-up and spin-down $d_{3z^2-r^2}$ orbitals at the surface, which may be the origin of the surface magnetic dead layers in LSMO.

6.2 Experimetal

LSMO ($x = 0.3$) thin films with thicknesses of $\sim$ 100 unit cells ($\sim$ 40 nm) were fabricated on AlO_2-terminated LAO (001) and TiO_2-terminated Nb-doped STO (001) substrates by the laser molecular beam epitaxy method [91]. The films undergo tensile and compressive strain from the STO and LAO substrate, respectively, due to the differences of the lattice constants between LSMO and the substrates. The LSMO thin films were deposited in an oxydizing atmosphere ($P_{O_2} = 1 \times 10^{-4}$ Torr). The deposition temperatures were 1050 °C for the STO substrate and 650 °C for the LAO substrate. The growth conditions for the LSMO/STO film was essentially the same as the previous study [113]. The growth conditions for the LSMO/LAO film was chosen so that the film is *partially* strained, since it tends to be an antiferromagnetic insulator if the film is fully strained [19]. The growth rate was monitored by the intensity oscillation of the specular spot in reflection high-energy electron diffraction (RHEED). The films were post-annealed at 400 °C in oxygen ($P_{O_2} = 1 \times 1$ bar) for 45 minutes at after the deposition in order to eliminate oxygen vacancies. In order to confirm that the grown LSMO thin films are well strained and at the same time are in the ferromagnetic metallic phase, the grown films were characterized by x-ray diffraction (XRD), magnetization measurement using a superconducting quantum interference device (SQUID), and resistivity measurement using the four-probe method. The XRD measurements were performed using a synchrotron light source at BL-7C of Photon Factory, High Energy Accelerator Research Organization (KEK-PF), and a laboratory light source using the Cu $K\alpha$ line.

The angle-dependent XMCD measurements were done using the vector-magnet XMCD apparatus (see Sec. 4.1 and Ref. [4] for details) installed at BL-16A2 of KEK-PF. The measurements were performed at 30 K for the LSMO/LAO film and at 270 K for the LSMO/STO film. A lower temperature was chosen for the LAO substrate since the saturation magnetization (M_{sat}) was low at room temperature [as shown in Fig. 6.2(d)], whereas a higher temperature was chosen for the STO substrate since the magnetic anisotropy energy (MAE) was so large at low temperature that it was not possible to totally align the electron spins along the film-normal direction (the magnetically hard axis). The XAS signals were collected using the total electron-yield (TEY) mode. A negative bias voltage of $\sim$ 200 V was applied on the sample in order to help the ejection of the photoelectrons. This is of importance especially in the case of in-plane magnetic field, because the trajectories of the photoelectrons are bent by the Lorentz force and they are absorbed back to the sample, resulting in a drop of the photocurrent down to almost zero. The base pressure of the measurement chamber was

$\sim 1 \times 10^{-9}$ Torr.

6.3 Results

6.3.1 Sample characterization

Figure 6.1(a) and 6.1(b) show the results of the XRD measurements in the specular geometry for the LSMO/STO films (grown at 1050 °C) and LSMO/LAO film (grown at 650 °C), respectively. For both the films, a sharp peak and a broader peak are observed, which correspond to the diffraction peaks from the substrate and the LSMO film, respectively. The out-of-plane lattice constants of LSMO can be deduced from the peak positions and have been estimated to be 0.386 nm and 0.401 nm for the STO and LAO substrates, respectively. By comparison with the lattice constant of bulk LSMO (0.389 nm), it can be confirmed that the LSMO/STO (LSMO/LAO) film undergoes a tensile (compressive) strain from the substrate. Furthermore, the XRD patterns for both the films exhibit clear oscillation fringes around the main peak, indicating that the roughness of the surface and the interface between the film and the substrate is small.

In order to get information about the in-plane lattice constants more directly, XRD measurements using the LSMO (103) diffraction peak have been also performed. Figures 6.1(c), 6.1(d), and 6.1(e) show the reciprocal space maps (RMSs) for the LSMO/STO film grown at 1050 °C, LSMO/LAO film grown at 650 °C, and LSMO/LAO film grown at 600 °C, respectively. The films on the LAO substrates have been grown under several different temperatures and two representative data are shown here. As for the LSMO/STO film [Fig. 6.1(c)] and the LSMO/LAO film grown at lower temperature [Fig. 6.1(e)], the diffraction peak from LSMO is located at the same Q_x as the substrate, suggesting that the films are fully strained. In contrast, the LSMO/LAO film grown at higher temperature [Fig. 6.1(d)] exhibits more diffuse diffraction spot from LSMO, in that the spot is split into two peaks and has tails towards the low-Q_x and high-Q_z sides. This shows that the average in-plane lattice constant of LSMO is longer than that of LAO, showing that the compressive epitaxial strain from LAO is partially relaxed. It should be also mentioned that the LSMO/LAO film were totally relaxed if the growth temperature was further raised up to 1000 °C, consistent with the previous study [19].

The magnetic hysteresis curves (M-H curves) of the LSMO/STO film and the partially relaxed LSMO/LAO film (grown at 650 °C) are shown in Figs. 6.2(a) and 6.2(b), respectively. The evolution of the magnetization (M) with lowering temperature (T) for the LSMO/STO, partially-relaxed

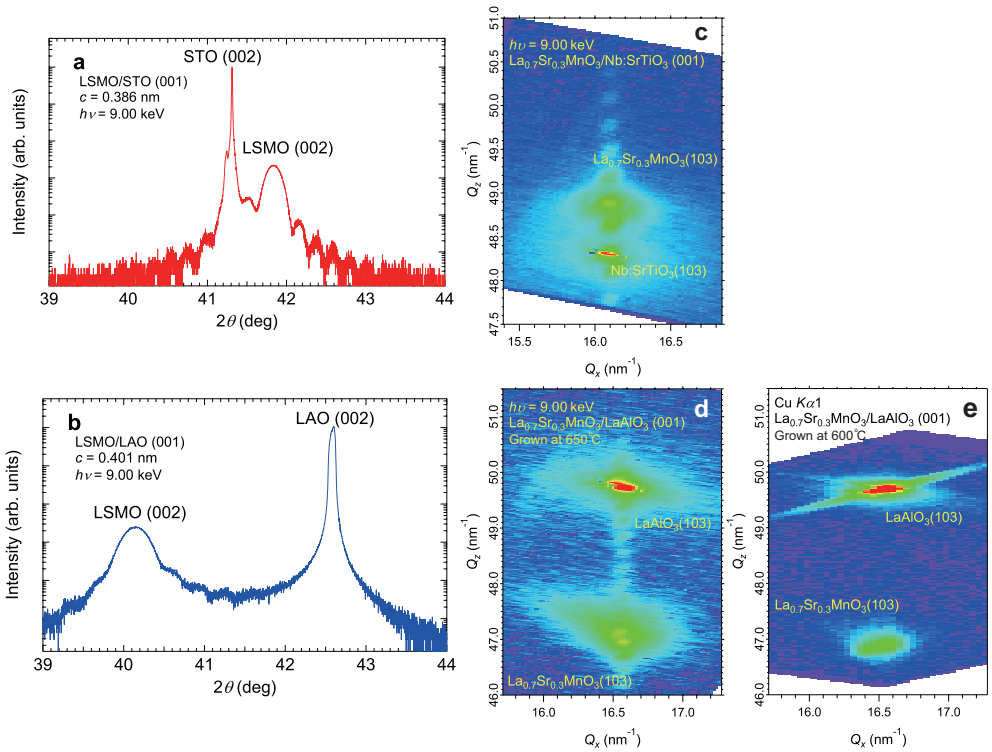

Figure 6.1: Structural characterization of the grown $La_{1-x}Sr_xMnO_3$ (LSMO) thin films ($x = 0.3$) by x-ray diffraction (XRD). (a)(b) XRD patterns measured in a specular geometry for the LSMO thin films grown on the Nb-doped $SrTiO_3$ (STO) (001) (a) and $LaAlO_3$ (LAO) (b) substrates. The out-of-plane lattice constants (c) are estimated to be 0.386 nm and 0.401 nm for the STO and LAO substrates, respectively. (c)-(e) Reciprocal space mappings (RSMs) measured using the (103) x-ray diffraction peak for the LSMO/STO film (c), LSMO/LAO film grown at 650 °C (d), and LSMO/LAO film grown at 600 °C (e). Here, the reciprocal lattice vector $\boldsymbol{Q}$ is defined by $\boldsymbol{Q} = \frac{2\pi}{\lambda}(\hat{\boldsymbol{k}}_f - \hat{\boldsymbol{k}}_i)$, where λ is the wavelength of the x ray, and $\hat{\boldsymbol{k}}_i$ and $\hat{\boldsymbol{k}}_f$ are the unit vectors along the incident and diffracted x rays, respectively.

LSMO/LAO (grown at 650 °C), and fully-strained LSMO/LAO (grown at 600 °C) thin films are shown in Figs. 6.2(c) and 6.2(d). The hysteresis curves in Figs. 6.2(a) and 6.2(b) show that the out-of-plane direction is the magnetic hard (easy) axis in the case of the STO (LAO) substrate, in agreement with previous studies [46, 47]. The saturation magnetization of the LSMO/STO film at low temperature estimated from the M-T curves in Fig. 6.2(c) is comparable to that of the bulk (3.7 μ_B/Mn). indicating that the majority part of the film is in the ferromagnetic phase. In the case of the LSMO/LAO films, on the other hand, only the partially-relaxed

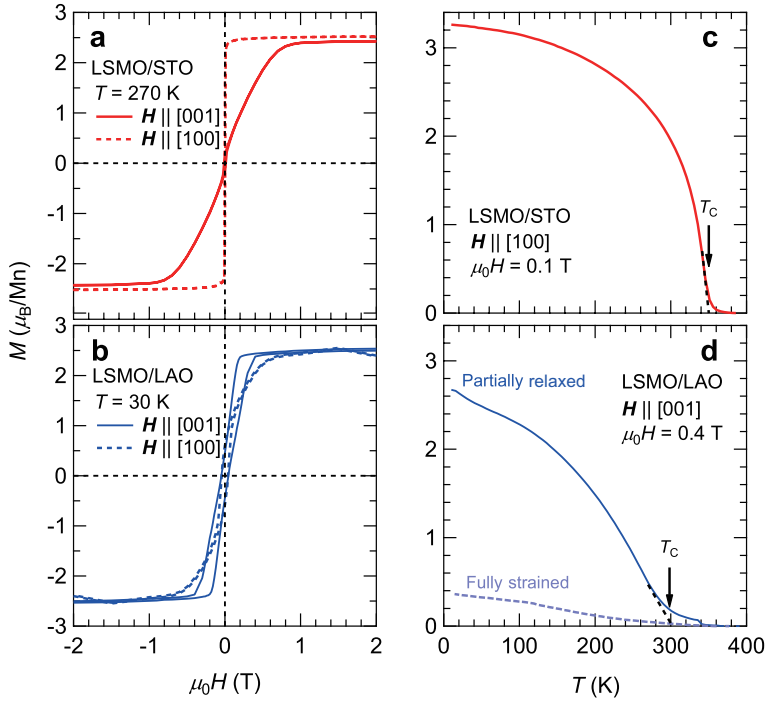

Figure 6.2: Magnetization data measured using a superconducting quantum interference device (SQUID) magnetometer. (a)(b) Magnetic hysteresis curves of the LSMO/STO (a) and partially-relaxed LSMO/LAO (b) thin films (grown at 650 °C). (c)(d) Temperature (T) dependencies of the magnetization (M) for the LSMO/STO (c) and LSMO/LAO (d) thin films. For LSMO/LAO, the data for the partially-relaxed film (solid curve) and the fully-strained film (grown at 600 °C, dashed curve) are shown.

film exhibits a relatively large saturation magnetization ($\sim$ 2.5 μ_B/Mn) and the fully-strained film shows quite small saturation magnetization ($\sim$ 0.4 μ_B/Mn) compared to the bulk. This shows that the ferromagnetism of LSMO is nearly suppressed in the latter film. The former sample with partial epitaxial strain has been therefore chosen for the XMCD measurements in the following. The Curie temperatures (T_C) of the LSMO/STO film and the partially-relaxed LSMO/LAO film are estimated to be 350 $\pm$ 5 K and 300 $\pm$ 10 K, respectively. These values are slightly lower than the bulk Curie temperature (T_C^{bulk} $\sim$ 370 K), which can be ascribed to the strain effect [19, 35].

Figure 6.3 shows the T-dependencies of the resistivity (ρ) for the grown LSMO/LAO films with partial strain (grown at 650 °C) and full strain (grown at 600 °C). It can be seen that the partially-relaxed LSMO/LAO film exhibits metallic behavior below the transition temperature (T_{MIT}) of

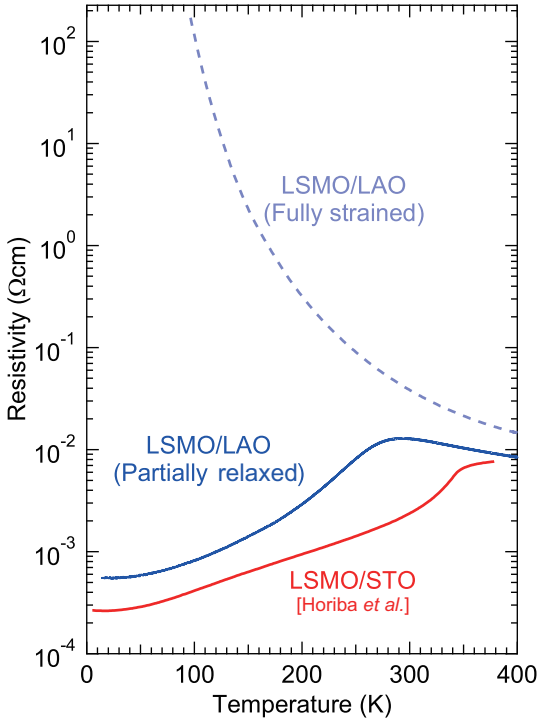

Figure 6.3: Resistitity data for the grown LSMO/LAO films with partial strain (grown at 650 °C) and full strain (grown at 600 °C). Since the resistivity measurements were not possible for the LSMO/STO film because of the conductive Nb-doped STO substrate, the resistivity data for another LSMO/STO film grown under similar conditions as the present study is shown here as a reference [113].

290±5 K, while the fully-strained one shows insulating behavior in the entire temperature range. It is therefore concluded that the partially-relaxed film is in the ferromagnetic metallic (FM-M) phase similar to the bulk, whereas the fully-strained one is in the antiferromagnetic insulating (AFM-I) phase, as reported in the previous study [19]. The resistivity measurements were not possible for the LSMO/STO film because of the conductive Nb-doped STO substrate. However, the LSMO/STO thin film which was grown under similar conditions to the present study by using the same apparatus is shown to be metallic, as shown in Fig. 6.3 [113] ($T_{\mathrm{MIT}} = 345 \pm 5$ K). In addition, the magnetization data in Fig. 6.2(c) shows that the Curie temperature T_{C} is almost comparable to that of the bulk. This rules out the possibility that the studied LSMO/STO film is in the ferromagnetic insulating (FM-I) phase, because the T_{C} in the FM-I phase is lower than 300 K [106]. These are indirect evidence that the grown LSMO/STO film is in the FM-M phase similar to the bulk.

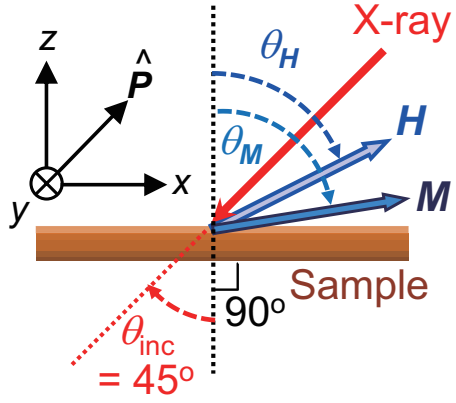

Figure 6.4: Schematic description of the experimental geometry for angle-dependent x-ray magnetic circular dichroism (XMCD). The angles of the incident x rays ($\theta_{\rm inc}$), the applied magnetic field ($\theta_{\boldsymbol{H}}$), and the magnetization ($\theta_{\boldsymbol{M}}$). are measured from the sample normal. $\theta_{\rm inc}$ was fixed at 45° in the present study. $\hat{\boldsymbol{P}}$ is a unit vector along the x-ray incident direction, which is defined to be antiparallel to the wavevector of x rays $\boldsymbol{k}$.

6.3.2 Angular dependence of the XMCD spectra and transverse XMCD

Figure 6.4 is a schematic description of the experimental geometry for angle-dependent XMCD. The direction of the magnetic field can be varied by using two pairs of superconducting magnet coils [see Fig. 4.1]. The angles of the incident x rays ($\theta_{\rm inc}$), the applied magnetic field ($\theta_{\boldsymbol{H}}$), and the magnetization ($\theta_{\boldsymbol{M}}$). are measured from the sample normal, as shown in the figure. The x-ray incident angle $\theta_{\rm inc}$ was fixed at 45° in the present study and the field direction $\theta_{\boldsymbol{H}}$ was varied in order to change the magnetization direction $\theta_{\boldsymbol{M}}$. It should be noted that $\theta_{\boldsymbol{M}}$ is in general different from $\theta_{\boldsymbol{H}}$ if there is magnetic anisotropy and the applied magnetic field is not strong enough to completely align the electron spins along the field direction. The XMCD sum rules [54, 55] dictate that one can deduce from the spectral intensities of XMCD the projection of the 'effective' spin magnetic moment ($\boldsymbol{M}_{\rm spin}^{\rm eff} \equiv \boldsymbol{M}_{\rm spin} + (7/2)\boldsymbol{M}_{\rm T}$) onto the incident x rays, namely, $\hat{\boldsymbol{P}} \cdot [\boldsymbol{M}_{\rm spin} + (7/2)\boldsymbol{M}_{\rm T}]$ [see Eq. (3.3)]. In systems where the orbital magnetic moment $\boldsymbol{M}_{\rm orb}$ and the magnetic dipole $\boldsymbol{M}_{\rm T}$ are much smaller than $\boldsymbol{M}_{\rm spin}$, as in $3d$ transition-metal ferromagnetic materials, the XMCD intensity is approximately proportional to the projection of the spin magnetic moment onto the incident x rays, i.e., $\hat{\boldsymbol{P}} \cdot \boldsymbol{M}_{\rm spin}$. More detailed explanations about the principles of angle-dependent XMCD are given in Sec. 4.3.

The Mn-$L_{2,3}$ ($2p \rightarrow 3d$) XAS spectra of the LSMO thin films grown on the STO and LAO substrates are shown in Figs. 6.5(a) and 6.5(b), respectively, The light-red and light-blue curves represent the XAS spectra for positive ($\sigma+$) and negative ($\sigma-$) circular polarizations, respectively, and the green curves represent the XAS spectra averaged over both the polarizations. Since the spectral line shape of the polarization-averaged spectra was nearly identical irrespective of the magnetic-field direction $\theta_{\boldsymbol{H}}$, as shown in Fig. 6.6, only the XAS spectra measured at $\theta_{\boldsymbol{H}} = 45°$ (the magnetic field being parallel to the incident light) are shown in Fig. 6.5. The spectral line shape of XAS is similar to those of bulk [92] and thin-film [50, 114] samples in previous studies. The XAS signals of extrinsic Mn^{2+}, which is often observed in manganite thin films due to the presence of oxygen vacancies [45], are hardly observed, indicating that the grown LSMO thin films have correct stoichiometry. Figures 6.5(c) and 6.5(d) show the Mn $L_{2,3}$-edge XMCD spectra for the LSMO/STO and LSMO/LAO films, respectively, with varying magnetic-field angle $\theta_{\boldsymbol{H}}$. The XMCD intensity at the Mn L_3 edge (which is approximately proportional to the projected spin magnetic moment $\hat{\boldsymbol{P}} \cdot \boldsymbol{M}_{\rm spin}$) gradually changes as a function of $\theta_{\boldsymbol{H}}$, due to the systematic changes in the magnetization direction $\theta_{\boldsymbol{M}}$. The reversal of the XMCD intensity at the Mn L_3 edge occurs around $\theta_{\boldsymbol{H}} = -15°$ - $-$ $20°$ in Fig. 6.5(c) and around $\theta_{\boldsymbol{H}} = -50°$ - $-$ $55°$ in Fig. 6.5(d). This suggests that the magnetization direction is nearly perpendicular to the incident x rays around these magnetic-field angles, namely, the TXMCD geometry is realized around these $\theta_{\boldsymbol{H}}$'s.

These XMCD spectra around the TXMCD geometry are shown in Fig. 6.7(a) with a magnified scale. The orange and green curves, respectively, represents the XMCD spectra of the LSMO/STO film measured at $\theta_{\boldsymbol{H}} = -20°$ and of the LSMO/LAO film measured at $\theta_{\boldsymbol{H}} = -50°$. Clear TXMCD signals can be observed, which are expected to originate from the magnetic dipole $\boldsymbol{M}_{\rm T}$. One might suspect that $\boldsymbol{M}_{\rm spin}$ is slightly deviated from the perpendicular direction to the x rays and these misaligned $\boldsymbol{M}_{\rm spin}$, rather than $\boldsymbol{M}_{\rm T}$, yield these finite XMCD signals. This possibility, however, can be ruled out because the spectral line shapes of XMCD in Fig. 6.7(a) are entirely different from the conventional ('longitudinal') XMCD spectra shown by the black curve in Fig. 6.7(a), which mainly originates from $\boldsymbol{M}_{\rm spin}$. Moreover, the spectral line shapes of LSMO/STO and LSMO/LAO are almost identical except for the sign difference, suggesting that they have the same physical origin. These results demonstrate that the LSMO/STO and LSMO/LAO films have the opposite signs of $\boldsymbol{M}_{\rm T}$, namely, they have opposite spin-density distribution reflecting the opposite signs of epitaxial strain.

In order to further confirm that the obtained XMCD spectra are gen-

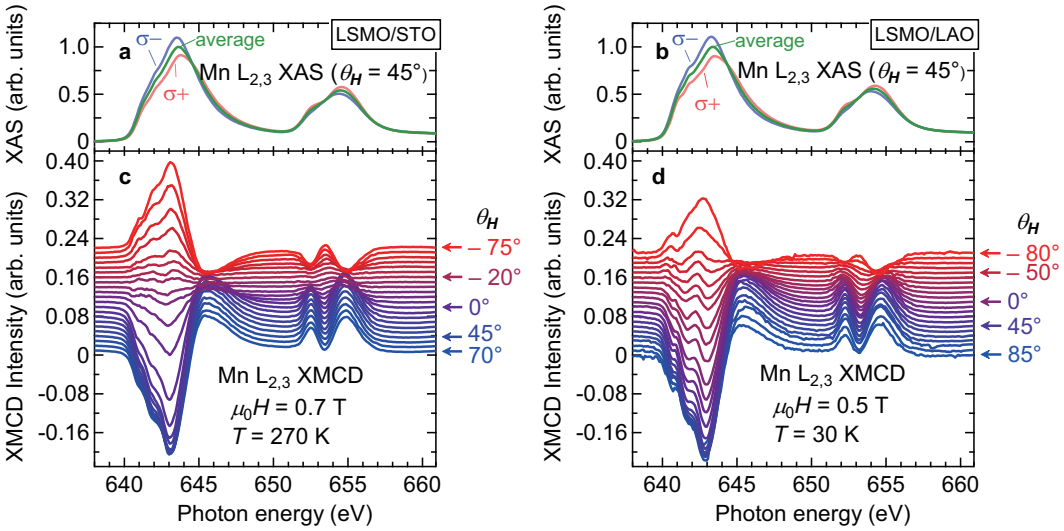

Figure 6.5: X-ray absorption spectroscopy (XAS) and XMCD spectra of the LSMO ($x = 0.3$) thin films at the Mn $L_{2,3}$ absorption edges. (a)(b) XAS spectra for the films grown on the (a) Nb-doped $SrTiO_3$ (STO) (001) and (b) $LaAlO_3$ (LAO) (001) substrates. The light-red and light-blue curves represent the XAS spectra for positive ($\sigma+$) and negative ($\sigma-$) circular polarizations, respectively. The green curves represent the XAS spectra averaged over both the polarizations. The peak height of the averaged XAS is normalized to unity. (c)(d) XMCD spectra of the LSMO thin films grown on the (c) STO and (d) LAO substrates for varying θ_H, measured in the geometry described in Fig. 6.4.

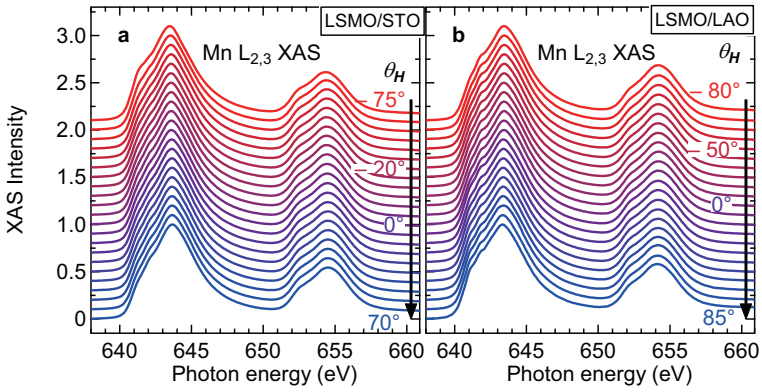

Figure 6.6: Polarization-averaged Mn-$L_{2,3}$XAS spectra of the (a) LSMO/STO and (b) LSMO/LAO films for various θ_H's.

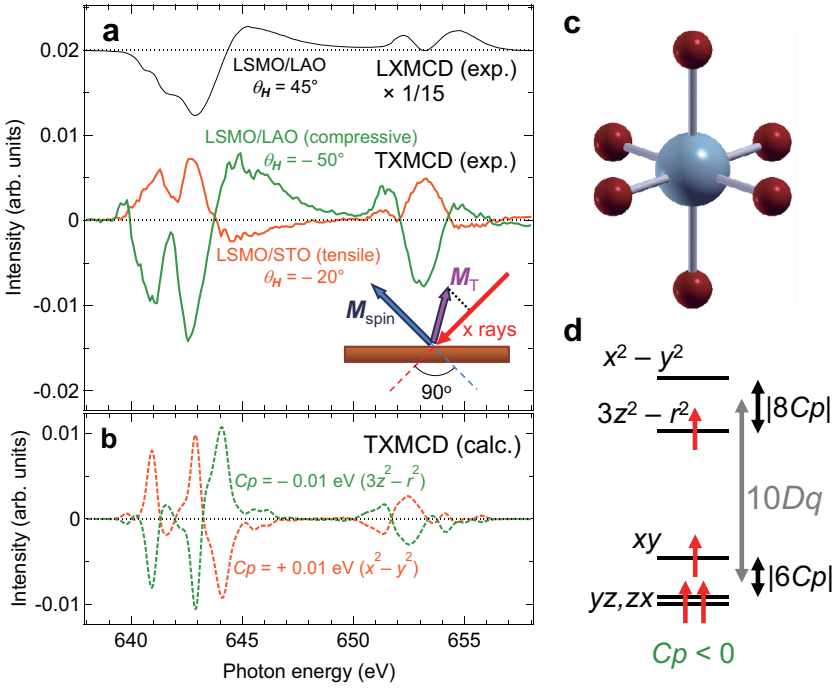

Figure 6.7: XMCD spectra in the transverse geometry. (a) Experimental transverse XMCD (TXMCD) spectra of the LSMO/STO (orange) and LSMO/LAO (green) films, plotted together with a longitudinal XMCD (LXMCD) spectra (black). Inset schematically describes the geometry of TXMCD. (b) TXMCD spectra based on the cluster-model calculation. (c) $Mn^{3+}O_6$ cluster model under the D_{4h} symmetry, which has been used in the present calculation. (d) Schematic drawing of the energy levels of the Mn $3d$ orbitals within the cluster model of panel (c). $8Cp$ denotes the crystal-field splitting between the $3z^2 - r^2$ and $x^2 - y^2$ levels [111], and the positive (negative) Cp describe the cases where the $3z^2 - r^2$ ($x^2 - y^2$) orbital has higher energy than the $x^2 - y^2$ ($3z^2 - r^2$) orbital. Panels (c) and (d) describe the case of $Cp < 0$. The parameter values used for the cluster-model calculation are listed in Table 6.1. Panel (c) has been drawn using XCrySDen [22].

uine TXMCD signals, the experimental spectra have been compared with the theoretical TXMCD spectra calculated based on the $Mn^{3+}O_6$ cluster model under the D_{4h} symmetry (see Sec. 3.4 for details of the cluster-model calculation). Only the Mn^{3+} (d^4) valence state has been taken into account in the present calculation, because the charge density should be isotropic in the Mn^{4+} (d^3) valence state (in which the $t_{2g\uparrow}$ levels are fully occupied and the $e_{g\uparrow}$ levels are empty). The parameter values used for the calculation are listed in Table 6.1. The effect of the tensile or compressive epitaxial strain has been incorporated by changing the sign of the tetragonal crystal field Cp

Table 6.1: Parameter values used for the cluster-model calculation of the TXMCD spectra in Fig. 6.7(b) (in eV). The meaning of the parameters are as follows: U_{dd}: 3d-3d Coulomb interaction, U_{pd}: 2p-3d Coulomb interaction, Δ: Charge-transfer energy, $(pd\sigma)$: Slater-Koster parameter, $10Dq$: Crystal-field splitting between the e_g and t_{2g} levels, $8Cp$: Crystal-field splitting between the x^2-y^2 and $3z^2-r^2$ levels ($Cp > 0$ represents that the $3z^2-r^2$ orbital has higher energy than the x^2-y^2 orbital [111]).

U_{dd}	U_{pd}	Δ	$(pd\sigma)$	$10Dq$	$\lvert 8Cp \rvert$
7.0	8.5	4.0	2.0	1.5	0.08

[see Fig. 6.7(d) for definition]. The calculated TXMCD spectra for a tensile strain ($Cp = +0.01$ eV) and for a compressive strain ($Cp = -0.01$ eV) are shown in Fig. 6.7(b). The calculated TXMCD spectra reasonably reproduce the experimental ones in Fig. 6.7(a), indicating that genuine TXMCD spectra have been experimentally obtained. By comparison of the signs of the experimental TXMCD spectra with the calculated ones, it is demonstrated that the spin-density distribution of the Mn 3d electrons is more $d_{x^2-y^2}$-like in the case of STO substrate (tensile strain) and is more $d_{3z^2-r^2}$-like in the case of LAO substrate (compressive strain). This result is consistent with what is expected from the sign of the epitaxial strain from the substrates.

6.3.3 Quantitative estimate of magnetic anisotropy energy and anisotropic spin-density distribution

The angle-dependent XMCD spectra in Figs. 6.5(c) and 6.5(d) show that the sign of the projected spin magnetic moment ($\hat{\boldsymbol{P}} \cdot \boldsymbol{M}_{\rm spin}$) reverses around $\theta_{\boldsymbol{H}} \simeq -20^\circ$ for LSMO/STO and $\theta_{\boldsymbol{H}} \simeq -50^\circ$ for LSMO/LAO. Without magnetic anisotropy, $\theta_{\boldsymbol{M}}$ would be always equal to $\theta_{\boldsymbol{H}}$ and the sign change of the XMCD spectra would occur at $\theta_{\boldsymbol{H}} = -45^\circ$, where the applied magnetic field is perpendicular to the incident light. The fact that the sign change angles are deviated from $\theta_{\boldsymbol{H}} = -45^\circ$ in the present experiment suggests that $\theta_{\boldsymbol{M}} \neq \theta_{\boldsymbol{H}}$ due to the presence of magnetic anisotropy. By fitting the experimental angular dependence of the projected magnetic moment to the theoretical curve, it is expected that one can deduce the sign and magnitude of the magnetic anisotropy energy (MAE).

Figure 6.8 shows the $\theta_{\boldsymbol{H}}$-dependence of the effective spin magnetic moment $\boldsymbol{M}_{\rm spin}^{\rm eff}$ projected onto the incident x rays [$\hat{\boldsymbol{P}} \cdot \boldsymbol{M}_{\rm spin}^{\rm eff}$ ($\equiv \hat{\boldsymbol{P}} \cdot [\boldsymbol{M}_{\rm spin} + (7/2)\boldsymbol{M}_{\rm T}] \simeq \hat{\boldsymbol{P}} \cdot \boldsymbol{M}_{\rm spin}$)] for both the films. These magnetic moments have been derived by using the XMCD spin sum rule [55] to the experimental

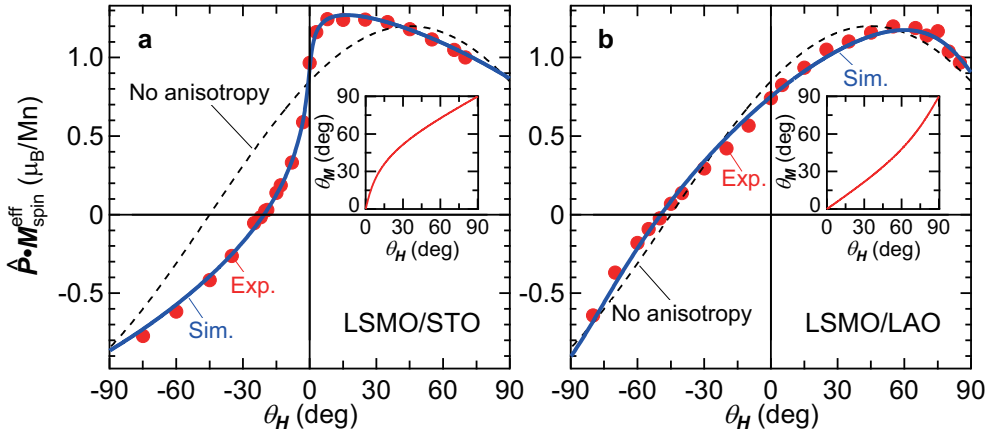

Figure 6.8: $\theta_{\boldsymbol{H}}$-dependence of the effective spin magnetic moment projected onto the incident x rays, $\hat{\boldsymbol{P}} \cdot \boldsymbol{M}^{\rm eff}_{\rm spin}$ ($\sim \hat{\boldsymbol{P}} \cdot \boldsymbol{M}_{\rm spin}$). Panels (a) and (b) are the data for the LSMO thin films grown on the STO and LAO substrates, respectively. Red circles: Projected effective spin magnetic moment $\hat{\boldsymbol{P}} \cdot \boldsymbol{M}^{\rm eff}_{\rm spin}$ deduced from experimental XMCD spectra by using the XMCD spin sum rule [55]. Black dashed curve: Angular dependence of $\hat{\boldsymbol{P}} \cdot \boldsymbol{M}^{\rm eff}_{\rm spin}$ in the absence of magnetic anisotropy. Blue solid curve: Simulated angular dependence of $\hat{\boldsymbol{P}} \cdot \boldsymbol{M}^{\rm eff}_{\rm spin}$ by incorporating the shape magnetic anisotropy and magnetocrystalline anisotropy (MCA). Insets show the relationship between $\theta_{\boldsymbol{M}}$ and $\theta_{\boldsymbol{H}}$ deduced from the simulation. The experimental geometry is shown in Fig. 6.4.

spectra in Figs. 6.5(c) and 6.5(d). The experimental angular dependencies, indicated by the red circles, are deviated from the sinusoidal curve indicated by the black dashed curves, which assume no magnetic anisotropy ($\theta_{\boldsymbol{H}} = \theta_{\boldsymbol{M}}$). This suggests that the effect of magnetic anisotropy has to be incorporated in order to reproduce the experimental angular dependencies. Here the Stoner-Wohlfarth model [88] has been adopted in order to simulate the obtained angular dependence. Details of the simulation methods are summarized in Sec. 4.3.2. In the Stoner-Wohlfarth model, it is assumed that the sample has a single magnetic domain and that it exhibits uniaxial magnetic anisotropy of the lowest order (proportional to $\cos^2\theta_{\boldsymbol{M}}$). The static magnetic energy per volume E can be then written by an expression using $\theta_{\boldsymbol{M}}$, $\theta_{\boldsymbol{H}}$, and other variables. By minimizing E with respect to $\theta_{\boldsymbol{M}}$ for each $\theta_{\boldsymbol{H}}$, one can determine the direction of the magnetization $\theta_{\boldsymbol{M}}$ as a function of the field direction $\theta_{\boldsymbol{H}}$, and the projected magnetic moment can be calculated by using the deduced $\theta_{\boldsymbol{M}}$. In addition, the uniaxial magnetocrystalline anisotropy (MCA) constant K_u, the saturation magnetization $M_{\rm sat}$, and the electric quadrupole moment $\langle Q_{zz} \rangle \equiv \langle 1 - 3\hat{z}^2 \rangle$ can be also

Table 6.2: Best-fit parameter values determined from the simulation in Fig. 6.8. Errors have been determined using the least squares method. Note that K_u denotes the MCA constant without the contribution of shape magnetic anisotropy.

Substrate	$M_{\rm sat}$ ($\mu_{\rm B}$/Mn)	K_u (kJ/m^3)	$(7/2)\langle Q_{zz}\rangle$
STO	1.255 ± 0.007	-37.2 ± 0.8	$+0.05 \pm 0.01$
LAO	1.206 ± 0.014	$+40.4 \pm 2.4$	-0.12 ± 0.02

deduced by taking these variables as fitting parameters and optimizing the simulation to the experimental angular dependencies (see Sec. 3.2.3 for the interpretation of Q_{zz}). The results of the simulations are shown in Figs. 6.8 by the blue solid curves, which well reproduces the experimental angular dependencies. The best-fit parameter values of K_u, $M_{\rm sat}$, and $\langle Q_{zz}\rangle$ are listed in Table 6.2. The MCA constant K_u in Table 6.2 ($K_u > 0$ corresponding to out-of-plane easy axis) suggests that the LSMO thin film on the STO (LAO) substrates favors in-plane (out-of-plane) magnetization due to MCA, which is consistent with the magnetization data in the present (Fig. 6.2) and previous studies [46, 47]. One can also see from Table 6.2 that the electric quadrupole moment $\langle Q_{zz}\rangle = \langle 1 - 3\hat{z}^2\rangle$ is positive (negative) for the STO (LAO) substrate. As can be seen from the first column of Fig. 1 in Ref. [2], $(7/2)\langle Q_{zz}\rangle$ is equal to $+2$ for the pure $d_{x^2-y^2}$ orbital and is equal to -2 for the pure $d_{3z^2-r^2}$ orbital. Thus, the positive (negative) $\langle Q_{zz}\rangle$ for the STO (LAO) substrate implies that the $x^2 - y^2$ ($3z^2 - r^2$) majority-spin band is more preferentially occupied in the case of the STO (LAO) substrate. This further supports the result of TXMCD that the spin-density distribution is anisotropic in the strained LSMO films. The degrees of the preferential orbital polarization $|(7/2)\langle Q_{zz}\rangle/2|$ are estimated to be $\sim 2.5\%$ and $\sim 6\%$ for LSMO/STO and LSMO/LAO, respectively.

The present method for deducing the magnetic anisotropy constant using the field-angle-dependent XMCD has an advantage that one can suppress the extrinsic changes of the spectral line shapes due to the saturation effect [105], since the incident angle of the x rays ($\theta_{\rm inc}$) is fixed. Moreover, the present method can be also utilized for dilute magnetic systems, such as lightly-doped magnetic semiconductors and ultrathin films with thicknesses of a few atomic layers. Since the conventional magnetometry is difficult to apply for these systems, the present method will offer the possibility to deduce the magnetic anisotropy constants of these magnetic systems with higher accuracy.

6.4 Discussion

6.4.1 Relationship between the magnetic anisotropy and $\boldsymbol{M}_{\mathrm{T}}$

The present results suggest a close relationship between the magnetic anisotropy and the anisotropic spin-density distribution $\boldsymbol{M}_{\mathrm{T}}$ of the LSMO thin films. As explained in Sec. 3.2.4, the uniaxial MAE of ferromagnets can be in general written as Eq. (3.12), which has been derived by Wang *et al.* based on the perturbation theory of SOI [58] and has been summarized by van der Laan [59]. The equation dictates that both the anisotropy of the orbital magnetic moment M_{orb} and the anisotropy of M_{T} contribute to the MAE. When the anisotropy of spin-density distribution is negligible (as in bulk single crystals with cubic symmetry), more simplified equation derived by Bruno [Eq. (3.10)] is applicable, in which only the anisotropy of M_{orb} is considered [57]. In the present case, assuming that $\zeta \sim 30$ meV and $\Delta E_{\mathrm{ex}} \sim 5$ eV, one can approximately estimate the contribution of M_{T} to the MAE to be ~ -0.01 meV/Mn ($+0.03$ meV/Mn) or ~ -30 kJ/m^3 ($+80$ kJ/m^3) for the STO (LAO) substrate. The estimated anisotropy energies are consistent with the K_u values in Table 6.2 in signs and are comparable in magnitudes. This estimation suggests that the magnetic dipole M_{T} (i.e., anisotropic spin-density distribution) has a non-negligible contribution to the strain-induced MAE in the LSMO thin films, although more precise measurements of M_{orb} is required in order to evaluate the relative contributions of the M_{orb}- and M_{T}- terms more quantitatively.

6.4.2 Comparison with XLD

The deduced spin-density anisotropy in the studied LSMO thin films (x^2-y^2-like for the STO substrate and $3z^2-r^2$-like for the LAO substrate) is consistent with the preferential orbital occupation expected from the sign of the epitaxial strain. It is also consistent with the preferential orbital occupation which has been predicted from the transport and magnetization data, and the first-principles calculation [19]. In contrast, the XLD spectroscopy has shown that the $d_{3z^2-r^2}$ orbital is more preferentially occupied than the $d_{x^2-y^2}$ orbital even in the case of tensile STO substrate [49], which has been ascribed to the symmetry breaking at the surface and interface of the films [50, 51]. The reason for these apparently different results between the present angle-dependent XMCD and previous XLD measurements, may become clear if one notices that XMCD is sensitive only to the *spin-polarized* electrons whereas XLD is sensitive to *all* the d electrons. As shown in Fig.

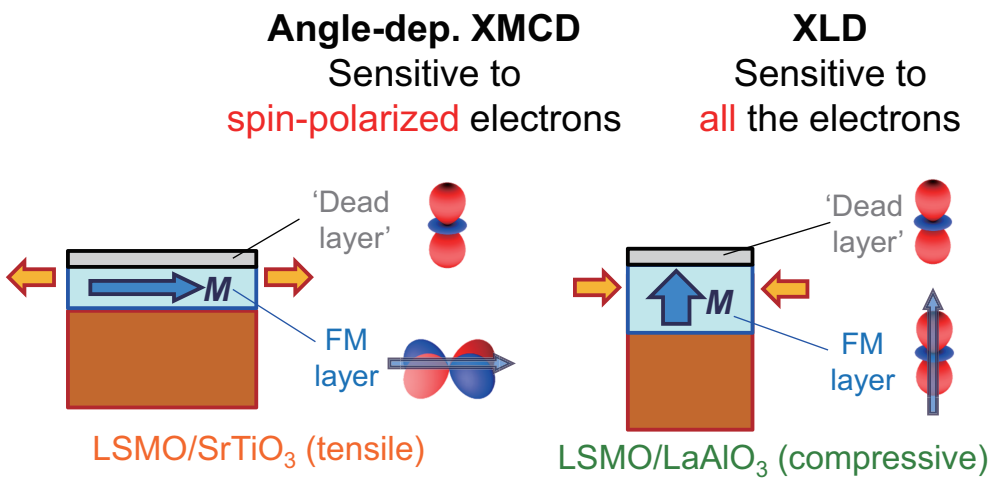

Figure 6.9: Schematic illustration of the preferential orbital occupation deduced from the comparison between the present angle-dependent XMCD result and the previous XLD results [49–51]. It is assumed that there is a magnetically dead layer at the surface of the film, in which the $3z^2-r^2$ orbital is preferentially occupied due to the symmetry-breaking effect [50, 51].

6.9, if most of the surface Mn atoms occupies the $d_{3z^2-r^2}$ orbital due to the symmetry breaking, both the $d_{3z^2-r^2\uparrow}$ (majority-spin band) and the $d_{3z^2-r^2\downarrow}$ (minority-spin band) levels are occupied and the Mn atoms are less spin-polarized at the surface. Thus, the $3z^2 - r^2$-like *charge*-density distribution (without spin polarization) at the surface and interface is detected by XLD, while the $x^2 - y^2$-like *spin*-density distribution in the bulk layers is detected by angle-dependent XMCD, Indeed, many studies have indicated the presence of magnetic dead layers at the surface or the interface of the manganite thin films [35, 115]. The results of the present angle-dependent XMCD and TXMCD studies, therefore, suggest a close relationship between the reported magnetic dead layer of LSMO thin films and the preferential occupation of the $3z^2-r^2$ orbital at the surface. In order to test this hypothesis, further experiments will be necessary such as XLD measurements in the fluorescence-yield mode, in which similar orbital polarization as the present study is expected due to much longer penetration depth of the fluorescence-yield mode than the electron-yield mode.

6.5 Conclusion

In this chapter, magnetic anisotropy and spatial distribution (i.e. the orbital occupation) of spin-polarized electrons in LSMO thin films under tensile

or compressive strain have been investigated via angle-dependent XMCD. It has been found by extracting the magnetic dipole $\boldsymbol{M}_{\mathrm{T}}$ that the spatial distribution of the spin density is $x^2 - y^2$-like in the case of tensile strain (STO substrate) and $3z^2 - r^2$-like in the case of compressive strain (LAO substrate). This result implies a close connection between the magnetic anisotropy and the spin-density distribution in strained LSMO thin films. The apparent discrepancy of the present result with the orbital occupation observed by XLD (i.e., $3z^2 - r^2$-like orbitals for both the substrates), can be explained by assuming that both the $3z^2 - r^2 \uparrow$ and the $3z^2 - r^2 \downarrow$ are preferentially occupied at the surface of the film, which may be a possible origin for the surface magnetic dead layer.

Chapter 7

Anisotropic charge distribution induced by spin polarization in $La_{0.6}Sr_{0.4}MnO_3$ thin films studied by x-ray magnetic linear dichroism

Part of this chapter has been published in "Anisotropic Charge Distribution Induced by Spin Polarization in $La_{0.6}Sr_{0.4}MnO_3$ Thin Films Studied by X-ray Magnetic Linear Dichroism", G. Shibata, K. Yoshimatsu, K. Ishigami, T. Harano, Y. Takahashi, S. Sakamoto, Y. Nonaka, T. Kadono, M. Furuse, S. Fuchino, M. Okano, J.-i. Fujihira, A. Uchida, K. Watanabe, H. Fujihira, S. Fujihira, A. Tanaka, H. Kumigashira, T. Koide, and A. Fujimori, J. Phys. Soc. Jpn. **87**, 114713 (2018).

7.1 Introduction

Magnetic anisotropy of ferromagnetic thin films and multilayers has been intensively studied so far both from technological and scientific interests [1]. From the technological point of view, materials with large magnetic anisotropy are desired for the realization of permanent magnets with higher coercive fields, magnetic recording media with higher density, and various spintronics devices. From the scientific point of view, clarifying the microscopic origin of magnetic anisotropy has been a challenging problem. Although it has been well established that magnetic anisotropy arises as a combined effect of the anisotropy of electronic states and spin-orbit interaction (SOI), consensus has not been reached yet regarding the detailed

mechanism for it. In his seminal paper, Bruno [57] has shown by the perturbative treatment of SOI that the magnetocrystalline anisotropy (MCA) energy is proportional to the anisotropy of the orbital magnetic moment (M_{orb}), suggesting that the orbital-moment anisotropy (OMA) is the primary origin for MCA. Wang *et al.* [58] have extended Bruno's theory, by incorpolating the 'spin-flip' term in addition to the 'spin-conservation' term, that the anisotropy of spin-density distribution, represented by 'magnetic dipole' M_{T} [2, 55], also contributes to the MCA [59]. The theories by Bruno and Wang *et al.* have been summarized by van der Laan [59] in a more concise form. Several theoretical studies have predicted that the magnetic dipole M_{T} may make a larger contribution to the MCA energy than the OMA [64–66]. As discussed in the previous chapter, the angle-dependent x-ray magnetic circular dichroism (XMCD) study show that the anisotropy of spin-density distribution M_{T} is associated with MCA [21]. Other XMCD studies also point out the close relationship between M_{T} and MCA [116]. These studies suggests that the charge-density anisotropy can also affect the preferential orientation of spin magnetic moments.

Since the electron orbitals and spins are coupled with each other through SOI, it is also expected, as an inverse process of the abovementioned process leading to MCA, that one can magnetically induce the OMA and anisotropic charge distribution by aligning the electron spin magnetic moments. X-ray linear dichroism (XLD) in core-level x-ray absorption spectroscopy (XAS) is a spectroscopic method which can probe the anisotropic charge distribution by measuring the differences in the XAS spectra between the two orthogonal linear polarizations. It is particularly called x-ray magnetic linear dichroism (XMLD) if the anisotropic charge distribution is magnetically induced. XMLD has been utilized for various magnetic thin films and multilayers in order to clarify the relationship between the electron spins and orbitals [117–124], especially for systems which exhibit perpendicular magnetic anisotropy [119, 123] and exchange bias [122]. As for the thin films of ferromagnetic manganites such as $La_{1-x}Sr_xMnO_3$ (LSMO), the anisotropy of charge distribution between the out-of-plane and in-plane directions has been investigated via XLD [48–51] and XMLD [50]. However, the charge anisotropy within the film plane has not been investigated in these studies.

In the present chapter, an XMLD study on the ferromagnetic LSMO ($x = 0.4$) thin films shall be presented in order to discuss the relationship between the electron spins and charge anisotropy.

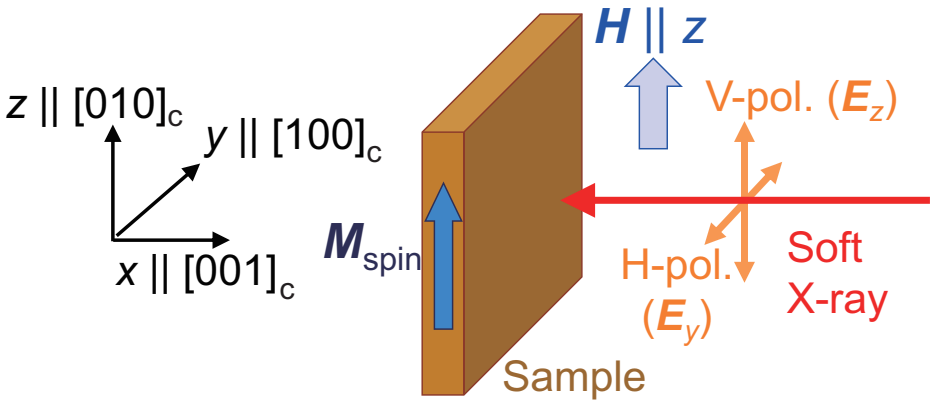

Figure 7.1: Schematic description of the experimental geometry of the present x-ray magnetic linear dichroism (XMLD) study.

7.2 Methods

LSMO ($x = 0.4$) thin films were grown on $SrTiO_3$ (STO) (001) substrates by the laser molecular beam epitaxy method [91]. Due to the difference in the lattice constants between LSMO ($a = 0.384$ nm) and STO ($a = 0.3905$ nm), the LSMO films undergo tensile strain from the STO substrates [19]. The growth conditions of the films were essentially the same as that described in Chap. 5. The thicknesses of the LSMO films were between 2 and 15 unit cell (UC). The films were capped with 1 UC of $La_{0.6}Sr_{0.4}TiO_3$ and subsequently-deposited 2 UC of STO (see Fig. 5.1). The films were annealed in O_2 atmosphere in order to fill the oxygen vacancies after the deposition.

Figure 7.1 schematically describes the experimental geometry of XMLD. The x rays were incident on the sample normal to the film ($[001]_c$ direction, where the subscript 'c' denotes that the indices are written in terms of the pseudocubic unit cell). The polarization of the x rays was either horizontal (denoted by H) or vertical (denoted by V). The films were mounted on the sample holder so that the in-plane $[100]_c$ direction was horizontal and the $[010]_c$ direction was vertical. A magnetic field $\boldsymbol{H}$ of $\mu_0 H = 0.1$ T (which was enough to saturate the magnetization along the in-plane direction) was applied along the vertical ($[010]_c$) direction, using the vector-XMCD apparatus [4, 21]. This means that the V and H polarizations correspond to the electic field vector of the x rays ($\boldsymbol{E}$) parallel and perpendicular to the spin magnetic moment $\boldsymbol{M}_{\rm spin}$, respectively. In the present article, the in-plane $[010]_c$ direction (i.e., the direction of the $\boldsymbol{M}_{\rm spin}$) is chosen to be the z-axis, following the definition in Refs. 68, 69. The x-axis is chosen to be the sample-normal ($[001]_c$) direction (i.e., opposite to the wavevector of the incident x rays) and y-axis to be the $[100]_c$ direction (i.e., the in-plane di-

rection perpendicular to $\boldsymbol{M}_{\mathrm{spin}}$). In the present study, XMLD is defined as XAS (V) − XAS (H).

The XMLD experiments were performed at the beamline BL-16A2 of KEK Photon Factory (KEK-PF) installed with a twin Apple II-type undulator. The measurement temperature T was 30 K. The spectra were measured in the total electron-yield (TEY) mode. The base pressure of the measurement chamber was $\sim 1 \times 10^{-9}$ Torr. The obtained XAS and XMLD spectra were analyzed with the cluster-model calculation using the 'Xtls' code (version 8.5) [72]. Details of the calculation methods are described in Secs. 3.4 and 6.3.2.

7.3 Results and Discussion

Figure 7.2(a) shows the Mn $L_{2,3}$-edge XAS spectra of the LSMO thin films averaged over both the H and V polarizations. In the raw spectra, XAS signals originating from Mn^{2+} overlap, as shown by dotted curves in Fig. 7.2(a). Such XAS signals of Mn^{2+} are occasionally observed in manganite thin films due to extrinsic effects such as oxygen reduction at the surface [45]. These extrinsic Mn^{2+} signals have been subtracted following the method presented in the previous study [98]. This affects the absolute values of the XMLD intensities by $\sim 10\%$ at most, but does not change our main conclusion. After having subtracted the Mn^{2+} signals, the spectral line shapes are almost identical to those in previous studies [21, 48–51, 92, 114]. The peak positions of the spectra are shifted to lower photon energies with decreasing thickness, indicating that the valence of Mn gradually decreases. This is the same tendency as the XMCD study (see Chap. 5), which may be due to electron doping at the interfaces from the substrates and/or from oxygen vacancies. Figure 7.2(b) shows the XMLD spectra of the LSMO thin films with various thicknesses. The XMLD intensity gradually decreases as the thickness of LSMO is reduced, while the spectral line shape of XMLD is essentially unchanged. Here, the XMLD intensity is defined as the difference between the signal intensities at 641.1 eV and at 643.1 eV (which are the peak and the dip positions of the XMLD spectra for the 15 UC film, respectively), as shown in Fig. 7.2(b). Note that this definition has been adopted because it is less affected by the procedure of the background subtraction compared to the spectral areas of XMLD. In Fig. 7.2(c), thus estimated XMLD intensities are plotted against the square of the ferromagnetic (FM) moment M^2_{ferro}, which has been estimated from the magnetization curves measured by XMCD [114]. The plot clearly shows that the XMLD intensity is proportional to M^2_{ferro}. In general, the XMLD intensity is proportional to the

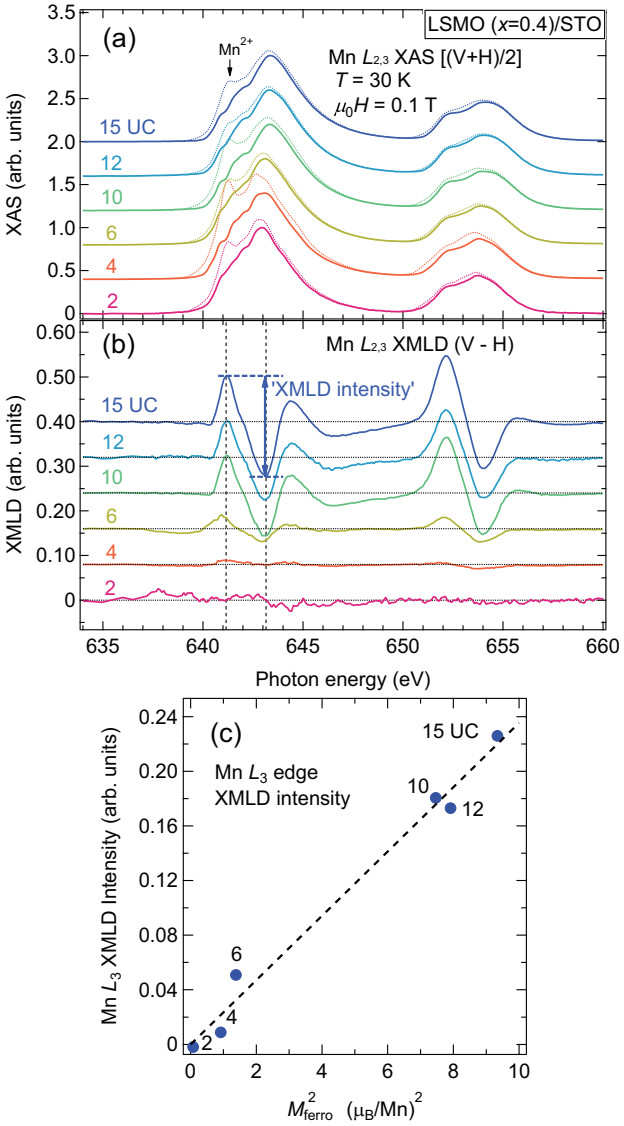

Figure 7.2: XMLD on $La_{1-x}Sr_xMnO_3$ (LSMO) thin films grown on $SrTiO_3$ (STO) (001) substrates with various thicknesses. (a) X-ray absorption spectroscopy (XAS) spectra at the Mn $L_{2,3}$ absorption edge averaged over both the polarizations. Dashed curves are the raw spectra and solid curves are the spectra after subtracting the extrinsic signals of Mn^{2+} (see text). (b) XMLD spectra at the Mn-$L_{2,3}$ absorption edge measured at $\mu_0 H = 0.1$ T. XMLD is defined as XAS(V)−XAS(H), where V and H, respectively, denote the vertical and horizontal linear polarization (i.e., $\boldsymbol{E} \parallel \boldsymbol{M}_{\rm spin}$ and $\boldsymbol{E} \perp \boldsymbol{M}_{\rm spin}$). The definition of the XMLD intensity is shown by an arrow. (c) XMLD intensities of LSMO/STO thin films with various thicknesses plotted as a function of ferromagnetic moment $M^2_{\rm ferro}$ deduced from x-ray magnetic circular dichroism (XMCD) [114]. Dashed line shows the result of a least-square fitting with a linear function, in which the constant term has been fixed to zero.

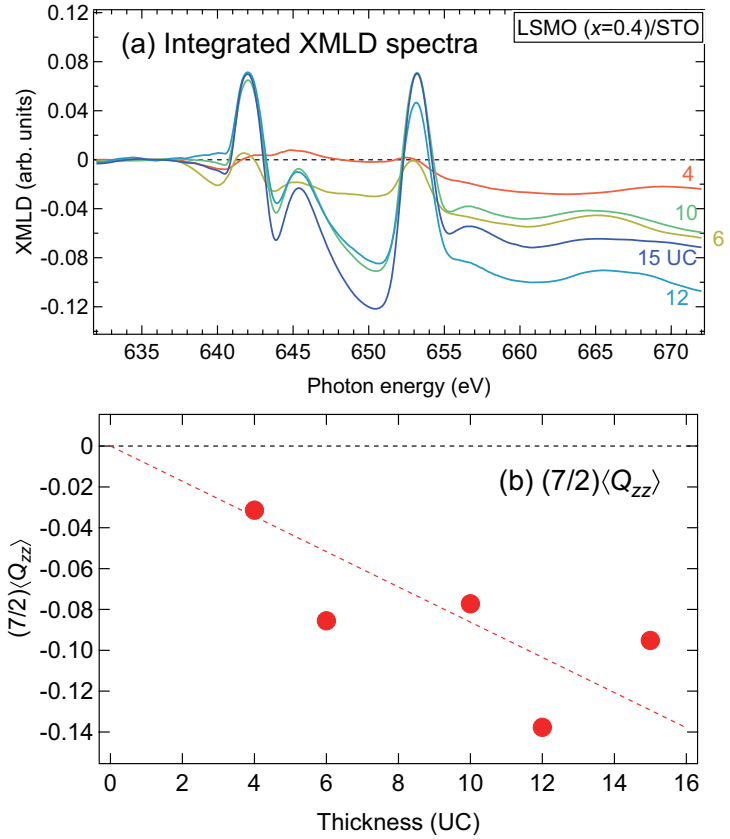

Figure 7.3: Estimation of charge-distribution anisotropy from the integrals of XMLD. (a) Integrals of the XMLD spectra shown in Fig. 7.2(b). (b) Electric quadrupole moment $(7/2)\langle Q_{zz}\rangle$ deduced from the integral of the XMLD spectra over the Mn $L_{2,3}$ edge. Data for 2 UC have been omitted because the XMLD signal was within the noise level. Dashed line shows the result of a least-square fitting with a linear function, in which the constant term has been fixed to zero.

square of the local spin magnetic moment [68]. The above result suggests that the XMLD signals originate from the FM phases rather than the antiferromagnetic (AFM) phases, which was possibly present in the sample as an impurity phase.

According to the sum rule for XLD [69], the integral of the XMLD spectra over the L_3 and L_2 absorption edges gives the electric quadrupole moment $\langle Q_{zz}\rangle = \langle 1 - 3z^2/r^2\rangle$, namely, the anisotropy of the charge distribution. Figure 7.3(a) shows the integrated XMLD spectra calculated from Fig. 7.2(b), and the values of $(7/2)\langle Q_{zz}\rangle$ deduced from them are shown in Fig. 7.3(b) as a function of thickness. Note that $(7/2)\langle Q_{zz}\rangle$ is equal to $+2$ (-2) for the $d_{x^2-y^2}$ ($d_{3z^2-r^2}$) orbital [2]. The values of $\langle Q_{zz}\rangle$ are negative for

all the thicknesses and the absolute values of $\langle Q_{zz} \rangle$ gradually increases with thickness, as the films turn from the paramagnetic into the ferromagnetic states. Without the spin magnetic moment $\boldsymbol{M}_{\rm spin}$, the electron distribution should be isotropic between the in-plane y- and z-directions because the films have a tetragonal crystal symmetry. The negative values of $\langle Q_{zz} \rangle$ $(= \langle 1 - 3z^2/r^2 \rangle)$ shows that the electrons are more densely distributed along the z-directions than the y-direction due to the presence of $\boldsymbol{M}_{\rm spin}$, namely, the electron orbitals are 'elongated' along the spin direction through SOI. The observed charge-density anisotropy $(7/2)\langle Q_{zz} \rangle \sim -0.1$ corresponds to the preferential occupation of the $d_{3z^2-r^2}$ orbital by $\sim 10\%$ compared to the $d_{x^2-y^2}$ orbital.

In Fig. 7.4(a), the experimentally obtained XMLD spectrum (for 15 UC) is compared with the theoretical ones calculated using the MnO_6 cluster model with octahedral (O_h) or tetragonal (D_{4h}) symmetry with respect to the out-of-plane (x) axis. For the simulation with D_{4h} symmetry, the in-plane $y^2 - z^2$ orbital has a lower energy than the out-of-plane $3x^2 - r^2$ orbital by 0.08 eV in order to simulate the tensile epitaxial strain. The parameter values used for the simulations are chosen to be the same as those in Table 6.1 in the previous chapter. In order to see the effects of SOI, the XMLD spectra in both the cases with and without SOI of Mn $3d$ electrons have been calculated. Comparing the calculated spectra with the experimental one, it can be seen that the calculation with D_{4h} symmetry under tensile strain is closer to the experimental spectra than that with O_h symmetry, especially for the spectral line shapes at the Mn L_2 edge. This is consistent with the tensile epitaxial strain from the STO substrate. Furthermore, as shown in Fig. 7.4(b), the integrals of the simulated XMLD spectra over the Mn L_3 and L_2 edges become negative in the presence of SOI of Mn $3d$ electrons, while they are equal to zero in the absence of SOI for both the crystal symmetries. The negative XMLD integrals suggest that $\langle Q_{zz} \rangle < 0$, namely, the charge density is higher along the z-direction than the y-direction, which is again consistent with the experiment. These simulations also demonstrate that SOI of Mn $3d$ electrons is indispensable for the experimentally observed charge-density anisotropy within the plane.

The present result illustrates that the charge distribution of Mn $3d$ electrons is elongated along the spin direction. This means that the state in which the electron orbitals are elongated along the spins is more energetically favorable. This observation may be related to the strain-induced magnetic anisotropy in manganite thin films which has been previously reported [46, 47]. It is known that the magnetic easy directions of LSMO thin films are out-of-plane in the case of compressive strain and in-plane in the case of tensile strain [46, 47]. As seen in the previous chapter, the

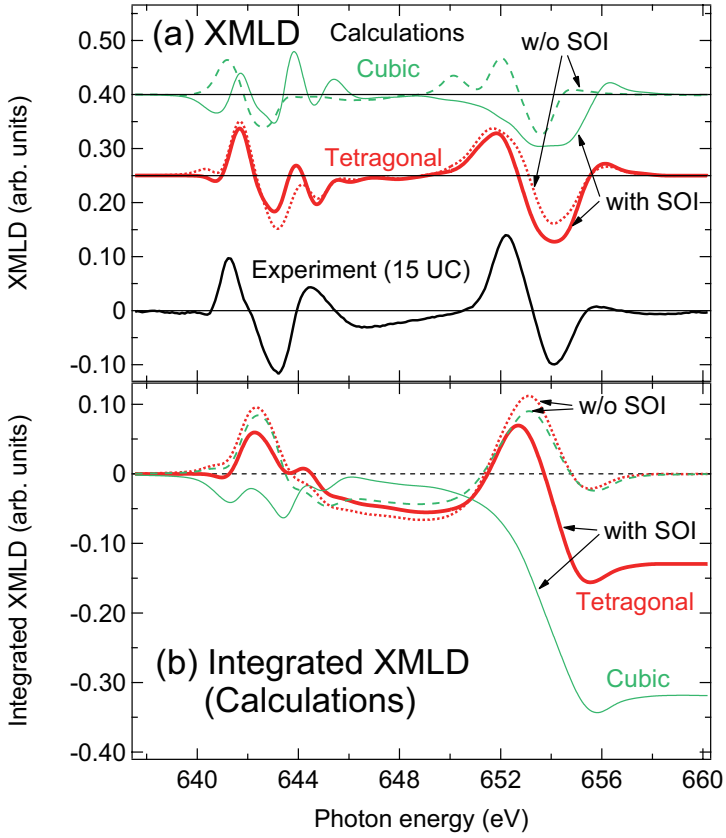

Figure 7.4: (a) Simulated XMLD spectra using the MnO_6 cluster model. (b) Integrals of the simulated XMLD spectra in (a). In both panels, solid and dashed curves represent the simulated spectra with and without Mn 3*d* spin-orbit interaction (SOI), respectively, and green and red curves represent the simulated spectra assuming the octahedral (O_h) and tetragonally (D_{4h})-tensiled crystal symmetry, respectively. Black solid curve at the bottom of Panel (a) shows the experimental XMLD spectrum for the LSMO thin film of 15 UC thickness.

charge density of spin-polarized Mn 3*d* electrons under the compressive and tensile strain is shown to be higher along the out-of-plane and in-plane directions, respectively. Therefore, it follows that LSMO thin films tend to be magnetized parallel to the directions along which the Mn 3*d* orbitals are elongated, the same tendency as the present XMLD result. The present study corroborates that the strain-induced magnetic anisotropy in LSMO thin films originates from the combining effect of SOI and the charge-density anisotropy of spin-polarized Mn 3*d* electrons. The magnetic anisotropy and the charge anisotropy are related with each other in two ways: One is that the charge anisotropy of spin-polarized electrons yields finite magnetic dipole

M_{T}, resulting in finite MCA energy through the spin-flip term in perturbation theory with respect to SOI by Wang *et al.* [58, 59]. The other is that the OMA contributes to the MCA energy through Bruno's spin-conservation term [57, 59] and that the observed charge anisotropy is indirectly induced by the OMA. In order to see which of the magnetic dipole M_{T} and the OMA plays a more important role in the MCA of LSMO thin films, further experimental and theoretical studies are needed.

It is also worthwhile to discuss how the magnetically induced charge-density anisotropy studied here and the strain-induced charge-density anisotropy studied previously (Chap. 6 and Ref. [21]) are related with each other. In the previous angle-dependent study, it has been assumed that the electric quadrupole tensor $\langle Q_{zz} \rangle$ is constant as a function of magnetization direction ($\theta_{\boldsymbol{M}}$), namely, the magnetically induced change of the charge density studied here has not been taken into account. A remedy for this problem is to assume that only the in-plane charge anisotropy is significantly affected by the magnetization direction, while the strain-induced charge-density anisotropy along the out-of-plane direction is less affected. In other words, it is assumed that the electric quadrupole tensor along the out-of-plane (z) direction $\langle Q_{zz} \rangle$ induced by the epitaxial strain is nearly independent of $\theta_{\boldsymbol{M}}$, and that the in-plane (xy) charge-density anisotropy observed by XMLD is induced by the difference between $\langle Q_{xx} \rangle$ and $\langle Q_{yy} \rangle$ (note that the coordination system used in Chap. 6 has been adopted here). This can explain both the results of XMLD and angle-dependent XMCD consistently. More XMLD measurements at various sample and magnetic field angles may be helpful in order to test this hypothesis.

7.4 Conclusion

In this chapter, the magnetically-induced anisotropic charge distribution in the LSMO ($x = 0.4$)/STO (001) thin films has been studied via XMLD. From the thickness dependence of the XMLD spectra, it has been shown that the XMLD intensity is proportional to the square of the FM moment of the film, suggesting that the XMLD signals originate from the FM phase in the LSMO thin films rather than the possible AFM impurity phase. The electric quadrupolar moment $\langle Q_{zz} \rangle$, which represents the anisotropy of the charge distribution, is shown to be negative, indicating that the in-plane $(y^2 - z^2)$ orbital of the Mn $3d$ electrons is slightly elongated along the direction of the spins. This is consistent with the theoretical prediction based on the MnO_6 cluster model with tensile strain and with SOI. The observed charge anisotropy, i.e., the elongation of the electron orbital along the spin direction,

may be related to the strain-induced magnetic anisotropy in LSMO thin films.

Chapter 8

Summary and outlook

In the present thesis, I have presented the soft x-ray spectroscopy studies of ferromagnetic metallic $La_{1-x}Sr_xMnO_3$ (LSMO) thin films, which have the highest Curie temperature above the room temperature among the perovskite manganites, in order to clarify the relationship between their electronic structures and the magnetic properties.

First, the electronic structures and magnetic properties of the LSMO ($x = 0.4$) thin films grown on the $SrTiO_3$ (STO) (001) substrates and their thickness dependencies have been studied using x-ray absorption spectroscopy (XAS) and x-ray magnetic circular dichroism (XMCD) spectroscopy in order to clarify the mechanism of the thickness-dependent MIT in LSMO thin films from the microscopic point of view. From the thickness dependence of XAS spectra, it has been shown that the Mn valence are shifted from the bulk value ($Mn^{3.4+}$) towards the lower side (Mn^{3+}) accompanying the MIT. This valence shift is considered to be induced by the interfacial electron doping from the substrate and the cap layer, and/or the possible presence of the oxygen vacancies. It has also been found from the magnetization curves measured by XMCD that the transition from the FM to the PM phases occurs more *gradually* than the MIT with decreasing thickness. This difference of the thickness dependencies between the MIT and the magnetic transitions can be explained based on the phase-separation model between the FM-M and PM-insulating phases.

Second, the angle-dependent XMCD study on the ferromagnetic LSMO ($x = 0.3$) thin films grown on the tensile STO (001) and compressive $LaAlO_3$ (LAO) (001) substrates has been presented, which has become possible using the newly-developed 'vector-magnet' XMCD measurement system. The aim of this study is to reveal the relationship between the epitaxial strain and the magnetic anisotropy of the films in terms of the electronic structure. From the angular dependencies of the XMCD intensity, it has been demon-

strated that the LSMO thin film grown on the STO (LAO) substrate has the in-plane (out-of-plane) magnetic easy axis, as previously reported [46, 47]. Besides, the magnetic dipole $\boldsymbol{M}_{\mathrm{T}}$ of Mn, which represents the anisotropy of the spin-density distribution (i.e., the preferential orbital occupation of the spin-polarized electrons), has been extracted using the transverse XMCD (TXMCD) method. The extracted $\boldsymbol{M}_{\mathrm{T}}$ suggests that the spin-density distribution is more x^2-y^2-like for the LSMO/STO film and more $3z^2-r^2$-like for the LSMO/LAO film, consistent with the signs of the epitaxial strain. By comparing the present result of angle-dependent XMCD (sensitive to *spin-polarized* electrons) with previous x-ray linear dichroism (XLD) results (sensitive to *all* the electrons), it is indicated that the surface Mn atoms is magnetically inactive, probably due to the preferential orbital occupation of the $3z^2-r^2\uparrow$ and $3z^2-r^2\downarrow$ orbitals.

Third, the charge-density anisotropy of Mn induced by the spins in LSMO ($x = 0.4$)/STO (001) thin films has been investigated by means of x-ray magnetic linear dichroism (XMLD), which has also become possible by using of the vector-magnet apparatus. The electric quadrupole moment $\langle Q_{zz}\rangle = \langle 1-3\hat{z}^2\rangle$, which represents the charge anisotropy with respect to the spin direction (z-axis), is shown to be negative from the XLD sum rule [69]. This indicates that the in-plane electron orbitals of Mn are elongated along the direction of the spin polarization due to SOI, despite the tetragonal crystal symmetry around the sample-normal direction. The observed charge anisotropy induced by the spin polarization can be understood as an inverse process of the strain-induced magnetic anisotropy addressed in the angle-dependent XMCD study.

To summarize, the present studies have given new insights into the relationship between the electronic structure and the magnetic properties of manganite thin films by the soft x-ray spectroscopy. There are still many remaining problems to be solved in the future in order to fully elucidate the origin of the magnetic properties of them from the microscopic point of view. As for the thickness dependent MITs and magnetic transitions, it is still necessary to clarify which of the interfacial carrier doping from the substrate or from the off-stoichiometry governs more significantly the critical thickness and the magnetic Curie temperature. Systematic spectrocsopic studies on manganite thin films with various growth conditions and various interfacial stacking structures may be the key to the solution. In addition, the role of the crystal structures on the electric and magnetic properties have to be examined more directly by other spectroscopic methods, such as resonant soft-x-ray scattering (RSXS) or extended x-ray absorption fine structure (EXAFS). It might be also useful to re-examine the bandwidth-narrowing effect induced by dimensionality using resonant inelastic x-ray scattering

(RIXS) spectroscopy. These will give important clues for the realization of manganite-based spintronics devices, such as magnetic tunneling junctions (MTJs) and spin filters, with better device properties at room temperature.

There have also been remaining issues about the origin of the magnetic anisotropy in ferromagnetic thin films and multilayers. Although a number of experimental and theoretical studies have been done on the magnetic anisotropy in various thin films and multilayers, consensus has not been reached on which of the orbital-moment anisotropy ($\Delta M_{\rm orb}$) [the first term of Eq. (1.4)] or the spin-density anisotropy ($\Delta M_{\rm T}$) [the second term of Eq. (1.4)] is the primary origin of the magnetic anisotropy energy in each material. This is partly because the direct measurement of the magnetic dipole $M_{\rm T}$ is difficult in conventional XMCD measurement systems and we just had to rely on the measurement of the orbital moment anisotropy $\Delta M_{\rm orb}$. The angle-dependent XMCD and TXMCD methods developed in the present study enable us to directly observe $M_{\rm T}$, which is essential to discuss the relationship between the magnetic anisotropy and the microscopic electronic structure. Applying these methods to other magnetic systems with large perpendicular magnetic anisotropy, such as $L1_0$-type alloys like FePt and cobalt ferrite $CoFe_2O_4$, would be benefitical in order to find out why the magnetic anisotropy is enhanced in these materials and how one can design magnetic materials which have large magnetic anisotropy. In magnetic heterostructures, coupling between ferromagnetic and neighboring paramagnetic/antiferromagnetic layers significantly affects the magnetic properties of the entire film. The observation of the charge-density anisotropy by XMLD in both the ferromagnetic and antiferromagnetic layers may be useful in order to discuss the origin of the novel magnetic properties in magnetic multilayers from the microscopic point of view.

I hope that the present study will be the starting for our deeper understanding of the origins of the magnetic properties of ultrathin films, particularly of magnetic anisotropy in a wide variety of ferromagnetic thin films and multilayers in the future.

Acknowledgments

It is my great pleasure to express my sincere gratitude to all the people who have helped with my study.

First of all, I would like to express my deepest gratitude to Prof. Atsushi Fujimori, who has guided me into this research field of strongly-correlated electron systems. His insightful advice and enlightening discussion with him have always led me to the correct direction throughout the whole research project. The present study would not have been completed without his excellent guidance. I cannot thank enough for his continuous supports in all ways for years. I would also like to cordially appreciate Prof. Teppei Yoshida and Prof. Kozo Okazaki, who were the assistant professors of Fujimori Group during my Ph. D. course, for their kindful help throughout my research life.

I would like to acknowledge Dr. Kohei Yoshimatsu, Dr. Miho Kitamura, Dr. Enju Sakai, Dr. Makoto Minohara, Prof. Hiroshi Kumigashira, and Prof. Masaharu Oshima at KEK-PF, who have provided me with high-quality $La_{1-x}Sr_xMnO_3$ (LSMO) thin films for my whole research project. I would also like to appreciate Dr. Akihito Sawa regarding the annealing of the LSMO thin films. The present research would not have been possible without their countinuous supports.

I owe much for the design and construction of the vector-magnet apparatus to the members of Prof. Makoto Okano's group in AIST: Dr. Mitsuho Furuse and Dr. Schuichiro Fuchino, and the members of Fujihira Co. Ltd.: Dr. Jun-ichi Fujihira, Mr. Akira Uchida, Mr. Kazunori Watanabe, Mr. Hideyuki Fujihira, and Mr. Seiichi Fujihira. Furthermore, technical advice on the design of the apparatus from Prof. Tsuneharu Koide was quite useful for me. Let me thank here all the people mentioned above. I also deeply appreciate the people in Fujimori Group who have been engaged in the design, construction, and improvement of the vector-magnet apparatus for their hard work: Dr. Toshiharu Kadono, Dr. Keisuke Ishigami, Mr. Takayuki Harano, Dr. Yukio Takahashi, Dr. Shoya Sakamoto, Mr. Yosuke Nonaka, Mr. Keisuke Ikeda, and Mr. Zhendong Chi.

The experiments at the synchrotron facilities were supported by a number of people. I thank Prof. Tsuneharu Koide, Prof. Kenta Amemiya,

and Dr. Masako Sakamaki for their technical supports regarding the experiments at KEK-PF BL-16A. I also thank the members of Prof. Hiroshi Yamagami's group for their supports regarding the XMCD experiments at SPring-8 BL23SU: Dr. Yukiharu Takeda, Dr. Tetsuo Okane, and Dr. Yuji Saitoh.

As for the angle-dependent XMCD study, discussion with Prof. Hiroki Wadati in ISSP about the results of XLD of LSMO thin films and with Prof. Arata Tanaka in Hiroshima University about the cluster-model calculation was quite fruitful for me. I would like to express my gratitude to them.

I am grateful to all the current and former members of Fujimori Group, who have continuously supported me in all aspects from the beginning of my research life: Dr. Takashi Kataoka, Dr. Vijay Raj Singh, Dr. Shin-ichiro Ideta, Dr. Keisuke Ishigami, Dr. Virendra Kumar Verma, Mr. Shin-ichi Aizaki, Mr. Yo Yamazaki, Mr. Ichiro Nishi, Dr. Wataru Uemura, Dr. Leo Cristobal C. Ambolode II, Dr. Liu Liang, Dr. Hakuto Suzuki, Mr. Takayuki Harano, Dr. Xu Jian, Dr. Masafumi Horio, Dr. Yukio Takahashi, Dr. Shoya Sakamoto, Mr. Yosuke Nonaka, Mr. Keisuke Ikeda, Mr. Zhendong Chi, Mr. Suguru Nakata, Mr. Kenta Hagiwara, Mr. Chun Lin, Mr. Yuxuan Wan, Mr. Masahiro Suzuki, Dr. Toshiharu Kadono, and Dr. Kohei Yoshimatsu. Let me also thank Ms. Emiko Murayama, Ms. Yuko Shimazaki, Ms. Miki Ueda, Ms. Ami Michimura, and Ms. Mayuko Niwata, who are the present or the former secretaries of our group, for their help with business stuff and encouragement for me.

Finally but not least, I would like to express my special gratitude to my family for their continuous encouragement and support for a long time.

January 2019,
Goro Shibata

References

[1] J. M. D. Coey, *Magnetism and Magnetic Materials* (Cambridge University Press, New York, 2009).

[2] J. Stöhr and H. König, Phys. Rev. Lett. **75**, 3748 (1995).

[3] H. A. Dürr and G. van der Laan, Phys. Rev. B **54**, R760 (1996).

[4] M. Furuse, M. Okano, S. Fuchino, A. Uchida, J. Fujihira, S. Fujihira, T. Kadono, A. Fujimori, and T. Koide, IEEE Trans. Appl. Supercond. **23**, 4100704 (2013).

[5] J. Z. Sun, W. J. Gallagher, P. R. Duncombe, L. Krusin-Elbaum, R. A. Altman, A. Gupta, Y. Lu, G. Q. Gong, and G. Xiao, Appl. Phys. Lett. **69**, 3266 (1996).

[6] F. Pailloux, D. Imhoff, T. Sikora, A. Barthélémy, J.-L. Maurice, J.-P. Contour, C. Colliex, and A. Fert, Phys. Rev. B **66**, 014417 (2002).

[7] M. Bowen, M. Bibes, A. Barthlmy, J.-P. Contour, A. Anane, Y. Lematre, and A. Fert, Appl. Phys. Lett. **82**, 233 (2003).

[8] H. Yamada, Y. Ogawa, Y. Ishii, H. Sato, M. Kawasaki, H. Akoh, and Y. Tokura, Science **305**, 646 (2004).

[9] M. Imada, A. Fujimori, and Y. Tokura, Rev. Mod. Phys. **70**, 1039 (1998).

[10] S. Majumdar and S. van Dijken, J. Phys. D: Appl. Phys. **47**, 034010 (2014).

[11] K. J. Choi, S. H. Baek, H. W. Jang, L. J. Belenky, M. Lyubchenko, and C. Eom, Adv. Mater. **22**, 759 (2010).

[12] A. Fujimori, J. Phys. Chem. Solids **53**, 1595 (1992).

[13] R. Venkatesh, M. Pattabiraman, S. Angappane, G. Rangarajan, K. Sethupathi, J. Karatha, M. Fecioru-Morariu, R. M. Ghadimi, and G. Guntherodt, Phys. Rev. B **75**, 224415 (2007).

[14] A. P. Ramirez, J. Phys.: Condens. Matter **9**, 8171 (1997).

[15] Y. Tokura and Y. Tomioka, J. Magn. Magn. Mater. **200**, 1 (1999).

[16] Y. Tokura, Rep. Prog. Phys. **69**, 797 (2006).

[17] Y. Tokura, A. Urushibara, Y. Moritomo, T. Arima, A. Asamitsu, G. Kido, and N. Furukawa, J. Phys. Soc. Jpn. **63**, 3931 (1994).

[18] J. Park, E. Vescovo, H.-J. Kim, C. Kwon, R. Ramesh, and T. Venkatesan, Nature **392**, 794 (1998).

[19] Y. Konishi, Z. Fang, M. Izumi, T. Manako, M. Kasai, H. Kuwahara, M. Kawasaki, K. Terakura, and Y. Tokura, J. Phys. Soc. Jpn. **68**, 3790 (1999).

[20] Y. Murakami, J. P. Hill, D. Gibbs, M. Blume, I. Koyama, M. Tanaka, H. Kawata, T. Arima, Y. Tokura, K. Hirota, and Y. Endoh, Phys. Rev. Lett. **81**, 582 (1998).

[21] G. Shibata, M. Kitamura, M. Minohara, K. Yoshimatsu, T. Kadono, K. Ishigami, T. Harano, Y. Takahashi, S. Sakamoto, Y. Nonaka, K. Ikeda, Z. Chi, M. Furuse, S. Fuchino, M. Okano, J.-i. Fujihira, A. Uchida, K. Watanabe, H. Fujihira, S. Fujihira, A. Tanaka, H. Kumigashira, T. Koide, and A. Fujimori, npj Quantum Mater. **3**, 3 (2018).

[22] A. Kokalj, J. Mol. Graphics Modell. **17**, 176 (1999).

[23] M. Uehara, S. Mori, C. Chen, and S.-W. Cheong, Nature **399**, 560 (1999).

[24] M. Fäth, S. Freisem, A. A. Menovsky, Y. Tomioka, J. Aarts, and J. A. Mydosh, Science **285**, 1540 (1999).

[25] A. Ohtomo and H. Hwang, Nature **427**, 423 (2004).

[26] N. Reyren, S. Thiel, A. D. Caviglia, L. F. Kourkoutis, G. Hammerl, C. Richter, C. W. Schneider, T. Kopp, A.-S. Rüetschi, D. Jaccard, M. Gabay, D. A. Muller, J.-M. Triscone, and J. Mannhart, Science **317**, 1196 (2007).

[27] A. Brinkman, M. Huijben, M. van Zalk, J. Huijben, U. Zeitler, J. Maan, W. Wiel, G. Rijnders, D. Blank, and H. Hilgenkamp, Nat. Mater. **6**, 493 (2007).

[28] N. Nakagawa, H. Y. Hwang, and D. A Muller, Nat. Mater. **5**, 204 (2005).

[29] A. Kalabukhov, R. Gunnarsson, J. Börjesson, E. Olsson, T. Claeson, and D. Winkler, Phys. Rev. B **75**, 121404 (2007).

[30] L. Qiao, T. C. Droubay, V. Shutthanandan, Z. Zhu, P. V. Sushko, and S. A. Chambers, J. Phys.: Condens. Matter **22**, 312201 (2010).

[31] K. Yoshimatsu, T. Okabe, H. Kumigashira, S. Okamoto, S. Aizaki, A. Fujimori, and M. Oshima, Phys. Rev. Lett. **104**, 147601 (2010).

[32] R. Scherwitzl, S. Gariglio, M. Gabay, P. Zubko, M. Gibert, and J.-M. Triscone, Phys. Rev. Lett. **106**, 246403 (2011).

[33] E. Sakai, M. Tamamitsu, K. Yoshimatsu, S. Okamoto, K. Horiba, M. Oshima, and H. Kumigashira, Phys. Rev. B **87**, 075132 (2013).

[34] X. Hong, A. Posadas, and C. H. Ahn, Appl. Phys. Lett. **86**, 142501 (2005).

[35] M. Huijben, L. W. Martin, Y.-H. Chu, M. B. Holcomb, P. Yu, G. Rijnders, D. H. A. Blank, and R. Ramesh, Phys. Rev. B **78**, 094413 (2008).

[36] K. Yoshimatsu, K. Horiba, H. Kumigashira, E. Ikenaga, and M. Oshima, Appl. Phys. Lett. **94**, 071901 (2009).

[37] J. Xia, W. Siemons, G. Koster, M. R. Beasley, and A. Kapitulnik, Phys. Rev. B **79**, 140407 (2009).

[38] D. Toyota, I. Ohkubo, H. Kumigashira, M. Oshima, T. Ohnishi, M. Lippmaa, M. Takizawa, A. Fujimori, K. Ono, M. Kawasaki, and H. Koinuma, Appl. Phys. Lett. **87**, 162508 (2005).

[39] K. Yoshimatsu, K. Horiba, H. Kumigashira, T. Yoshida, A. Fujimori, and M. Oshima, Science **333**, 319 (2011).

[40] M. Jałochowski and E. Bauer, Phys. Rev. B **38**, 5272 (1988).

[41] D. B. Haviland, Y. Liu, and A. M. Goldman, Phys. Rev. Lett. **62**, 2180 (1989).

[42] D. C. Licciardello and D. J. Thouless, J. Phys. C: Solid State Phys. **8**, 4157 (1975).

[43] A. F. Ioffe and A. R. Regel, Prog. Semicond. **4**, 237 (1960).

[44] K. Fuchs, Proc. Cambridge Philos. Soc. **34**, 100 (1938).

[45] M. P. de Jong, I. Bergenti, V. A. Dediu, M. Fahlman, M. Marsi, and C. Taliani, Phys. Rev. B **71**, 014434 (2005).

[46] F. Tsui, M. C. Smoak, T. K. Nath, and C. B. Eom, Appl. Phys. Lett. **76**, 2421 (2000).

[47] C. Kwon, M. Robson, K.-C. Kim, J. Gu, S. Lofland, S. Bhagat, Z. Trajanovic, M. Rajeswari, T. Venkatesan, A. Kratz, R. Gomez, and R. Ramesh, J. Magn. Magn. Mater. **172**, 229 (1997).

[48] A. Tebano, C. Aruta, P. G. Medaglia, F. Tozzi, G. Balestrino, A. A. Sidorenko, G. Allodi, R. De Renzi, G. Ghiringhelli, C. Dallera, L. Braicovich, and N. B. Brookes, Phys. Rev. B **74**, 245116 (2006).

[49] A. Tebano, C. Aruta, S. Sanna, P. G. Medaglia, G. Balestrino, A. A. Sidorenko, R. De Renzi, G. Ghiringhelli, L. Braicovich, V. Bisogni, and N. B. Brookes, Phys. Rev. Lett. **100**, 137401 (2008).

[50] C. Aruta, G. Ghiringhelli, V. Bisogni, L. Braicovich, N. B. Brookes, A. Tebano, and G. Balestrino, Phys. Rev. B **80**, 014431 (2009).

[51] D. Pesquera, G. Herranz, A. Barla, E. Pellegrin, F. Bondino, E. Magnano, F. Sánchez, and J. Fontcuberta, Nat. Commun. **3**, 1189 (2012).

[52] L. Tröger, D. Arvanitis, K. Baberschke, H. Michaelis, U. Grimm, and E. Zschech, Phys. Rev. B **46**, 3283 (1992).

[53] S. Eisebitt, T. Böske, J.-E. Rubensson, and W. Eberhardt, Phys. Rev. B **47**, 14103 (1993).

[54] B. T. Thole, P. Carra, F. Sette, and G. van der Laan, Phys. Rev. Lett. **68**, 1943 (1992).

[55] P. Carra, B. T. Thole, M. Altarelli, and X. Wang, Phys. Rev. Lett. **70**, 694 (1993).

[56] C. T. Chen, Y. U. Idzerda, H.-J. Lin, N. V. Smith, G. Meigs, E. Chaban, G. H. Ho, E. Pellegrin, and F. Sette, Phys. Rev. Lett. **75**, 152 (1995).

[57] P. Bruno, Phys. Rev. B **39**, 865 (1989).

[58] D.-s. Wang, R. Wu, and A. J. Freeman, Phys. Rev. B **47**, 14932 (1993).

[59] G. van der Laan, J. Phys. Condens. Matter **10**, 3239 (1998).

[60] D. Weller, J. Stöhr, R. Nakajima, A. Carl, M. G. Samant, C. Chappert, R. Mégy, P. Beauvillain, P. Veillet, and G. A. Held, Phys. Rev. Lett. **75**, 3752 (1995).

[61] W. Zhu, H.-C. Ding, S.-J. Gong, Y. Liu, and C.-G. Duan, J. Phys.: Condens. Matter **25**, 396001 (2013).

[62] M. Kotsugi, M. Mizuguchi, S. Sekiya, M. Mizumaki, T. Kojima, T. Nakamura, H. Osawa, K. Kodama, T. Ohtsuki, T. Ohkochi, K. Takanashi, and Y. Watanabe, J. Magn. Magn. Mater. **326**, 235 (2013).

[63] M. M. Soares, A. D. Lamirand, A. Y. Ramos, M. De Santis, and H. C. N. Tolentino, Phys. Rev. B **90**, 214403 (2014).

[64] I. V. Solovyev, P. H. Dederichs, and I. Mertig, Phys. Rev. B **52**, 13419 (1995).

[65] P. Ravindran, A. Kjekshus, H. Fjellvåg, P. James, L. Nordström, B. Johansson, and O. Eriksson, Phys. Rev. B **63**, 144409 (2001).

[66] Y. Miura, S. Ozaki, Y. Kuwahara, M. Tsujikawa, K. Abe, and M. Shirai, J. Phys.: Condens. Matter **25**, 106005 (2013).

[67] K. Ikeda, T. Seki, G. Shibata, T. Kadono, K. Ishigami, Y. Takahashi, M. Horio, S. Sakamoto, Y. Nonaka, M. Sakamaki, K. Amemiya, N. Kawamura, M. Suzuki, K. Takanashi, and A. Fujimori, Appl. Phys. Lett. **111**, 142402 (2017).

[68] B. T. Thole, G. van der Laan, and G. A. Sawatzky, Phys. Rev. Lett. **55**, 2086 (1985).

[69] P. Carra, H. König, B. Thole, and M. Altarelli, Physica B **192**, 182 (1993).

[70] J. J. Sakurai and J. J. Napolitano, in *Modern Quantum Mechanics*, 2 ed. (Addison Wesley, New York, 2010), Chap. 3.

[71] E. Benckiser, M. W Haverkort, S. Brck, E. Goering, S. Macke, A. Frano, X. Yang, O. Andersen, G. Cristiani, H. Habermeier, A. Boris, I. Zegkinoglou, P. Wochner, h.-J. Kim, V. Hinkov, and B. Keimer, Nat. Mater. **10**, 189 (2011).

[72] A. Tanaka and T. Jo, J. Phys. Soc. Jpn. **63**, 2788 (1994).

[73] J. C. Slater, Phys. Rev. **34**, 1293 (1929).

[74] J. C. Slater and G. F. Koster, Phys. Rev. **94**, 1498 (1954).

[75] J.-i. Fujihira, A. Uchida, S. Fujihira, M. Furuse, M. Okano, S. Fuchino, T. Kadono, K. Yoshimatsu, A. Fujimori, H. Kumigashira, and T. Koide, J. Cryo. Super. Soc. Jpn. **48**, 233 (2013), (Japanese).

[76] E. Arenholz and S. O. Prestemon, Rev. Sci. Instr. **76**, 083908 (2005).

[77] C. S. Hwang, C. T. Chen, C. H. Chang, C. Y. Liu, F. Y. Lin, B. Wang, and R. Wahrer, J. Magn. Magn. Mater. **239**, 586 (2002).

[78] K. Amemiya, A. Toyoshima, T. Kikuchi, T. Kosuge, K. Nigorikawa, R. Sumii, and K. Ito, AIP Conf. Proc. **1234**, 295 (2010).

[79] K. Amemiya, BL-16A: Variable Polarization Soft X-ray spectroscopy Station, `http://pfwww.kek.jp/users_info/users_guide_e/station_spec_e/bl16/bl16a.html`, retrieved in January 16, 2019.

[80] T. Muro, T. Nakamura, T. Matsushita, H. Kimura, T. Nakatani, T. Hirono, T. Kudo, K. Kobayashi, Y. Saitoh, M. Takeuchi, T. Hara, K. Shirasawa, and H. Kitamura, J. Electron. Spectrosc. Relat. Phenom. **144-147**, 1101 (2005).

[81] K. Amemiya, M. Sakamaki, T. Koide, K. Ito, K. Tsuchiya, K. Harada, T. Aoto, T. Shioya, T. Obina, S. Yamamoto, and Y. Kobayashi, J. Phys. Conf. Ser. **425**, 152015 (2013).

[82] K. Amemiya and T. Ohta, J. Synchrotron Radiat. **11**, 171 (2004).

[83] M. C. Hettrick and S. Bowyer, Appl. Opt. **22**, 3921 (1983).

[84] Y. Saitoh, T. Nakatani, T. Matsushita, A. Agui, A. Yoshigoe, Y. Teraoka, and A. Yokoya, Nucl. Instrum. Methods Phys. Res., Sect. A **474**, 253 (2001).

[85] T. Koide, T. Shidara, and H. Fukutani, Rev. Sci. Instrum. **63**, 1462 (1992).

[86] Y. Saitoh, Y. Fukuda, Y. Takeda, H. Yamagami, S. Takahashi, Y. Asano, T. Hara, K. Shirasawa, M. Takeuchi, T. Tanaka, and H. Kitamura, J. Synchrotron Radiat. **19**, 388 (2012).

[87] A. Agui, A. Yoshigoe, T. Nakatani, T. Matsushita, Y. Saitoh, A. Yokoya, H. Tanaka, Y. Miyahara, T. Shimada, M. Takeuchi, T. Bizen, S. Sasaki, M. Takao, H. Aoyagi, T. P. Kudo, K. Satoh, S. Wu, Y. Hiramatsu, and H. Ohkuma, Rev. Sci. Instrum. **72**, 3191 (2001).

[88] E. C. Stoner and E. P. Wohlfarth, Philos. Trans. R. Soc. London, Ser. A **240**, 599 (1948).

[89] H. Boschker, J. Kautz, E. P. Houwman, W. Siemons, D. H. A. Blank, M. Huijben, G. Koster, A. Vailionis, and G. Rijnders, Phys. Rev. Lett. **109**, 157207 (2012).

[90] E. H. Sondheimer, Phys. Rev. **80**, 401 (1950).

[91] K. Horiba, H. Ohguchi, H. Kumigashira, M. Oshima, K. Ono, N. Nakagawa, M. Lippmaa, M. Kawasaki, and H. Koinuma, Rev. Sci. Instrum. **74**, 3406 (2003).

[92] T. Koide, H. Miyauchi, J. Okamoto, T. Shidara, T. Sekine, T. Saitoh, A. Fujimori, H. Fukutani, M. Takano, and Y. Takeda, Phys. Rev. Lett. **87**, 246404 (2001).

[93] Y. Teramura, A. Tanaka, and T. Jo, J. Phys. Soc. Jpn. **65**, 1053 (1996).

[94] C. Piamonteze, P. Miedema, and F. M. F. de Groot, J. Phys. Conf. Ser. **190**, 012015 (2009).

[95] T. Burnus, Z. Hu, H. H. Hsieh, V. L. J. Joly, P. A. Joy, M. W. Haverkort, H. Wu, A. Tanaka, H.-J. Lin, C. T. Chen, and L. H. Tjeng, Phys. Rev. B **77**, 125124 (2008).

[96] R. K. Sahu, Z. Hu, M. L. Rao, S. S. Manoharan, T. Schmidt, B. Richter, M. Knupfer, M. Golden, J. Fink, and C. M. Schneider, Phys. Rev. B **66**, 144415 (2002).

[97] Y. Ishii, H. Yamada, H. Sato, H. Akoh, M. Kawasaki, and Y. Tokura, Appl. Phys. Lett. **87**, 022509 (2005).

[98] Y. Takeda, M. Kobayashi, T. Okane, T. Ohkochi, J. Okamoto, Y. Saitoh, K. Kobayashi, H. Yamagami, A. Fujimori, A. Tanaka, J. Okabayashi, M. Oshima, S. Ohya, P. N. Hai, and M. Tanaka, Phys. Rev. Lett. **100**, 247202 (2008).

[99] C. N. R. Rao, G. Kulkarni, A. Govindaraj, B. C. Satishkumar, and P. Thomas, Pure Appl. Chem.Pure Appl. Chem **72**, 21 (2000).

[100] B. N. Reinecke, K. P. Kuhl, H. Ogasawara, L. Li, J. Voss, F. Abild-Pedersen, A. Nilsson, and T. F. Jaramillo, Surf. Sci. **650**, 24 (2016).

[101] K. Yoshimatsu, H. Wadati, E. Sakai, T. Harada, Y. Takahashi, T. Harano, G. Shibata, K. Ishigami, T. Kadono, T. Koide, T. Sugiyama, E. Ikenaga, H. Kumigashira, M. Lippmaa, M. Oshima, and A. Fujimori, Phys. Rev. B **88**, 174423 (2013).

[102] J.-S. Lee, D. A. Arena, P. Yu, C. S. Nelson, R. Fan, C. J. Kinane, S. Langridge, M. D. Rossell, R. Ramesh, and C.-C. Kao, Phys. Rev. Lett. **105**, 257204 (2010).

[103] F. Sandiumenge, J. Santiso, L. Balcells, Z. Konstantinovic, J. Roqueta, A. Pomar, J. P. Espinós, and B. Martínez, Phys. Rev. Lett. **110**, 107206 (2013).

[104] H. Kumigashira, A. Chikamatsu, R. Hashimoto, M. Oshima, T. Ohnishi, M. Lippmaa, H. Wadati, A. Fujimori, K. Ono, M. Kawasaki, and H. Koinuma, Appl. Phys. Lett. **88**, 192504 (2006).

[105] R. Nakajima, J. Stöhr, and Y. U. Idzerda, Phys. Rev. B **59**, 6421 (1999).

[106] A. Urushibara, Y. Moritomo, T. Arima, A. Asamitsu, G. Kido, and Y. Tokura, Phys. Rev. B **51**, 14103 (1995).

[107] G. van der Laan, Phys. Rev. B **57**, 5250 (1998).

[108] T. Maruyama, I. Hojo, S. ichi Nagamatsu, and T. Fujikawa, J. Electron. Spectrosc. Relat. Phenom. **180**, 46 (2010).

[109] H. A. Dürr, G. Y. Guo, G. van der Laan, J. Lee, G. Lauhoff, and J. A. C. Bland, Science **277**, 213 (1997).

[110] K. Mamiya, T. Koide, Y. Ishida, Y. Osafune, A. Fujimori, Y. Suzuki, T. Katayama, and S. Yuasa, Radiat. Phys. Chem. **75**, 1872 (2006).

[111] G. van der Laan, R. V. Chopdekar, Y. Suzuki, and E. Arenholz, Phys. Rev. Lett. **105**, 067405 (2010).

[112] T. Koide, K. Mamiya, D. Asakura, Y. Osafune, A. Fujimori, Y. Suzuki, T. Katayama, and S. Yuasa, J. Phys. Conf. Ser. **502**, 012002 (2014).

[113] K. Horiba, A. Chikamatsu, H. Kumigashira, M. Oshima, N. Nakagawa, M. Lippmaa, K. Ono, M. Kawasaki, and H. Koinuma, Phys. Rev. B **71**, 155420 (2005).

[114] G. Shibata, K. Yoshimatsu, E. Sakai, V. R. Singh, V. K. Verma, K. Ishigami, T. Harano, T. Kadono, Y. Takeda, T. Okane, Y. Saitoh, H. Yamagami, A. Sawa, H. Kumigashira, M. Oshima, T. Koide, and A. Fujimori, Phys. Rev. B **89**, 235123 (2014).

[115] K. Yoshimatsu, K. Horiba, H. Kumigashira, E. Ikenaga, and M. Oshima, Appl. Phys. Lett. **94**, 071901 (2009).

[116] S. Miwa, M. Suzuki, M. Tsujikawa, K. Matsuda, T. Nozaki, K. Tanaka, T. Tsukahara, K. Nawaoka, M. Goto, Y. Kotani, T. Ohkubo, F. Bonell, E. Tamura, K. Hono, T. Nakamura, M. Shirai, S. Yuasa, and Y. Suzuki, Nat. Commun. **8**, 15848 (2017).

[117] P. Kuiper, B. Searle, L.-C. Duda, R. Wolf, and P. van der Zaag, J. Electron. Spectrosc. Relat. Phenom. **86**, 107 (1997).

[118] M. M. Schwickert, G. Y. Guo, M. A. Tomaz, W. L. O'Brien, and G. R. Harp, Phys. Rev. B **58**, R4289 (1998).

[119] S. S. Dhesi, G. van der Laan, E. Dudzik, and A. B. Shick, Phys. Rev. Lett. **87**, 067201 (2001).

[120] J. Kuneš and P. M. Oppeneer, Phys. Rev. B **67**, 024431 (2003).

[121] E. Arenholz, G. van der Laan, R. V. Chopdekar, and Y. Suzuki, Phys. Rev. B **74**, 094407 (2006).

[122] E. Arenholz, G. van der Laan, R. V. Chopdekar, and Y. Suzuki, Phys. Rev. Lett. **98**, 197201 (2007).

[123] G. van der Laan, E. Arenholz, R. V. Chopdekar, and Y. Suzuki, Phys. Rev. B **77**, 064407 (2008).

[124] G. van der Laan, E. Arenholz, A. Schmehl, and D. G. Schlom, Phys. Rev. Lett. **100**, 067403 (2008).